Properties of Lithium Metal for Solid State Batteries

by

Alvaro G. Masias

A dissertation submitted in partial fulfillment
of the requirements for the degree of
Doctor of Philosophy
(Materials Science and Engineering)
in the University of Michigan
2021

Doctoral Committee:

Associate Professor Jeff S. Sakamoto, Chair
Mr. Ted Miller, Ford Motor Company
Professor Max Shtein
Professor Anna G. Stefanopoulou

Alvaro G. Masias

masias@umich.edu

ORCID iD: 0000-0001-9354-1970

Dedication

This dissertation is dedicated to my family, my biggest supporters.

Acknowledgements

First and foremost I would like to sincerely thank my advisor, Professor Jeff Sakamoto for the constant support over the past few years. I am grateful for your willingness to take on a non-traditional graduate researcher into your lab. I would also like to thank my committee members, Mr. Ted Miller, Professor Max Shtein and Professor Anna Stefanopoulou for their support and technical insight as part of my committee and for years prior. Thanks is also given to Mr. Kent Snyder for his constant support and flexibility during my graduate research.

I am happy to acknowledge the members of the Sakamoto lab who welcomed me into the group and were kind enough to share their knowledge, in particular Dr. Travis Thompson, Dr. Nathan Taylor, Dr. Asma Sharafi, Dr. Michael Wang, Dr. Regina Garcia-Mendez, Dr. Arushi Gupta and Dr. Kendell Pawelec. I am also grateful for the effort and contributions of my undergraduate researchers, Mr. Marcus Lee, Mr. Nando Felten, Mr. Beckett McMath, Ms. Samir Tawfik and Mr. Mihir Upandhye.

Funding support from the Ford-University of Michigan Alliance (Grant # UM0163) and the Ford Salaried Tuition Assistance Program (STAP) is acknowledged.

This dissertation contains results and conclusions based on the following papers.

Chapter 1: Masias, A., Marcicki, J., Paxton, W., "Opportunities and Challenges of Lithium Ion Batteries in Automotive Applications." *ACS Energy Letters*, 6 (**2021**), 621-630. https://dx.doi.org/10.1021/acsenergylett.0c02584

Chapter 3: Masias, A., Felten, N., Garcia-Mendez, R., Wolfenstine, J., Sakamoto, J., "Elastic, plastic and creep mechanical properties of lithium metal." *Journal of Materials Science*, 54 (**2019**), 2585-2600. https://doi.org/10.1007/s10853-018-2971-3

Chapter 4: Masias, A., Felten, N., Sakamoto, J., "Characterizing the mechanical behavior of lithium in compression." *Journal of Materials Research*, (**2021**) 1-11. https://doi.org/10.1557/s43578-020-00028-x

Chapter 5: Masias, A., Upadhye, M., Sakamoto, J., "Safety Considerations of Lithium Metal Solid State Batteries." Journal of Electrochemical Society, (**In Draft**).

Table of Contents

List of Tables

List of Figures

Abstract

The advancements in lithium ion batteries (LIBs) over the last three decades has significantly altered the modern world. The availability of efficient, portable electrical energy storage has enabled the proliferation of personal electronics, improved the viability of renewable energy sources such as wind and solar, and begun to transform the transportation sector.

Current LIB technology has enabled a diverse electric vehicle (EV) market in passenger cars, however adoption remains low compared to internal combustion engine (ICE) vehicles. Modern EVs still require customers to compromise when compared to ICE powered vehicles, primarily in the areas of cost and/or range. These limitations come from the performance of available technology, which continues to drive the evolutionary improvement of LIBs. The ecosystem of energy storage would benefit greatly from a revolutionary increase in battery performance. As the third lightest element and the lowest reduction potential, lithium metal is the ideal battery anode and has been a focal point since the 1960s. Despite decades of research, many technical challenges have prevented the usage of lithium anodes. Recent discoveries of several solid state electrolytes has renewed the prospects of lithium anode adoption.

In this work, we will study several of the properties of lithium metal in the context of future lithium metal solid state batteries (LMSSB). Despite the long history of lithium metal in batteries, relatively little is known regarding its elemental mechanical properties and their sensitivities to parameters like aspect ratio, temperature or strain rate. This is particularly true in the thin film form factor required by LMSSBs. Lithium metal is not stable in the ambient environment, which has complicated mechanical studies in addition to raising questions regarding its safety. Due to

these knowledge gaps, this work will also explore the potential safety implications of LMSSB arising from the usage of lithium metal. Our study will inform future designers of LMSSB of the mechanical limits of lithium metal and assess the potential safety consequence of its possible future use.

Chapter 1

Introduction

1.1 Motivation

The development of efficient and portable electrical energy storage in the form of lithium ion batteries (LIBs) in recent decades [1, 2, 3, 4, 5] has transformed society. This technology has powered the personal electronics revolution, which has brought the information age to every corner of the planet; a planet that is beginning to experience the climate change inducing consequences of the industrial age, which heavily relied on the consumption of fossil fuels. Transitioning the global economy towards renewable energy sources such as wind and solar has been enabled by the load leveling capabilities of LIBs [6, 7, 8, 9]. Transportation, another significant source of fossil fuel consumption, has seen the introduction of many electric vehicles (EVs) in the past decade.

The transition of the vehicle fleet from fossil fuel to electric power can bring a range of near and long term benefits to society. Growing concern with global climate change has motivated recent efforts to electrify the transportation fleet. The changing composition of the earth's atmosphere due to the release of greenhouse gases has increased the global heat imbalance by 3 W/m^2 since pre-industrial levels in 1750 [10]. Further causing concern is that 45% of this growth has occurred in the past 30 years alone (see **Figure 1.1**) [10]. Global warming holds the potential to alter the future environment in a myriad of ways. By focusing on four particular areas of impact, hurricane damage, real estate loss, increased energy needs and water scarcity, one study estimated

the direct cost of unchecked climate change to the US economy of $271 billion in 2025 and $506 billion in 2050 [11].

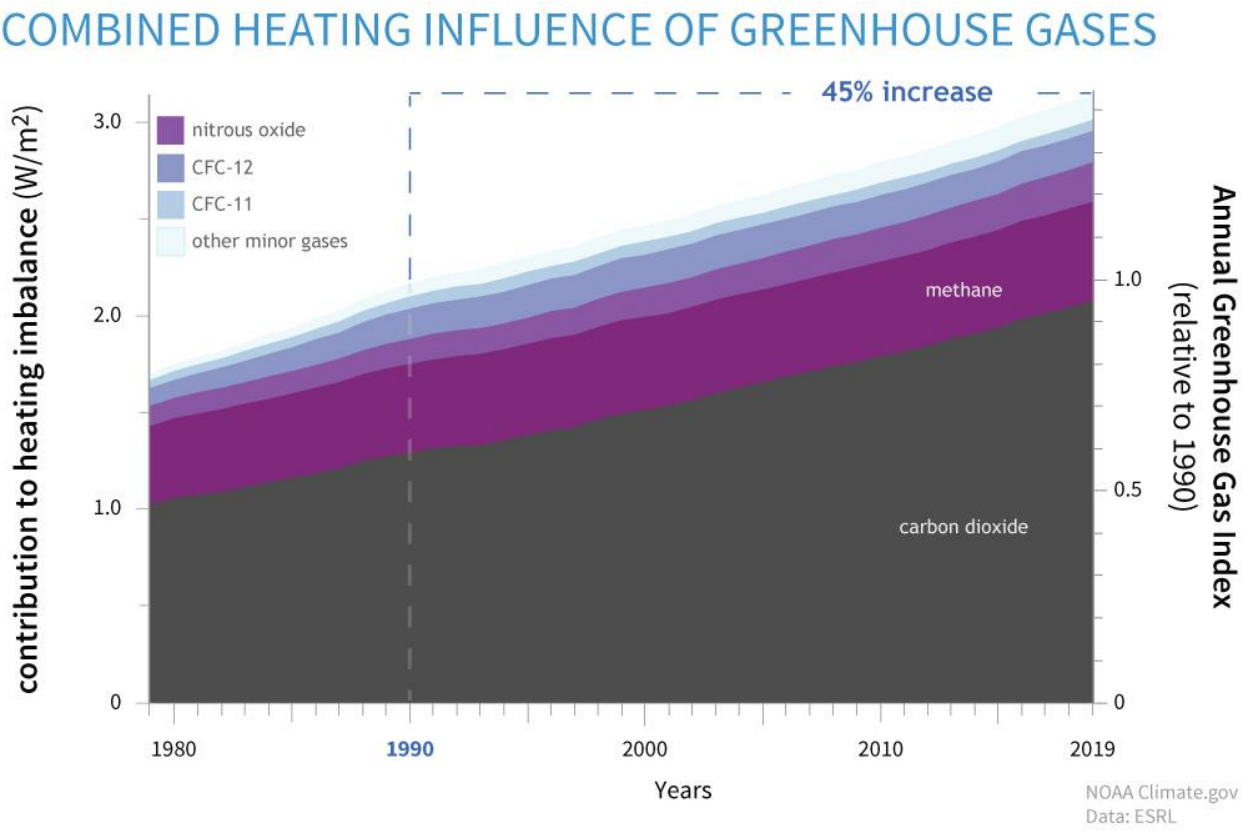

Figure 1.1: Combined Heating Influence of Greenhouse Gases [10]

An examination of **Figure 1.1** shows that the majority of the increase in heating imbalance of the atmosphere can be accounted for by rising carbon dioxide levels. The anthropogenic nature of this growing level of atmospheric carbon dioxide can be confirmed by comparing the CO_2 emissions of human activity since the industrial age (see **Figure 1.2**) [10].

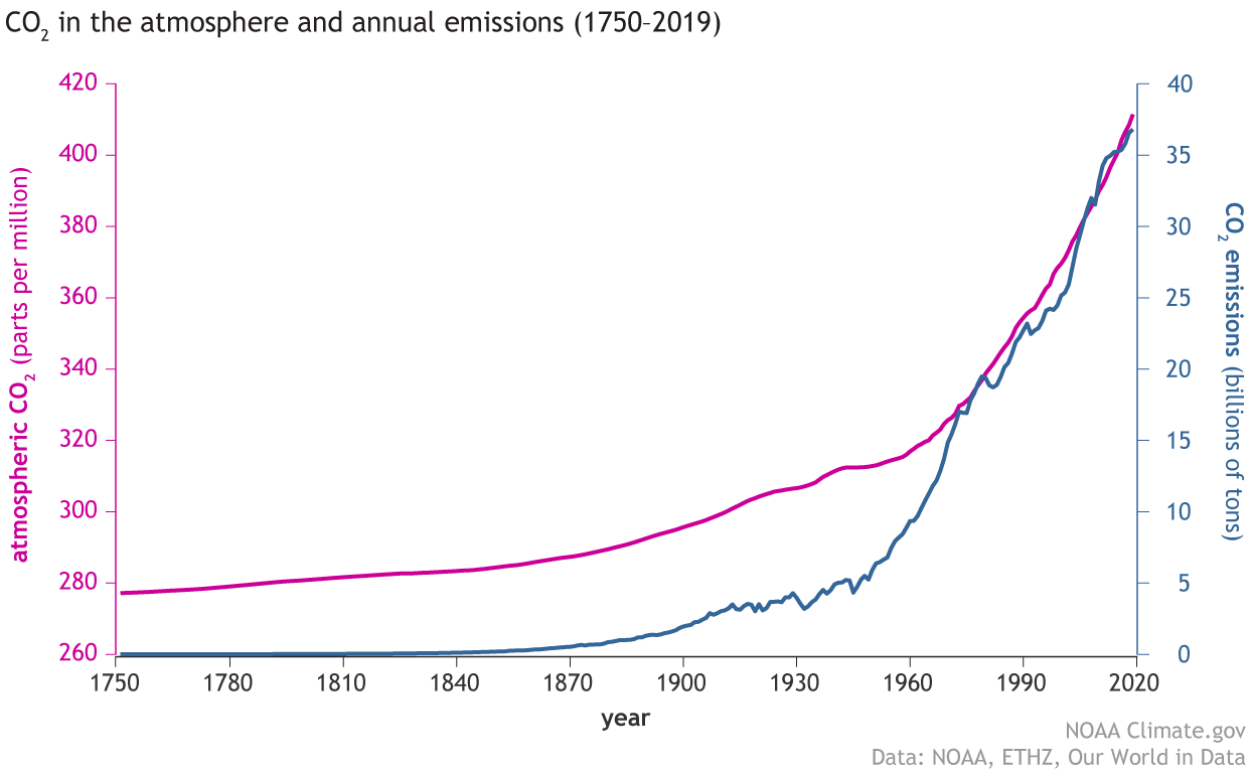

Figure 1.2: CO2 in the atmosphere and annual emissions (1750-2019) [10]

These rising levels of man-made carbon dioxide emissions have provided the modern interest in the electric vehicle. In 2019, 91% of all US transportation energy was provided by petroleum, which also accounted for 69% of all the petroleum used by the country as a whole [12]. Given that also in 2019 the US consumed 21% of the world's entire petroleum, electrified transportation has the potential to significantly reduce the consumption of fossil fuels [12]. Unfortunately, displacement of internal combustion engine (ICE) vehicles by EVs has been low, at least partially due to limitations in LIB technology. In 2019, of the 28.2 Quads of energy used by the transportation sector in the US, only 0.03 Quads or 0.1% came from electricity (see **Figure 1.3**) [13].

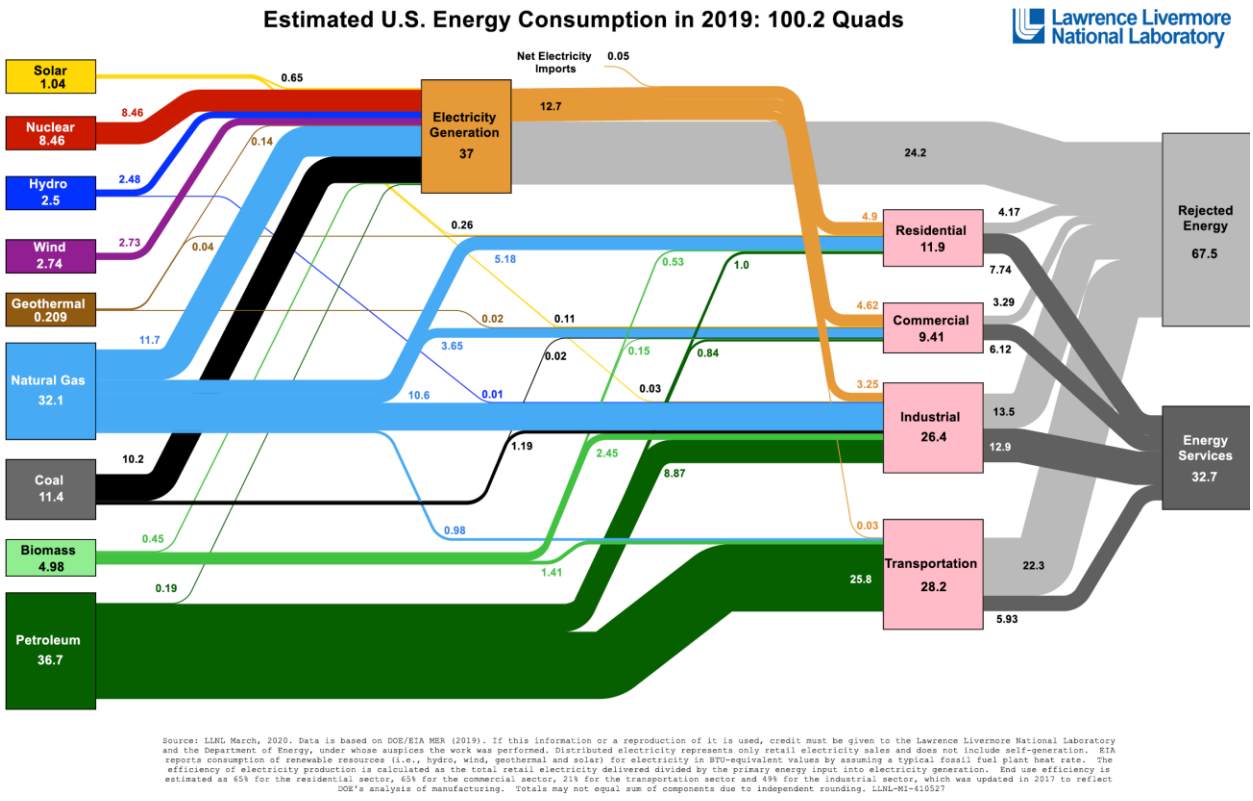

Figure 1.3: Estimated US Energy Consumption in 2019 [13]

1.1.1 Promise of Electrified Vehicles & Challenges of Cost, Weight & Volume

Transitioning the global vehicle fleet to EVs from ICE holds the potential for significant reduction in greenhouse gas emissions. Although EVs can require approximately 39% more carbon emissions to produce [14], they can result in significant net carbon savings when considering their use or run phase [15, 16]. The run emissions from an EV are primarily dependent on the carbon intensity of the local grid, the ambient temperature and ratio of rural versus urban driving. Although these three main factors can combine to result in significant regional variation of net EV carbon emissions, overall they can be markedly lower (i.e. approximately 70% lower in Los Angeles County) than ICEs [15].

The reduced emissions impact of EVs during the run phase also correlates with their lower fuel costs. A 2018 study of energy costs in the US market found EVs to be 230% cheaper to fuel than ICE vehicles ($485 versus $1,117 per year) [17]. The promise of this improvement in running costs is tempered by the initial high price of EVs, primarily driven by their LIBs. The average EPA rated combined (city and highway) range of a Ford brand vehicle in the 2020 Model Year (MY) was 474 miles. The average EPA rated electric consumption of all 2020 model year electric vehicles on sale in the US was 3.14 mi/kWh [18, 19]. To provide a customer with the average range of a gasoline powered car using a LIB in the 2020 model year would require a battery pack of 151 kWh useable energy. Depending on the cell design and vehicle application, often a portion of the battery energy content (state of charge, SOC) is held in reserve to prolong life, resulting in a true energy content requirement in excess of 166-182 kWh (assuming a 10%-20% margin for EVs) [21, 22]. Furthermore, the testing parameters of the EPA range tests are performed at 20 to 30 °C [20]. Kirchain et al. found that the extreme cool and warm conditions could increase the energy consumption rate of an EV by 40-50% beyond these baseline temperatures, potentially requiring even large battery packs [15].

Although prices have been dropping steadily in recent years for both cells and packs, this amount of energy would still require a $21,74-23,8426 battery in 2020 assuming a pack level cost of $131/kWh (see **Figure 1.4**) [19]. The average useable energy content of 2020 model year EVs was 83.1 kWh, equating to a practical battery cost of approximately $11,974-13,063 using the same methodology [19]. The historical cost of an ICE engine ($5,000) and supporting fuel/emissions systems ($2,000-$3,000), is still significantly cheaper to produce. This analysis highlights the large cost challenges still remaining for LIBs when compared with gasoline powered vehicles. As a result, current EV range lags significantly behind gasoline powered vehicle ranges.

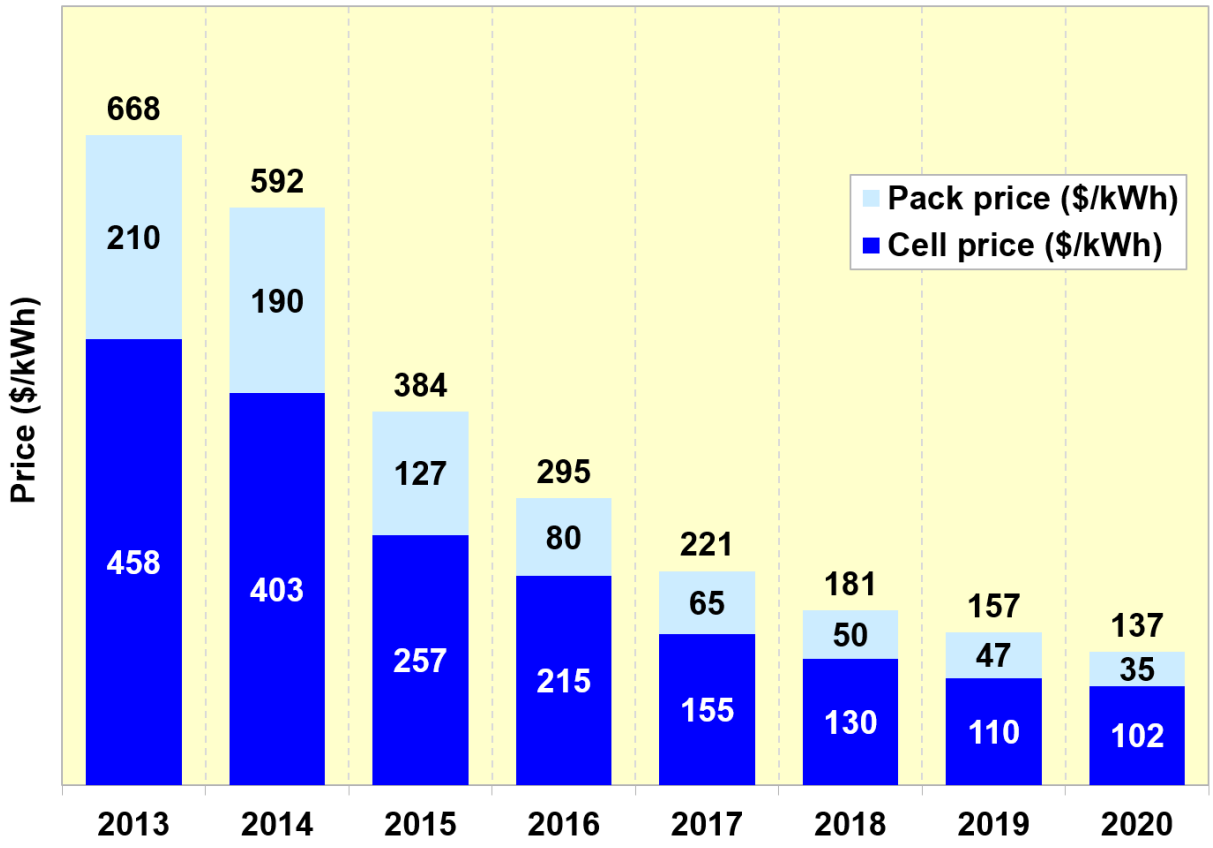

Figure 1.4: Industry Survey Based Cost Estimates for Automotive Lithium Ion Cell & Packs 2013-2020 [19, 23]

Additionally, the smaller battery energy installed in 2020 MY EVs also highlights a second large challenge remaining for LIBs range, that of packaging weight and volume. Beyond cost, the other main reasons why only 55% of the gasoline proscribed energy content is installed in modern EVs is weight (specific energy, Wh/kg) and volume (energy density, Wh/L).

Regarding weight, further improvements in battery technology are necessary to reduce the weight penalty and corresponding increases in fuel consumption seen in EVs. The Energy Systems Division of Argonne National Lab (ANL) maintains a public vehicle energy use analytical tool

called the Greenhouse gases, Regulated Emissions, and Energy use in Technologies (GREET) Model [24]. Recently in 2020 the GREET model's battery specific energy pack variables were updated (**Table 1.1**) [25]. By comparing a range of cathode driven battery pack specific energies capable of meeting the standard GREET EV design of 70.6 kWh, the impact on overall weight can be calculated (**Table 1.1**).

The fuel reduction value of non-powertrain compensated weight savings is particular to each vehicle design but has been estimated to be between 0.15 and 0.25 L/(100km*100kg) in the literature [26]. In the ANL GREET EV design (70.6 kWh), being able to achieve a next generation battery pack specific energy of 382 Wh/kg would enable a further 100 kg of weight savings at the pack level, leading to an estimated fuel consumption improvement of 0.15 to 0.25 L/100km. Conversely to achieve battery energy content of a comparable gasoline vehicle as shown previously (requiring an energy content of 166-182 kWh) would require a battery pack weight of 669-734 kg, even using the most advanced current technology considered by GREET, the NMC811 cathode.

Cathode			Pack		
			Specific Energy (Wh/kg)	Weight (kg)	Volume (L)
Lithium Iron Phosphate	LFP	$LiFePO_4$	174	405	193
Nickel Manganese Cobalt 111	NMC111	$LiNiMnCoO_2$	215	329	156
Nickel Manganese Cobalt 532	NMC532	$LiNi_{0.5}Mn_{0.3}Co_{0.2}O_2$	225	314	149

Nickel Manganese Cobalt 811	NMC811	$LiNi_{0.8}Mn_{0.1}Co_{0.1}O_2$	248	285	135

Table 1.1: Pack Weight as a function of various Cathode Derived Battery Pack Specific Energies used by the ANL GREET Model EV (70.6 kWh Pack) [24, 25]. Pack Volume calculated from the GREET Pack Weight using USABC & EUCAR target densities [27, 28]

Regarding volume, the amount of physical space available in a modern vehicles for ever increasing battery packs is more and more challenging to accommodate. The United States Advanced Battery Consortium (USABC) [27] and the European Council for Automotive R&D (EUCAR) [28] have published various goals for vehicle battery systems. Given that a vehicle's available volume is highly specific, USABC and EUCAR don't publish explicit volume targets, however based on their energy performance goals, it is possible to determine expected battery pack densities of 2.12 and 2.08 kg/L. By comparing this average battery pack density to the cathode specific pack weights calculated in the ANL GREET model, a range of chemistry specific pack volumes can be determined for the GREET EV design (70.6 kWh) (**Table 1.1**). When considering the equivalent energy content of a comparable gasoline powered vehicle (166-182 kWh), the resulting battery pack using the GREET model's most advanced cathode choice occupies 319-350 L. For all 2020 model year Ford passenger vehicles, the average liquid fuel storage volume was 74L, more than four times smaller than what would be required with an advanced battery pack to give comparable range.

1.1.2 Development History of LIBs and Challenges of Energy

LIBs have offered increased energy storage performance since their introduction by Sony Corp in 1991 [1], having steadily improved over the following three decades [19, 29]. Decades of academic research drove continuous industrial development resulting in approximately an overall

improvement of 282% in specific energy (Wh/kg) and 353% in energy density (see **Figure 1.5**) [19]. However as can also be seen from **Figure 1.5**, this growth has been uneven over time, as shown by considering the Compound Annual Growth Rate (CAGR) for weight and volume. After an initial low growth rate for the first 5 years (averaging 1.7% by weight and 3.7% by volume), the CAGR reached a relatively stable fast rate for the next 10 years (averaging 5.9% by weight and 6.6% by volume). The rate of improvement by both weight and volume then slowed significantly in 2006 and performance plateaued for the next 5 years (see **Figure 1.5**). The main catalyst for this pause was a series of laptop events in 2006 which prompted a prioritization on safety instead of energy performance [30]. By 2010 the manufacturers of consumer cylindrical cells has improved safety and quality enough to reprioritize energy performance, leading to renewed, though slower rate of improvement (see **Figure 1.5**) [19].

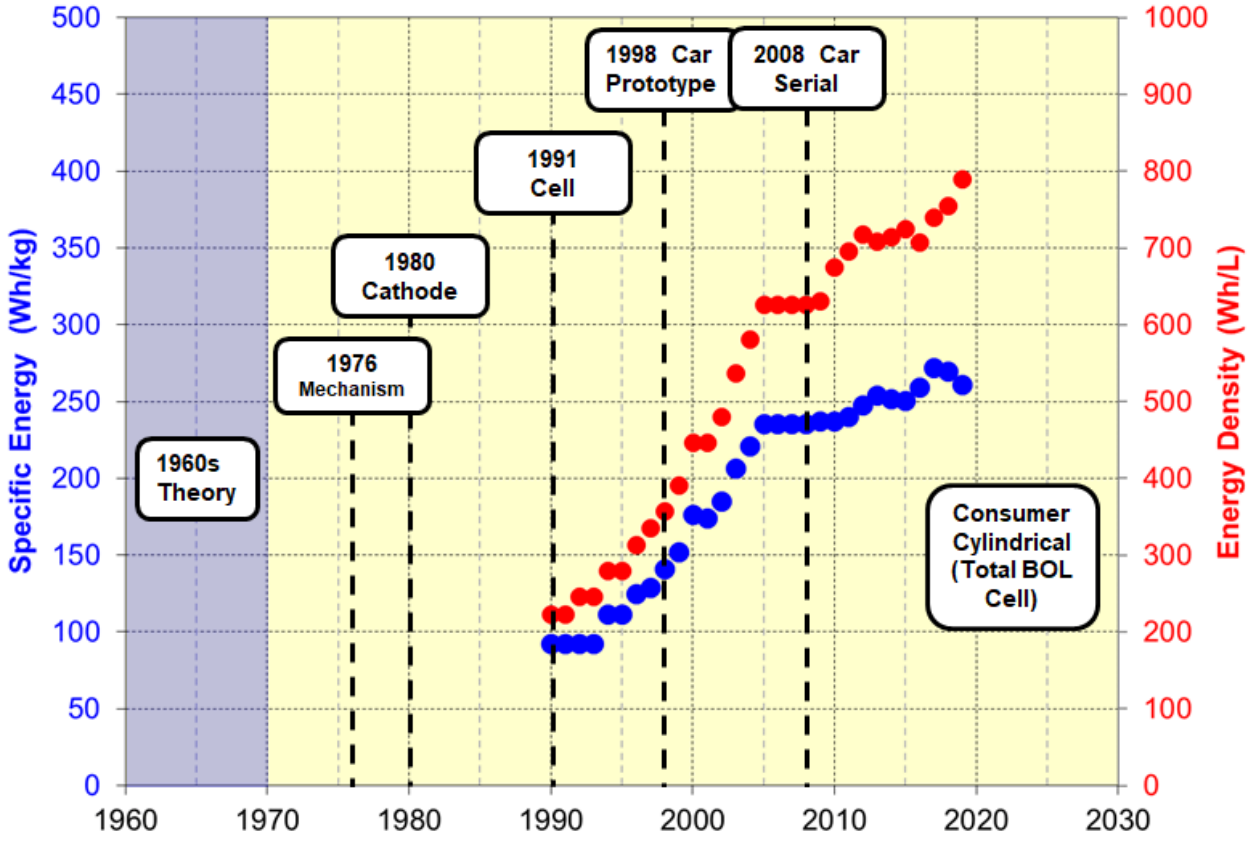

Figure 1.5: Historical Developments in Lithium Ion Batteries and Consumer Cylindrical Cell Specific Energy [19]

The slowing rate of improvement of LIB technology raises questions about the long term growth and capability of the technology. As a result, a robust research effort into Beyond Lithium Ion (BLI) technologies has developed in recent years. One of the main outputs of this BLI research effort has been development of several solid state (SS) electrolytes [31, 32]. SS electrolytes can double as separators for lithium metal, offering a potential solution to the well explored technical challenges of life and safety due to dendrite growth when employing lithium anodes [33, 34]. The substitution of a SS electrolyte/separator and lithium metal in place of the incumbent liquid carbonate electrolytes, porous polyolefin separator and graphitic carbon anode in a LIB design could provide an increase in energy storage capacity of approximately 50% [35, 36]. Due to the strong impact that weight can have on the resulting vehicle energy efficiency, gasoline or electric

(see **Figure 1.6**), such significant improvements on battery weight and volume could translate to significant overall energy savings.

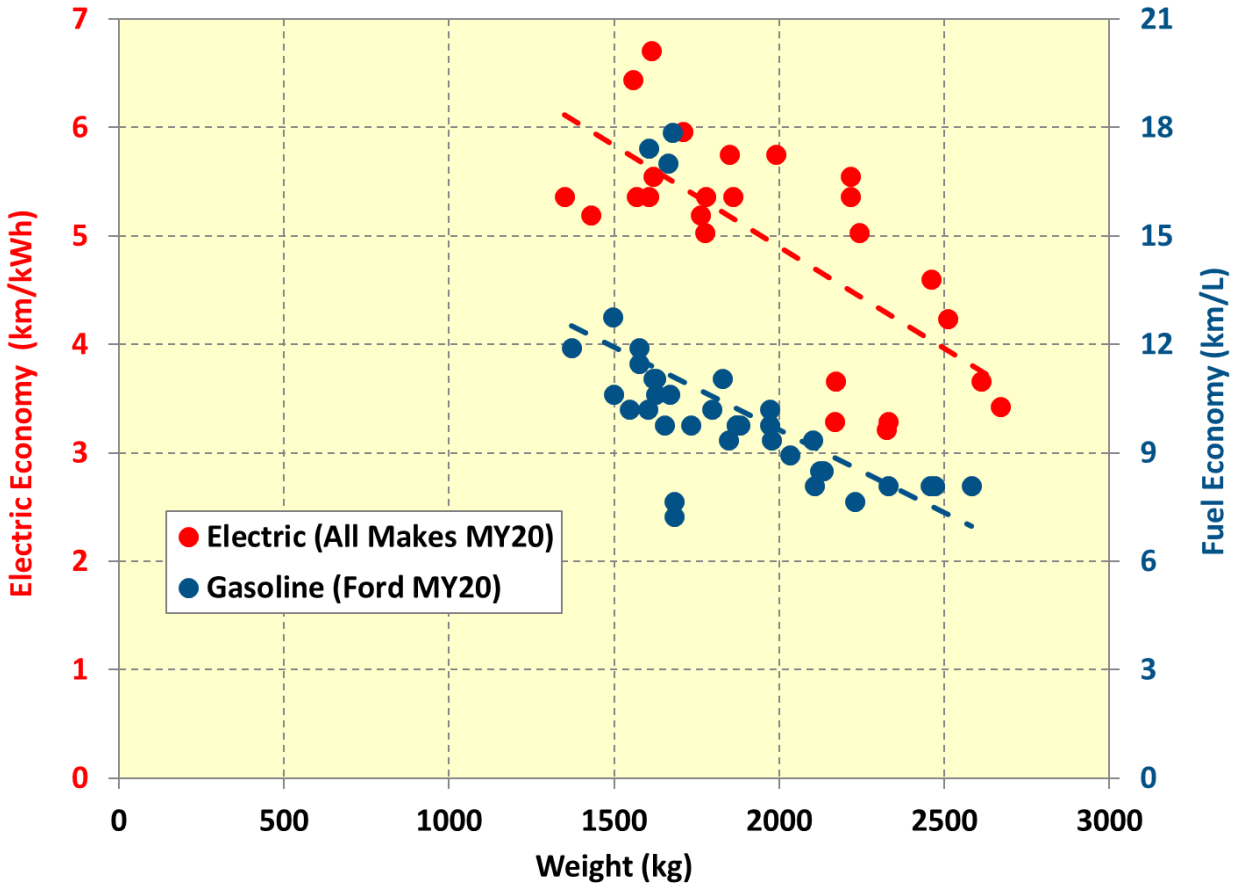

Figure 1.6: Vehicle energy economy (electric and gasoline) versus weight [19]

1.2 Lithium Metal Solid State Batteries (LMSSB)

As a new cell type, the lithium metal solid state battery (LMSSB), shares many of the same design features as a more traditional LIB (see **Figure 1.8**) [35, 36]. The first main difference is the replacement of the polyolefin thin film separator and liquid carbonate based electrolyte & lithium hexafluorophosphate charge carrying salt with a lithium conducting polymer, ceramic or glass [36]. The second major difference between LMSSB and LIB designs involves replacing the carbon based anode with lithium metal. Typically the cathode active material used is similar to a

standard LIB type, although both electrodes need to be specifically re-engineered to work efficiently with the solid electrolytes [36].

The development of LMSSB raises the potential for the industrial application of pure lithium metal for the first time. Although lithium metal has many existing applications, it is as an additive such as in aerospace alloys [37], container glasses [38], concrete [39] and lubricating greases [40]. The lack of an industrial use for pure lithium metal, combined with its instability in the ambient environment [41], has limited studies of many of its properties. The successful commercialization of LMSSB in the automotive sector would require the use of a significant quantity of elemental lithium, on the order of 7 kg to achieve 300 miles EV range (see **Figure 1.7**).

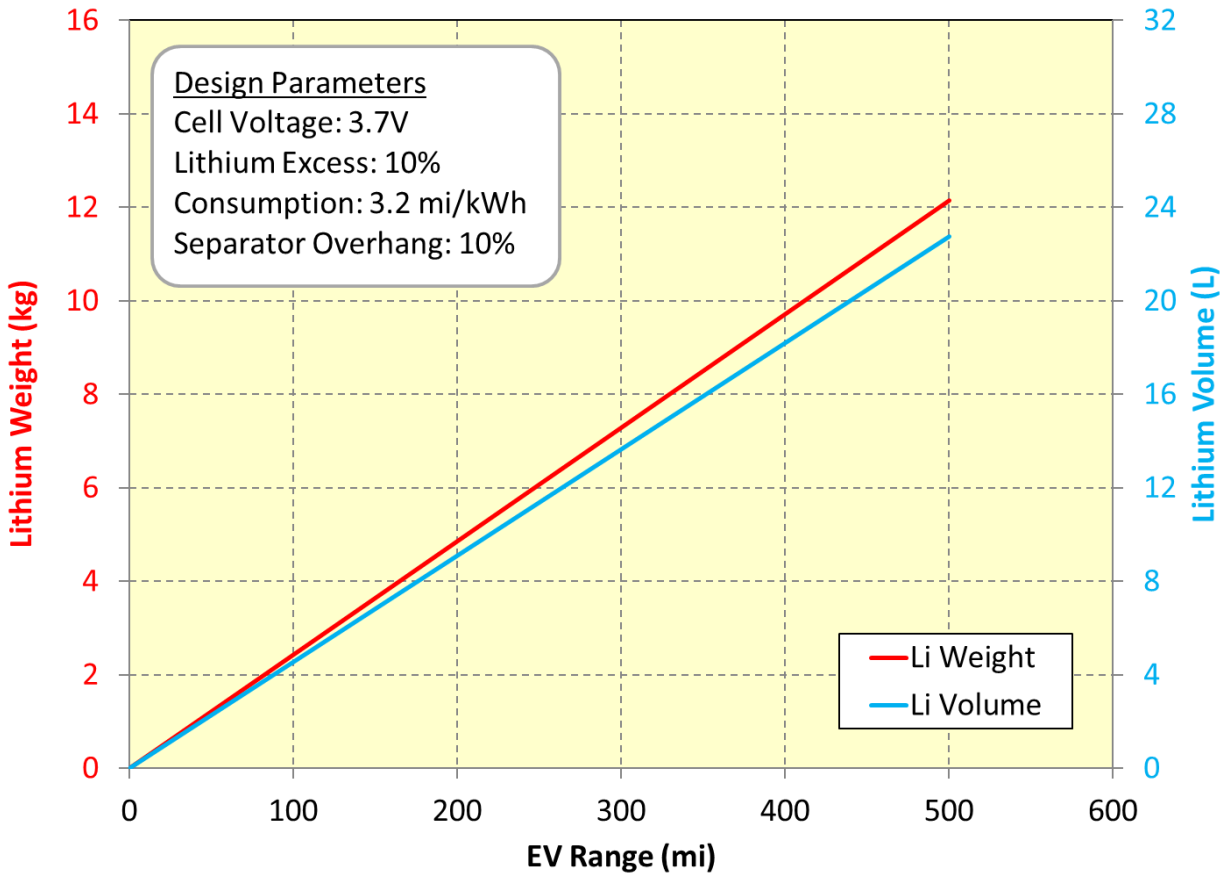

Figure 1.7: Lithium Metal Weight and Volume as a function of Electric Vehicle Range for a representative LMSSB cell, pack and vehicle design

For LMSSB, the mechanical behavior of lithium under a variety of conditions is critical to both initial and long term performance. For example, lithium has a low melting point (180.5°C), resulting in a room temperature homologous temperature of $T_H = 0.66$ [42]. By being indexed to each material's melting point, the homologous temperature allows for the comparison of some mechanical properties across temperature domains. In particular the plastic and viscoelastic behavior of materials is sensitive to the T_H. As a result, when comparing the plastic & viscoelastic behavior of lithium, a material with such a low melting point, against other materials it is important to do so across equivalent T_H values.

The boundary between cold and hot working temperatures for a material is defined as T_H = 0.50, which for lithium corresponds to -46°C [43, 44]. As a result of lithium being at such a high T_H, at room temperature, it is likely to exhibit significant creep behavior. An essential property for designers of LMSSB will be to avoid short-circuits by not allowing lithium to move around the separator and touch the cathode [42]. **Figure 3.11c** depicts a schematic of the potential short-circuit scenario to avoid in the case of LMSSB. Careful design of the lithium geometry under pressure and separator overhang margin can address this potential issue.

Unfortunately, the literature record has a limited number of lithium mechanical property studies. This study provides a critical but missing set of data for the rational design of future LMSSB by accurately quantifying the mechanical properties such as the elastic constants, yield strength, and visco-elastic (creep) rates of lithium metal.

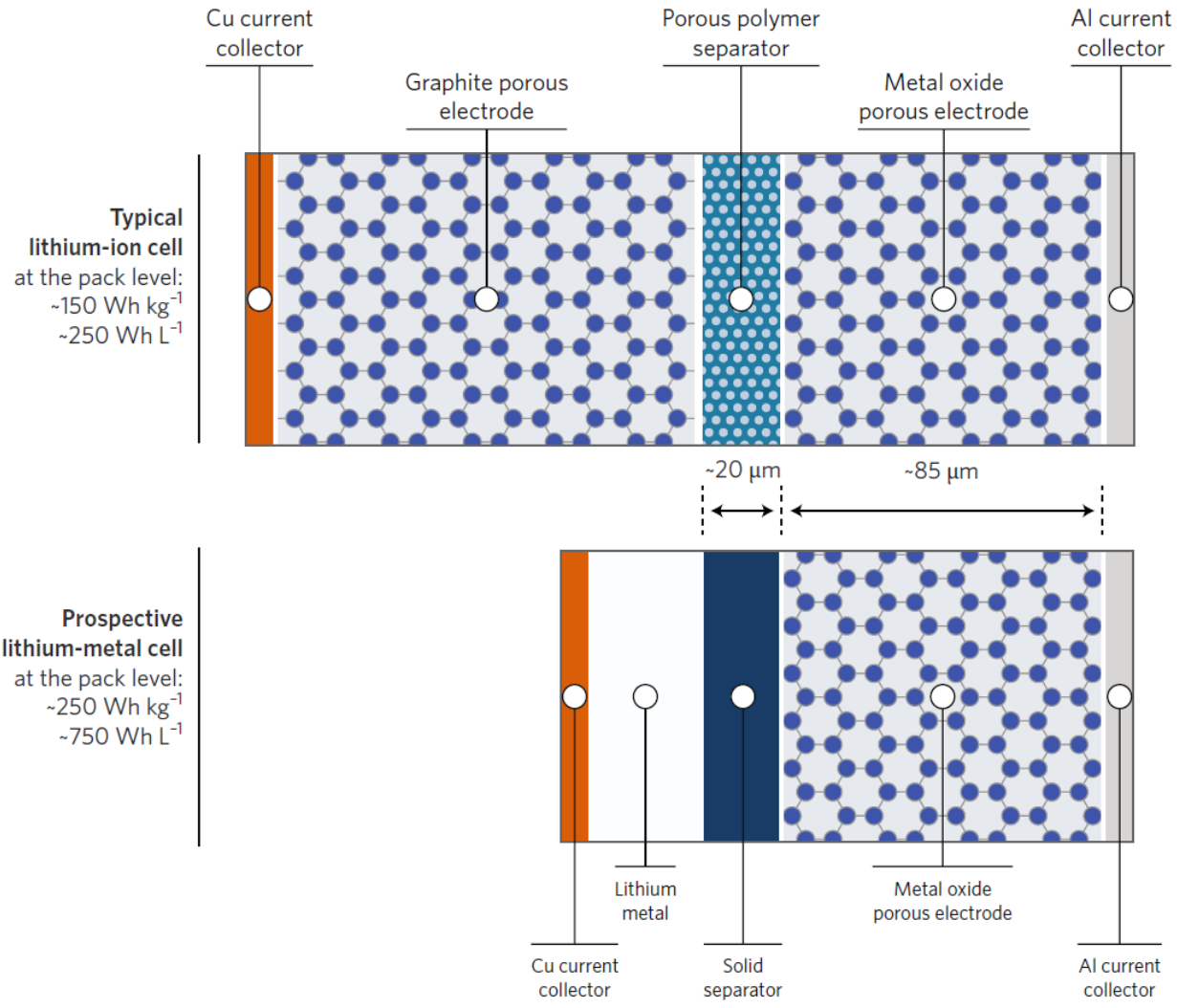

Figure 1.8: Schematic Representation of the Electrode Layers in a LIB versus a LMSSB [36]

The large scale adoption of batteries using lithium metal anodes also raises safety concerns, with the properties of lithium making it unstable in the room environment. Safety problems have also historically limited the viability of lithium metal anodes, from their initial commercialization efforts in the 1980s [1] to solid polymer electrolyte systems in the 2000s [45, 46]. As can be seen in **Figure 1.5**, safety issues had a significant tangible impact on the development history of LIB technology between 2006 and 2010. Proponents of LMSSBs often list improved safety over LIB technology due to the replacement of the flammable liquid electrolyte with an inflammable solid.

This argument largely ignores the impact on safety of adding lithium metal, which exothermically reacts with water to form hydrogen gas [41]. There is an extensive body of work on the safety performance of LIBs which has examined its mechanical [47, 48], thermal [49, 50], electrical [51, 52] and system level [53, 54] behavior. In contrast, this novel work performs a high level safety assessment of the LMSSB compared to LIB technology, and subsequently investigates the identified potential areas of concern for this new cell type.

1.2.1 Mechanical Properties of Lithium Metal

A literature review of the mechanical properties of lithium initially focused on the elastic constants given their foundational importance to mechanical behavior. Primary sources were identified for the elastic modulus (E) with methods including wire bend [55], single crystal [56, 57, 58, 59] acoustic resonance [60], load frame [61, 62] and DFT [63] (see **Figure 1.9**). Despite the large number of sources and methods, there was very little agreement on such fundamental physical properties. The four elastic constants are related to each other, and as a result, only two are independent. Most researchers measure one elastic constant and cite published accounts for the others, often leading to the inconsistent use of values to predict mechanical properties. For example in previous modeling work [64, 65] three separate values of the bulk modulus are used either directly or indirectly through citations for other constants; (1) based on the shear ($G = 3.4$ GPa) modulus and Poisson's ratio given ($\nu = 0.42$), a bulk modulus (K) of 20.1 GPa is required, (2) however there are citations [66] in this work which base their calculation on a K of 0.9 GPa and (3) other calculations cite another work which used $K = 11.1$ GPa [67]. A detailed description of how the lithium mechanical properties are used in models such as in reference 64 is shown in the Appendix [64].

Building a model using material constants derived by using three separate values for K (as one example) raises clear issues with real world fidelity. It was possible to find materials handbooks as secondary sources for the shear modulus (G) [66, 68] and the bulk modulus (K) [66, 67] but not their primary source [65, 68]. For the Poisson's ratio (ν), a collection of secondary source handbooks [66, 69] were found in the literature along with recalculations based on the other constants [55, 64, 65]. The lack of self-consistency and primary sources for elastic constants of lithium highlights the need for further study in this area.

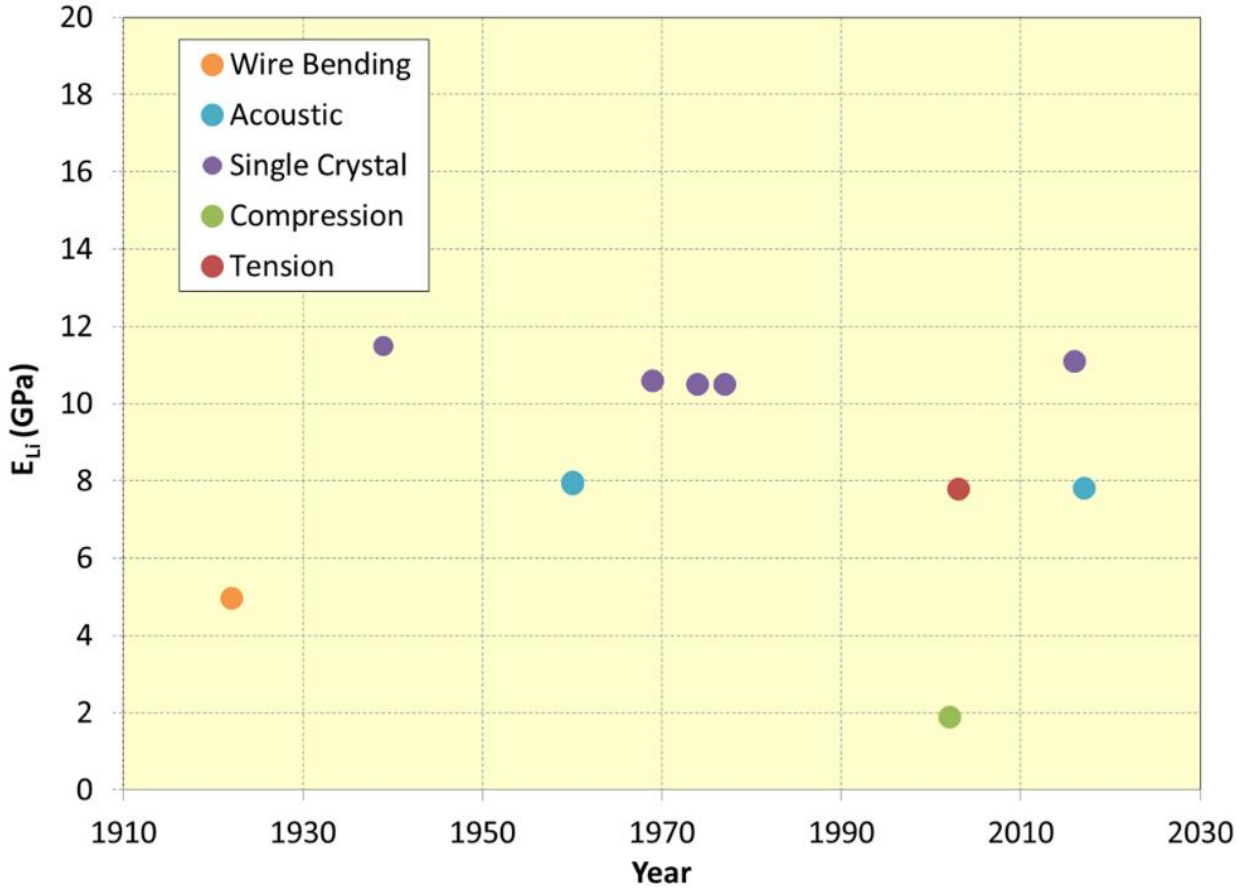

Figure 1.9: Historical Reporting of the Elastic Modulus of Lithium Metal [70]

While the elastic constants are critical for modeling the behavior of lithium, the dynamics of the interface under pressure during plating and stripping of lithium are controlled by the plastic behavior. Of particular interest in the design of lithium electrodes in LMSSB is the condition of yielding for which publication literature was also sparse. Two studies using conventional stress-strain analysis, one was in tension and the other in compression, were found with one containing inaccurate elastic modulus values (see **Figure 1.9**) [61, 62]. Also of significant relevance is the visco-elastic behavior of lithium at the required temperature range for automotive batteries of 52°C to -30°C, corresponding to a T_H of 0.72 to 0.54 [27]. Only one relevant compressive creep reference could be found for bulk lithium [71]. Based on the limited stress-strain data in tension and compression for elastic, plastic and visco-elastic deformation, this area was identified as in need of further study.

1.2.2 Safety Properties of Lithium Metal

In 2008, the first serial production LIB containing vehicle, the Mercedes S400 hybrid, was introduced, seventeen years after the first consumer electronics LIB [1, 19, 29]. Until this point, all automotive batteries were of either lead acid or nickel metal hydride chemistry [34]. These incumbent aqueous chemistries had comparatively lower energy density than LIB, but also significantly fewer safety concerns [33, 34]. The introduction of LIBs into vehicles in 2008 was preceded by significant safety research. Despite the effort to consider all possible aspects of this technology change, a subsequent safety incident in 2011 ignited significant governmental regulatory attention [72]. The result has been a broad documentation of mechanical [47, 48], thermal [49, 50], electrical [51, 52] and system level [53, 54] safety behavior of LIBs by both academic literature and industry studies. One such output of this research is a series of abuse

scenario boundary conditions for high severity events such as crush, overcharge, and short-circuit (see **Figure 1.10**) [53]. The assessment of specific LIB abuse responses has also been standardized by a common scoring system [73]. A variety of hazard assessment techniques have been established by the industry at either the battery [74], or functional safety level [75, 76]. In addition, the industry has also applied bottom up (Failure Mode and Effects Analysis, FMEA) [77] and top down (Fault Tree Analysis, FTA) [53, 78] failure determination techniques to LIBs. All of these safety studies and failure assessment techniques have resulted in a rich body of global industry safety standards [79, 80, 81] and regulatory requirements [82, 83, 84, 85, 86].

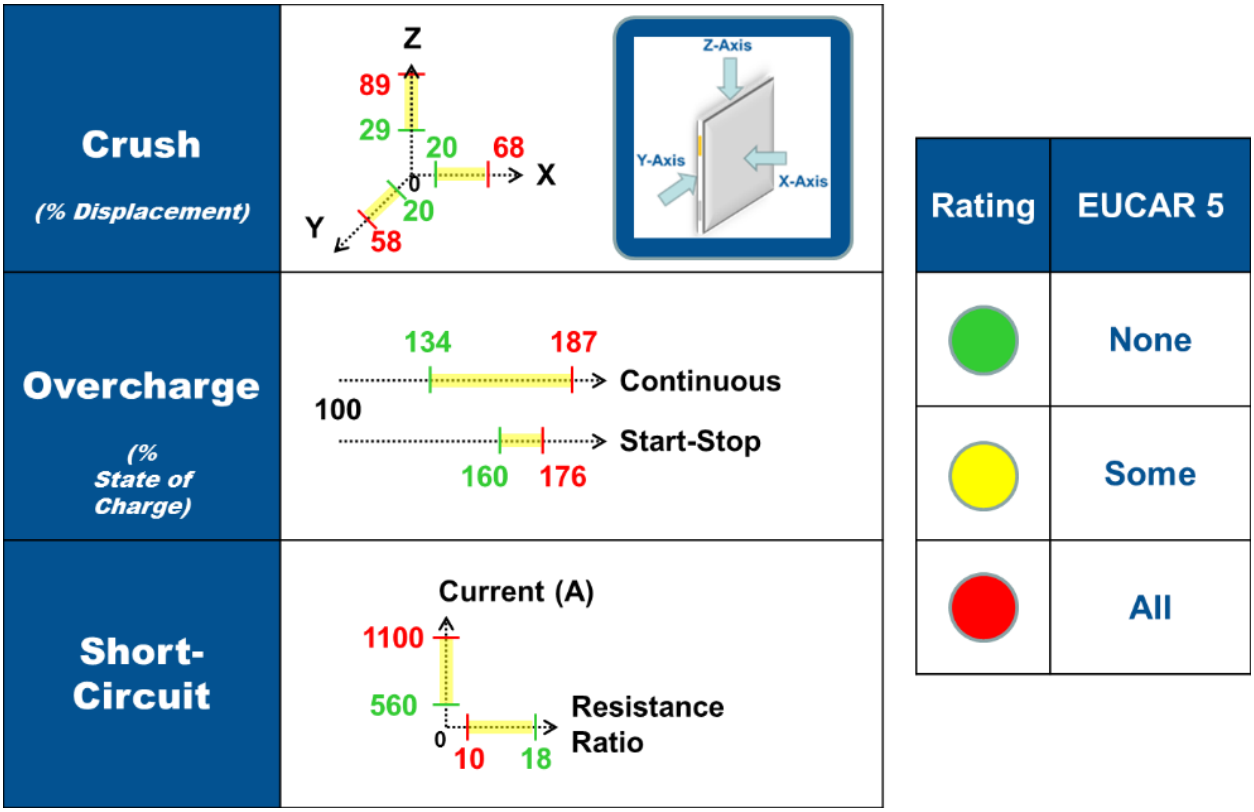

Figure 1.10: LIB EUCAR 5 (Fire) Based Safety Boundary Conditions for Crush, Overcharge and Short-circuit [53]

Currently, LMSSB are one of the leading candidate BLI battery technologies yet they remain in the research phase [87]. The introduction of LMSSB will require a revaluation of safety performance in EVs much as the introduction of LIBS in 2008 required. Almost none of the previously described studies, standards, or regulations consider the presence of lithium metal in the batteries under test. In recent years a small number of researchers have applied accelerated rate calorimetry (ARC), a thermal safety assessment tools developed for LIBs, to lithium metal cells [88, 89]. Additionally, while there has been a recent study that considered best safety practices for lithium metal battery researchers themselves [90], there has not been the same consideration given to the use of LMSSB outside the careful controlled research lab environment.

1.3 Dissertation Goals

The overall goal of this thesis research is to create an improved understanding of the mechanical and safety properties of lithium metal employed in lithium metal solid state batteries (LMSSB). LIB technology has significantly impacted the modern world [1, 2, 3, 4, 5], however its rate of evolutionary improvement has begun to slow down (see **Figure 1.5**). Among candidate next generation battery technologies being studied, the LMSSB holds the greatest potential [35, 36].

Lithium metal has been considered the holy grail of battery technology since its early experimentation in the 1960s and 1970s [91, 92, 93]. The high electronegativity of lithium which makes it appealing as part of an electrochemical couple has also made it difficult to harness is potential. The tendency of lithium to readily decompose liquid electrolytes and form dendrites after plating and stripping has limited its utility [94]. The advent of modern solid state electrolyte materials stable against lithium metal has renewed the potential of this anode technology [31].

Following the development of stable electrolyte/separator material, the main remaining challenge for the utilization of lithium metal is the dendrite issue and related safety issues [87]. It is the goal of this dissertation to further knowledge of lithium metal towards an improved understanding of its mechanical and safety behavior.

One goal of this research is to determine the elastic, plastic, and visco-elastic mechanical behavior of bulk lithium metal. A fundamental understanding of the mechanical behavior of lithium metal was found to be lacking in the literature. The elastic constants have been measured individually and inconsistently combined for the purposes of mechanics modeling [64, 65]. The literature had very limited elastic/plastic [61, 62] and visco-elastic [71] deformation experiments of lithium. Given the large quantity (see **Figure 1.7**) and important role which lithium metal itself plays in the LMSSB, establishing these basic properties is critical towards understanding more complicated behavior such as dendrite formation.

After establishing the overall mechanical behavior of lithium metal a second goal is to specifically examine the impact of LMSSB relevant sizing or aspect ratio, temperature and strain rates. The use of LMSSB batteries in automotive applications is the long term goal of this research and a study of the mechanical behavior of lithium in this particular environment is necessary. The initial fundamental mechanical study of lithium was performed at sample size scales or aspect ratios proscribed in standard materials testing [95, 96, 97]. A goal of this second mechanics study is to extend the elastic/plastic deformation of lithium metal to smaller and smaller aspect ratios better aligned with those likely to be found in future LMSSB designs. Additionally, one of the potential advantages of LMSSB is their reduced cooling needs compared to the incumbent LIB technology [94]. As a result the mechanical behavior of lithium at elevated temperatures was also of interest for study. Also in the automotive application environment fast charge and discharge

rates are to be expected which in a lithium metal anode system will correspond to quick plating and stripping events. Accordingly, the impact of elevated strain rates on the mechanical properties of lithium is of interest. The goal of this second study was a translation of three key material relevant environmental requirements of the automotive battery application into mechanical testing and analysis.

A final goal of this research is to perform a thorough safety assessment of potential faults in LMSSBs and then investigate the identified areas of concern, specifically air exposure, water exposure and vibration. Based on the challenging safety history of lithium metal batteries [1, 45, 46], adoption of a LMSSB design into automotive applications will need extensive safety study. Given the research nature of LMSSB, the top down Fault Tree Analysis (FTA) approach is the preferred safety assessment tool [53, 77]. The FTA constructed has yielded three potential faults of interest for further study, water exposure, air exposure and vibration. Water exposure in a lithium system has the potential for a severe safety event given the strongly exothermic nature of water and its generation of hydrogen gas [41]. However, an automotive relevant study of the water exposure potential fault needs to consider the manner and extent to which lithium metal may actually come into contact with water during an abuse scenario. An additional environmental exposure fault which was highlighted by the FTA was for moist air exposure. This identified fault was deemed to primarily take the form of a performance and quality issue once a study of its likely mechanism and severity in the automotive environment was assessed. The final identified fault of interest was vibration which in the automotive environment can be quite severe, potentially leading to cracking of brittle solid state separators and creating a short-circuit path for lithium metal to the cathode. The overall goal of this study to assess the safety challenges of lithium in a LMSSB

automotive application resulted in the thorough top down FTA and careful consideration of the three identified priority faults.

The research results are summarized below in three chapters, one each per published or draft journal manuscript. The approach and structure of each study and chapter is described in the following subsections.

1.3.1 Approach to Lithium Mechanics: Property Characterization Study

The following Chapter 3 will describe the initial general mechanical property investigation of elemental lithium metal. A visual layout of the key results in Chapter 3 is shown in **Figure 1.11**, including Section 3.2.1 determining the elastic constants' of lithium via acoustic resonance, Section 3.2.2 elastic & plastic and Section 3.2.3 & 3.2.4 visco-elastic deformation via mechanical load frames [42].

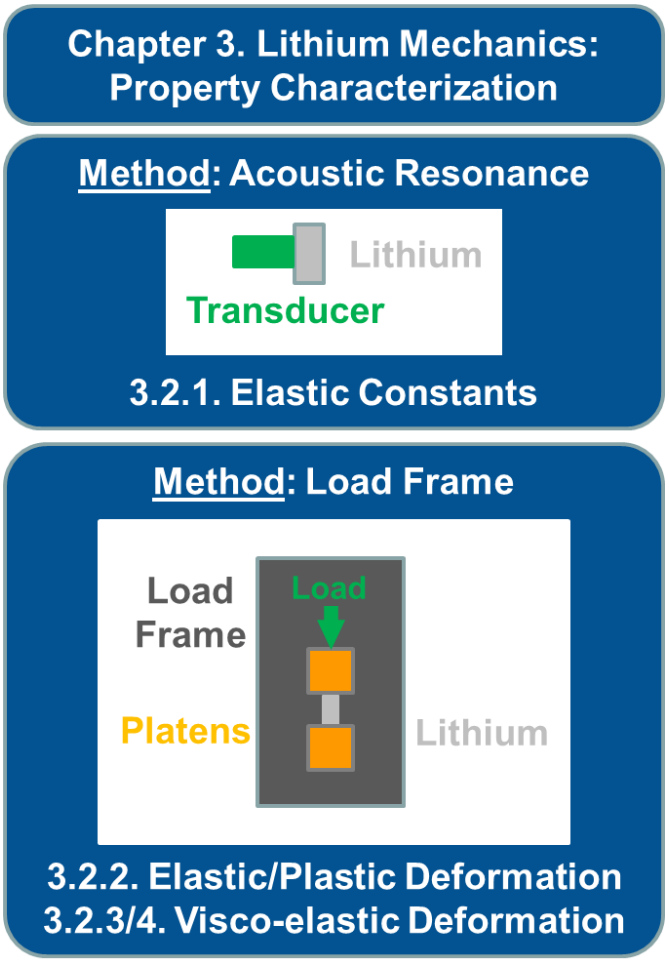

Figure 1.11: Visual Layout of Chapter 3: Lithium Mechanics: Property Characterization Study Results. Section 3.2.1 used acoustic resonance to determine the elastic constants of lithium. Section 3.2.2. applied constant strain rate uniaxial tension and compression to lithium to study the elastic and plastic behavior. Sections 3.2.3/4 studied the visco-elastic behavior of tension creep and compression deformation.

Section 3.2.1: Based on the literature, the previous mechanical characterization attempts of lithium metal included a wide range of reported elastic modulus (1.9 – 11.5 GPa) [56, 61] and very few primary sources for the shear modulus, bulk modulus and Poisson's ratio. Due to this uncertainty, our research approach was to use two complementary techniques (mechanical load frame and acoustic) on the same materials. Additionally, by performing measurements on both bulk rod and foil, this study spanned dimensions from those traditionally used for the evaluation

of structural materials to those more common in battery applications. To this end, both lithium rods (12.7 mm diameter) and foil (0.75 mm thickness) were utilized for the elastic constant determination using acoustic resonance (see **Figure 1.11**).

Section 3.2.2: Traditional stress-strain testing in uniaxial tension and compression is critical for the characterization of any new material (see **Figure 1.11**). Given the limited efforts in the literature using conventional testing in a load frame, this was the main approach chosen to determine the elastic, plastic and visco-elastic behavior [61, 62]. However given the wide range of elastic moduli seen even among these two references (1.9 – 7.8 GPa), acoustic resonance was also performed as a second, non-destructive and alternative technique to supplement the stress-strain curves of load-frame testing with separate elastic constant data. To maintain the purity of samples and results, both experimental systems were housed inside argon gloveboxes. This combination of bulk and foil lithium tested via load frames and acoustic resonance techniques provided an improved, holistic understanding of the mechanical properties of lithium metal.

Section 3.2.3/4: The time dependent response in tension (creep) and compression (deformation) was also studied in uniaxial stress-strain using a mechanical load frame (see **Figure 1.11**). Force was initially applied at a constant speed as in section 3.2.2 until a target load met and then the control strategy changed to constant load (see **Figure 2.1**). In the case of tension testing the strain rate declined into a plateau in the secondary creep phase until sufficient necking occurs to drive failure in the tertiary creep phase. A comparison of the secondary creep steady state strain rates as a function of load can provide information regarding a material's creep mechanism. In the case of compression deformation, the strain rate perpetually decays at constant load as the sample's surface area increases under compression. As a result, the compression deformation strain rate varies as a function of pressure and time.

1.3.2 Approach to Lithium Mechanics: LMSSB Sensitivities Study

The subsequent Chapter 4 will detail the LMSSB sensitivity focused study of lithium metal, including Section 4.1/2/3 the sensitivity of bulk lithium to sizing or aspect ratio (AR), temperature and strain rate (SR), Section 4.4 foil lithium & low aspect ratio sensitivity, and Section 4.5 multi-factor sensitivities & hydrostatic pinning (see **Figure 1.12**) [98].

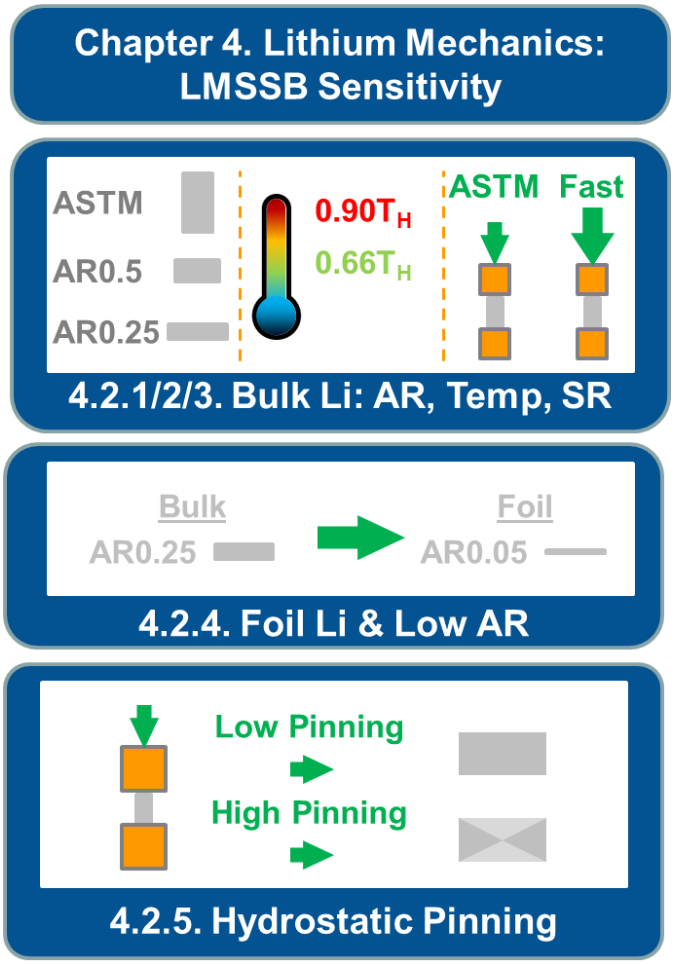

Figure 1.12: Visual Layout of Chapter 4: Lithium Mechanics: LMSSB Sensitivity Study Results. Sections 4.2.1/2/3 explored the sensitivity of bulk lithium to aspect ratio, temperature and strain rate. Section 4.2.4 extended the aspect ratio sensitivity study by using lithium foil. Section 4.2.5. explored the impact of multiple simultaneous sensitivities and proposed the theory of hydrostatic pinning to explain the observed mechanical behavior of lithium

Section 4.2.1/2/3: In an effort to extend the fundamental properties of lithium metal determined [42], a second mechanical study was carried out to explore the relevant environmental variables present in the LMSSB system. Specifically the impact of sizing or aspect ratio, temperature and strain rates on the behavior of lithium in compression (see Figure 1.12). The aspect ratio was varied using lithium rods across an order of magnitude from 2.10 to 0.31. Additionally the impact of temperature was studied from 0.66 to 0.90 T_H or 26 to 134°C. And finally the strain rate was tested across three orders of magnitude from the ASTM standard for compression of $1x10^{-3}$ s^{-1} up to 1 s^{-1}[95]. Our study found the resulting flow stress of lithium to vary by an order of magnitude (0.21 to 1.86 MPa) depending on the sample geometry, temperature and strain rate of compression. This behavior, particularly in temperature and strain rate compared favorably with other BCC metals [98].

Section 4.2.4: The sectioning & squaring technique used to prepare lithium rods could fabricate a minimum sample height of 3 mm before sample quality suffered. As a result, lithium foils were added to this study to extend the achievable values of AR from 0.25 to between AR0.045 and AR0.095 (see **Figure 1.12**). The reduced AR samples had significantly increased yield strengths in proportion to their sizing, with a maximum value of 2.4 MPa recorded, four times greater than AR2 samples.

Section 4.2.5: In seeking to explain the aspect ratio or sizing response of lithium we found strong alignment with the hydrostatic pinning behavior found in copper by Cook & Larke (see **Figure 1.12**) [99]. By exploring the sensitivity of lithium metal to aspect ratio, temperature and strain rates more likely to be found in the LMSSB system, we were able to extend our fundamental mechanical properties work into results more suitable for the design of practical LMSSBs.

1.3.3 Approach to Safety Assessment & Experimentation of LMSSB

The final body chapter, Chapter 5 delineates the lithium metal safety study, including Section 5.1 fault tree analysis, Section 5.2 water exposure, Section 5.3 air exposure and Section 5.4 vibration (see **Figure 1.13**).

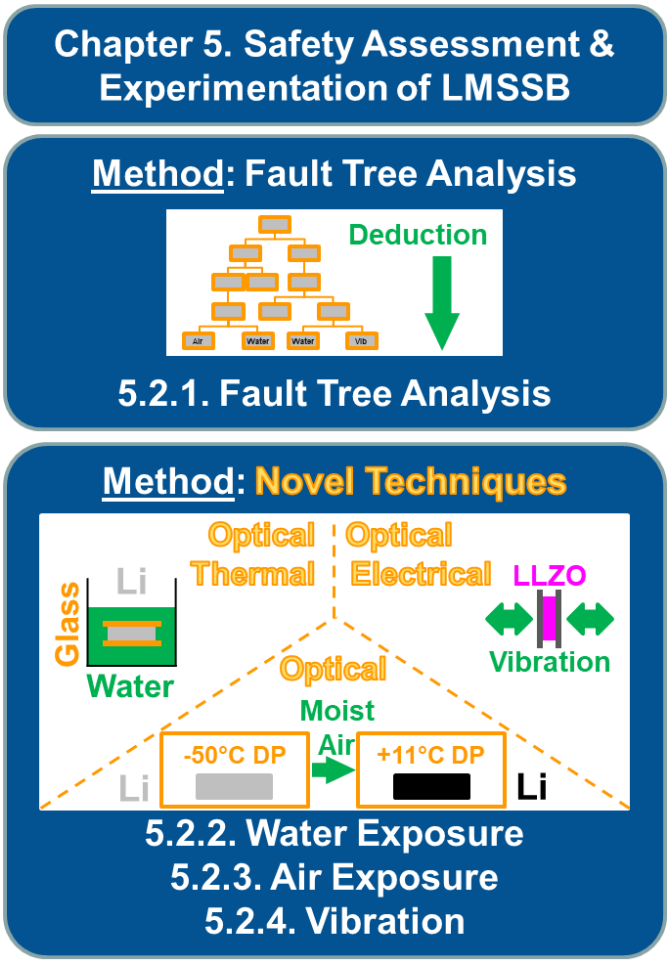

Figure 1.13: Visual Layout of Chapter 5: Safety Assessment & Experimentation of LMSSB Study Results. Section 5.2.1 describes the Fault Tree Analysis study done on the safety of lithium in the LMSSB system. Sections 5.2.2/3/4 developed novel experimentation techniques to study three key faults from the fault tree, water exposure, air exposure and vibration.

Section 5.2.1: Understanding the safety consequences of adding lithium metal to LMSSB required an approach that reconsidered all the existing battery safety assumptions of LIB

technology. To perform a thorough safety assessment, there are two common methodologies, Fault Tree Analysis (FTA) and Failure Mode and Effects Analysis (FMEA). The FTA approach is based on a top-down, deductive method to identify possible fault paths resulting in failure. FTAs start with general failure types and then deductively create downward fault paths capable of culminating in the original possible failures and are therefore well-suited to new generic designs [53]. FMEAs are bottom-up, inductive approaches that rely on the identification of specific, individual failure modes. As a technique, the true value of FMEAs is realized when it is possible to assign severities and probabilities to each unique failure and then create a specific set of engineering countermeasures [77]. Given the research nature of LMSSB, creating a FTA based on general design of a hypothetical battery was chosen as the preferred approach (see **Figure 1.13**).

Section 5.2.2, 5.2.3 & 5.2.4: The FTA scope specifically compared fault path changes due to transitioning from existing LIB to future LMSSB designs. The four main branches of faults identified were Mechanical, Thermal, Electrical and Chemical, aligning with a previous LIB FTA study [53]. Our study indicated that lithium metal's reactivity with liquid water and vapor figured prominently in the FTA faults. This instability of lithium metal was also compounded by the brittle nature of SS electrolytes made from ceramics or glasses. As a result, novel test procedures and evaluations criteria were created and tested for air exposure, water exposure and vibration for LMSSBs (see **Figure 1.13**).

Chapter 2

Experimental Methods

This chapter presents a description of the novel experimental procedures developed during the course of the work delineated in the following chapters. This includes details surrounding the lithium test materials and their preparation as well as a variety of mechanical and safety assessment and quantification procedures developed as part of this study.

2.1 Lithium Test Materials

Lithium (99.9% metals basis, 88ppm Ca, 19ppm Na) rods of 12.7 mm diameter were purchased (Alfa Aesar # 10773) and handled inside an argon glovebox (Vacuum Atmospheres Company Omni-Lab, <1ppm O_2 and H_2O) at approximately 26°C. It was assumed that the lithium was melt processed, thus was polycrystalline.

Depending on the test type, rod samples were initially prepared with aspect ratios (AR) of 1, 2 and 4 per ASTM standards [95, 96, 97]. Following the mechanical characterization of these AR sizes in both tension and compression [42], a second study examined reduced rod samples of ARs down to 0.25 in compression [98].

To prepare these lithium rod samples of specific height and diameter, a set of custom sized copper (McMaster-Carr # 8964K809, 110 copper alloy) forming jigs was used. Each individual copper die was bored to a specific diameter and various height copper spacers were fabricated to vary the jig depth when assembled. Once a lithium rod sample was set at the correct height, a variety of blades were used to section the excess lithium. The upper die wall was able to constrain

the movement of lithium metal at the sectioned interface. To achieve a specific height, several sectioning steps were used to progressively decrease the lithium height to the target while maintaining a squared profile. In between sectioning steps, the copper spacers were removed, allowing the entire lithium sample to be inserted into the copper jig. Once constrained on all sides, a custom copper rod plunger was inserted into the top of the die and hand compressed to further promote maintenance of the square profile. This iterative process of sectioning and squaring was repeated until the target height was approached. As the lithium samples' geometry approached their dimensional targets, a caliper (Mitutoyo 500-151-30) was used to confirm actual sizing. This sizing, combined with sample weights was used to calculate an apparent density which when compared with the theoretical density of lithium yielded the volumetric deviation from squareness of the samples. Each lithium sample was sectioned and squared until this geometric deviation was reduced to 2% or less. In the case of some samples, this required sectioning below the target height to achieve the proper squareness, accounting for the range in aspect ratios reported.

Lithium rod samples prepared in this manner for tension testing were mounted onto two copper rods (McMaster-Carr # 8966K14, 5/8" diameter 110 copper alloy) using a cyanoacrylate based adhesive (Henkel # 852882). These copper mounts provided an attachment location for the tension grips (Instron # 2710-205, Basic Screw Side Action Grips; Rated Capacity 5 kN). Lithium test samples for compression testing were lubricated with mineral oil (Alfa Aesar # J62592) to reduce friction and were mounted in between compression platens (Instron # 2501-083, Compression Platen with LVDT Mounting Holes, Rated Capacity 10 kN). The degree to which friction was reduced was not known, but it was assumed friction was not completely eliminated since barreling (increased mid-section diameter) occurred.

Lithium foil samples were cut to size using an arch punch in the argon glovebox environment. Some lithium foil samples were hand pressed to a target thickness using a borosilicate glass rolling pin (McMaster-Carr #8496K53) and sheet (McMaster-Carr #8476K47). To anneal lithium foil samples after roll pressing they were placed within a custom made copper jig and the whole assembly was heated on a hot plate in the glovebox environment at > 140°C (T_H > 0.91) for at least 2.5 hours.

During our experiments, the lithium samples never left the argon glovebox environment once opened. As a result, the lithium was not contaminated by air exposure. Upon compression, the newly revealed lithium metal surfaces did appear be more reflective than the lithium surfaces that were exposed prior to the testing. This is common in lithium even in a glovebox environment as completely preventing the passivation of a freshly cut lithium surface by atmosphere is not achievable even in this environment. However, our samples showed a variation of reflectivity that was mild and in no way suggested that anything more than a thin surface film was present. In the work of Schultz et al., they report that lithium a couple of decades old was tested in the open air environment, which although initially shiny after cutting, was a "dull grayish black" after two hours [61]. No such discoloration or contamination of our lithium sample was seen.

2.2 Mechanical Methods

The description of the mechanical test methods are divided into the acoustic methods used to non-destructively measure the elastic constants, the continuous stress-strain deformation in tension & compression to explore the yield strength, and flow stress and time dependent stress-strain methods used to study visco-elastic behavior.

2.2.1 Acoustic Characterization

An acoustic pulse echo technique was used to determine the elastic constants of lithium. Measurements were conducted in a glovebox wherein transducers were pressed against lithium to acquire acoustic spectra. The pulse-echo method [100, 101, 102] was used in which the transducer emits an acoustic wave that propagates through the material, reflects off the opposing surface and returns to impinge on the transducer. The acoustic wave velocity was determined by measuring the time between the initial pulse and the returning wave (echo) along with the sample height. Acoustic measurements were performed using an Olympus 5073R Pulse/Receiver (P/R) paired with a Picoscope 2207A PC based oscilloscope. An electrical impulse at 200Hz frequency repetition rate, 50Ω damping and energy ranging between 8-16 μJ was generated and received with a 39 dB gain. Longitudinal wave speeds were measured using an Olympus M110-RM contact transducer (operating at 5 MHz) coupled to lithium in an argon glovebox with mineral oil as a couplant. Similarly, shear wave speeds were measured using an Olympus V-156RM contact transducer (also operating at 5 MHz) coupled to lithium with Olympus SWC-2, also in the argon glove box environment. Lithium samples tested were all cylindrical of 12.7 mm diameter with varying heights between 0.75 and 12.3 mm. Wave speeds were calculated by measuring the sample height and the time in between acoustic peaks in resonance.

2.2.2 Continuous Speed Stress-Strain Characterization

2.2.2.1 Lithium Mechanics: Property Characterization Study

Stress-strain characterization in tension and compression was performed using a 2.0 kN mechanical load frame (Instron # 5944) and a 0.5 kN load cell (Instron # 2580-105) housed inside an argon-filled glovebox. Data acquisition (DAQ) frequency was set at 10 Hz (i.e. data

logging every 0.1sec) and every 1 N for yield strength tests. To limit the data file size while maintaining resolution, the DAQ triggers were set to 0.1 Hz (i.e. data logging every 10sec), every 0.3 N and 0.05 mm of displacement for the longer creep tests.

In the yield strength experiments the transition between elastic and plastic behavior was determined as the point where linearity is lost. In the absence of a well-defined criteria for loss of linearity, this point was determined as the point on the stress strain curve where a linear regression R^2 fit dropped below 0.99. Once the transition point to the plastic region is quantified, the stress-strain curve slope identifying Young's modulus can be calculated between this point and the start of the test. A comparison between Young's modulus values from literature with values estimated using the tension and compression stress-strain curves in this work resulted in inconsistencies, likely due to the highly ductile nature of lithium combined with the elasticity/rigidity of the load frame and corresponding load cell/grip setup. As the load frame actuates its motion, there is the opportunity for gear slip in the electric motors and slippage in the couplings between load cell, joints and ultimately grips. These issues are often found in load frame based testing and in our experimental setup were compounded by the lack of an extensometer. Tariq et al. [62] was able to perform load frame tension testing of lithium with an extensometer and measure Young's modulus values in agreement with pulse echo approaches [42, 60]. Schultz et al. [61] performed load frame compression testing of lithium without an extensometer and similar to our study measured Young's modulus values significantly lower than all literature references.

As a result, Young's modulus determined by the acoustic characterization method was used to determine the yield strength. The yield strength was determined by plotting Young's (from acoustic measurement) on the tensile stress-strain data and applying the 0.2 % strain offset method

[103]. All yield stress-strain experiments were conducted with a crosshead speed of 1 mm/sec, which corresponded to an average strain rate of 1.22×10^{-3} sec^{-1}. This strain rate was selected following a review of ASTM standards [95, 96, 97], which recommends the use of a crosshead speed that is in between 1.15 and 11.5 MPa/sec divided by the expected Young's modulus. A review of the lithium literature yields a span of Young's moduli between 1.9 and 10.6 GPa (see **Table 2.1**), giving a corresponding strain rate span of 0.11 to 6.05×10^{-3} sec^{-1}, with 1.22×10^{-3} sec^{-1} selected as a value which fell in the middle of this span and corresponded to a crosshead speed of 1 mm/sec.

Lithium samples with aspect ratios (AR) of approximately 1 were used in both tension and compression yield experiments during the first round of experiments [42]. These AR values were chosen as practical compromises between the 2 and 4 values proscribed by ASTM standards [95, 96] for compression and tension respectively, and the likely small ($\sim 1 \times 10^{-4}$) values to be found in an actual battery. For example, an electrode areal capacity of 4 mAh/cm^2 with a 50% excess lithium (to account for loss over time) would require a lithium thickness of only 30 um. Extending this electrode areal capacity target to approach battery capacity values commonly used in smart phones, hybrids and electric cars (2, 5, 60 Ah) would require large surface areas (500, 1,250, 15,000 cm^2), leading to correspondingly tiny ARs (1.2×10^{-4}, 7.5×10^{-5} and 2.2×10^{-5}).

Microstructure	E (GPa)	Method	Reference
Polycrystalline	5.0	Wire Bending	[55]
Polycrystalline	8.0	Acoustic	[60]
Polycrystalline	1.9	Compression	[61]
Polycrystalline	7.8	Tension	[62]
Polycrystalline	7.8	Acoustic	[42]
Single Crystal	10.6	Acoustic	[57]

Single Crystal	10.5	Acoustic	[58]
Single Crystal	10.5	Acoustic	[59]

Table 2.1: Young's Modulus of lithium from literature and this study (room temperature)

2.2.2.2 Lithium Mechanics: LMSSB Sensitivities

During the subsequent second round of study, only compression testing was performed but on bulk lithium samples of approximately AR 0.25 to AR 2.0 [98]. In addition to the shaping procedures implemented during lithium sample preparation (described in Section 2.1), further steps for alignment were undertaken during the pre-load stage of sample setup. Once a test sample had been loaded in between compression platens, a pre-load compression pattern was applied with computer controlled limit of 2.5N. A manual mechanical jog feature of the load frame was used to deliver the pre-load threshold value of 2.5N at least three times to the sample. The procedure was developed in previous testing [42] and was shown to significantly reduce the variability of the initial low stress/strain region of lithium's compression. During this second study as before the transition point between elastic and plastic behavior was determined as the point where linearity is lost, a criterion that is not well defined in the literature. For the second study [98], we defined this as the point on the stress strain curve where the linear regression R^2 quality of fit hit a maximum value (average of $R^2 = 0.9985$, occurring at 0.54 MPa and 3.02% for N = 81) and thereafter began to decline. Next it was necessary to determine the slope calculation start point, (average of 0.24 MPa, 1.93% strain N = 81) which was defined as the initial instance of stable data logging (i.e. not at the immediate t = 0 onset) and with a slope of approximately ~ 10 % of the maximum point slope (average of 36.9 MPa, N = 81). The slope determined by this method was then applied with a 0.2% offset to determine an intercept with the experimental data, identifying the elastic/plastic transition point (average of 0.84 MPa, 4.31% for N = 81).

The need to define a slope calculation start point instead of t = 0 is likely due to test artifacts from the experimental setup of the mechanical test frame. These artifacts are of small absolute magnitude but given the mechanical properties of lithium and the size of the test frame, of large importance to account for in these experiments. As the load frame actuates motion, there is the opportunity for gear slip in the electric motors and slippage in the couplings between load cell, joints and ultimately platens. Additionally, the Instron Load Frame 594x series has an axial stiffness of 8.5 kN/mm or less excluding the compression platens. At the maximum load value of 500N, this could translate to a displacement of 59 um [104]. When testing lithium of an AR2 and diameter of 12.7mm, this amounts of frame extension equals 0.2% of sample height. However when testing the 750um thick foil samples at the extreme load value of 500N, this level of stiffness amounts to 7.8% of sample height. These issues are often found in load frame-based testing and in our experimental setup were compounded by the lack of an extensometer. For small AR values (AR < 0.50), the slope calculation start point had to be increased (i.e. to 0.5 MPa and greater), this was likely due to the shrinking signal to noise ratio involved in using samples of smaller and smaller absolute height while maintaining the same test equipment mechanical load frame.

Lithium sample heating was provided by a variable transformer (Staco Energy Model # 3PN1010b) and heating cord combination (Briskheat Model # HTC451005) insulated with fiberglass sheets (McMaster-Carr Model # 9356K11). Target testing temperatures were determined by evenly spacing homologous temperature values between room temperature (T_H = 0.66) and the melting point (T_H = 1.00). Each individual compression platen was instrumented and allowed to achieve a temperature equilibrium for a minimum of 1 hour. Lithium samples were placed between both platens at a minimal load (< 2.5 N) for at least 3 minutes prior to test start to allow for thermal equilibrium. Given the > 1-hour pre-warming of the relatively large steel platens

compared to the lithium sample size, 3 minutes was enough for both platens to cool slightly (~1-2°C) and stabilize after warming the lithium. During the actual testing period, the temperature at each platen was noted at a minimum of 5-time intervals; the resulting 10 point or greater data was averaged and then reported as the test temperature.

The previously measured lithium creep behavior was seen to begin at approximately $1x10^{-4}$ s^{-1}[42]. As a result, we viewed the measured lithium creep rates as a practical speed minimum. Our test frame has a maximum speed of 2500 mm/min and considering our bulk lithium sample height range (2.88 to 26.71 mm), a maximum practical strain rate of 1.56 s^{-1}. This value was reduced by a safety margin to 1 s^{-1} and that value used as our speed maximum. Accordingly, values ranging from the ASTM strain rate of $1x10^{-3}$ to 1 s^{-1} were able to be evaluated in this study. The third sample strain rate was determined as the logarithmic mean ($3.16 x10^{-2}$ s^{-1}) between these two end points.

2.2.3 Time-dependent Stress-Strain Characterization

A similar experimental setup was also used to study the time-dependent deformation behavior in tension and compression, using a constant $1.0 x10^{-3}$ sec^{-1} strain rate to approach the target hold pressures. Once the target load was achieved, the load frame control mode changed from constant crosshead speed (strain rate) to constant load (pressure) (see **Figure 2.1**). Creep data was processed using a 100 point moving average to smooth the as-collected data. Tension creep performance was studied at loads below the 0.8 MPa yield point between 0.2 to 0.6 MPa, using lithium samples with ARs of approximately 4 (ASTM E8/E8M-16A [96]). Compression deformation testing was performed at stresses between 0.8 and 2.4 MPa, using samples with ARs of approximately 2 (ASTM E9-09 [95]). This covers the range of anticipated stack pressures that are required to achieve low and stable cell resistance [105, 106]. True stress-strain was calculated

only for the compression samples since, necking or a non-uniform reduction in area occurred in tension, which precludes the assumption that deformation occurred at constant volume.

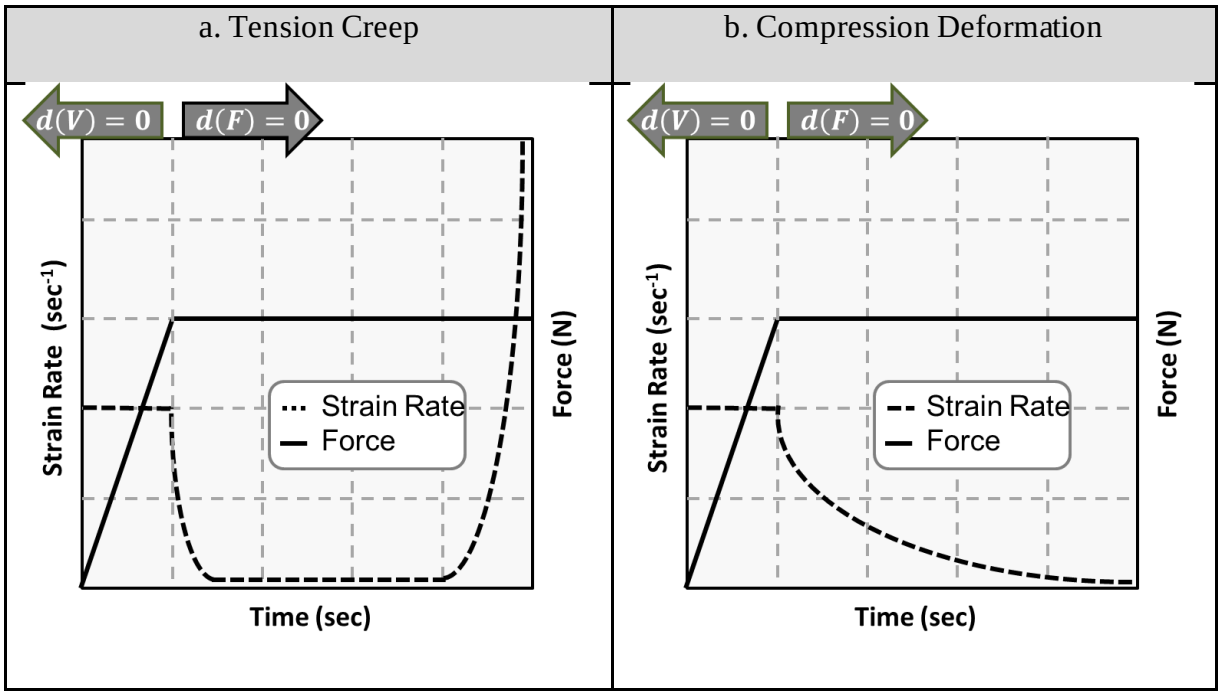

Figure 2.1: Schematic of representation of the strain rate and force as a function of time for the creep tension (a., left) and compression (b., right) test procedure

2.3 Safety Methods

The safety test methods section details the unique materials of these experiments as well as the Fault Tree Analysis (FTA) methodology and the evaluation techniques and methods developed to investigate the identified faults of interest from the FTA, namely water exposure, air exposure and vibration.

2.3.1 Materials

Lithium foil samples were purchased (750 um thick from Alfa Aesar) and handled (Argon glove box at 26C) as described previously. For safety experiments, the lithium was hand rolled

inside the glovebox using a borosilicate glass rod (McMaster-Carr #8496K53, ¾" diameter) and plate (McMaster-Carr #8476K47, 6" x 4" x 5/8"). Lithium safety experiments were either performed in a fume hood (Labconco) in the room environment or in a dry room (-50°C dew point). Standard commercial grade aluminum foil (Reynolds Wrap # 3591, 16um thick), phenolic resin lab table countertop and a white board (Quartet # UKTE2436-ECR) were used as reference for the purposes of surface reflectance.

2.3.2 Fault Tree Analysis

Improved safety is often touted as an inherent benefit of LMSSBs when compared to LIBs, often without any technical basis except for the removal of flammable liquid electrolytes. As a means to rigorously explore the safety implications of LMSSB designs when compared to LIBs we performed a Fault Tree Analysis (FTA). FTAs are top down, deductive approaches to failure mode analysis and are distinct from the more common, bottom up Failure Mode Effects Analysis (FMEA) performed in product design and validation. FTAs are more flexible at considering a general design approach and environment, whereas FMEAs require specific case studies and probabilities analysis, which is typically not possible in a research setting with a prototype cell. Our FTA of LMSSB was performed by concentrating on the changes points relative to a traditional LIB, an FTA of which was previously performed and published [53]. As in the case of the LIB FTA, the hazards were sorted into mechanical, electrical, thermal and chemical branches.

2.3.3 Water Exposure

Two different water exposure test chambers were fabricated from insulating Styrofoam and used to study the thermal and visual evolution of lithium metal. For both chambers, temperature

was recorded using a digital DAQ (Dataq Instruments # DI-245) connected to multiple K-type thermocouples (Omega # SA-3K-120-SRTC).

Chamber #1 was designed to hold a Pyrex glass bowl (300ml) for the water exposure experiments. Three different types of lithium samples were tested in chamber #1 using approximately 150ml of distilled water; bare, submerged and wrapped lithium. The bare lithium samples were comprised of lithium foil cut to size and allowed to float on the water surface. Submerged lithium samples were fabricated by bonding lithium to copper weights (McMaster-Carr # 8966K14) using a cyanoacrylate-based adhesive (Henkel # 852882). Wrapped lithium foil samples were placed between two microscope slides (AmScope # BS-50P-100S-22) held together by springs. Cell imagery was captured using a borescope (Depstech # 4331891326) in Chamber #1.

Chamber #2 was designed to hold a custom circular acrylic compression jig, fabricated from acrylic sheet stock (McMaster-Carr #8560K275) laser-cut to shape. In an effort to minimize the thermal soak time of Chamber #1, the amount of distilled water used was reduced to 75g and a magnetic stir bar added. The new circular jig was fabricated with visual hash marks at regular 2.5 mm intervals expanding outward from a 5.4 cm diameter center circle. This jig had 4 set screws for compression, set using a feeler gauge (McMaster-Carr #2334A66) for consistent opening dimensions all the way around. Lithium samples used for this jig were arch punched to 19 mm diameters from lithium foil and then centered in the circular jig. In Chamber #2 a set of optical lenses (Shuttermoon # SM100) attached to a smartphone and then backlight (Panther Vision BL-6885) using a button lamp to visually observe testing. The higher level of precision of the acrylic jig and improved image quality allowed for the development of optical image analysis,

which was performed by the ImageJ software to estimate the surface area of lithium consumption [107].

2.3.4 Air Exposure

The effects of air exposure on lithium were assessed by visual discoloration which accompanies the formation of a surface film attributed to reaction products such as lithium oxide, lithium nitride and lithium carbonate. Surface dullness measurements were used to quantify these observations and were performed using an optical orange peel and distinctness of image (DOI) tool (BYK-Gardner # 4840, Wave-Scan Dual) [108].

2.3.5 Vibration

For the vibration experiments, a custom vibration plate (McMaster-Carr # 9246K31) and restraints (McMaster-Carr #9246K483) were fabricated from 6061 aluminum sheet. The lithium lanthanum zirconia oxide (LLZO) samples were fixed at consistent pressure by using a torque wrench (CDI # 151SM) on four compression screws. A custom slip table (Unholtz-Dickie Corporation) was used to follow the UNECE R100, Appendix 8A Vibration test procedure. This procedure calls for a sinusoidal logarithmic frequency sweep from 7 to 50Hz with a maximum acceleration of $10 m/s^2$ at an acceleration over 7.5 minutes. This cycle is repeated 24 times for a total test time of 3 hours [84]. The R100 vibration pattern was modified to increase the maximum acceleration by factors of x2 and x4. Due to amplitude limits on the slip table, the starting frequency had to be raised to 10 and 12 Hz respectively for 20 and 40 m/s^2. Samples of LLZO were synthesized, pressed, cut and polished to form 1/2" diameter discs of solid electrolyte. Before and after vibration testing an in-situ electrical harness was added to the vibration plate to enable

electrochemical impedance spectroscopy (EIS) to be run by a Biologic VMP-300 machine. All samples were tested using a 10 mV fixed amplitude, single sine waveform from 0.5 Hz to 7MHz yielding 10 points per logarithmic decade.

Chapter 3

Elastic, Plastic and Creep Mechanical Properties of Lithium Metal

This chapter describes the determination of the elemental mechanical properties of lithium metal including elastic constants via acoustic resonance, as well as elastic/plastic & visco-elastic deformation via a mechanical load frame [42].

3.1 Introduction

Lithium metal solid state batteries (LMSSB) have garnered interest for their potential to dramatically improve performance compared to conventional lithium ion battery (LIB) technology [36]. By replacing the conventional graphite anode with lithium, an approximate 50% gain in cell energy density (Wh/l) compared to lithium ion could be achieved [35, 36]. However, the development of LMSSB requires a solid-state electrolyte that satisfies a myriad of physical and chemical criteria [109]. For example, according to existing mechanical models, solid electrolytes with a shear modulus $\geq 2G_{Li}$ (where G_{Li} is the shear modulus of lithium) should mechanically suppress lithium metal penetration [64, 65]. In another example, the fracture toughness of several ceramic electrolytes has been studied to assess the feasibility of manufacturing thin membranes that can prevent lithium metal penetration [110]. While the mechanical properties of solid electrolytes have been studied, little is known about the mechanical properties of metallic lithium.

Existing LIB cells and packs are typically held under compression to maintain their overall dimensions during use [29, 70]. Owing to the change in cell volume associated with the stripping

and plating of lithium, it is likely that compression will be even more important in LMSSB. Recent studies of all solid-state cells using lithium metal electrodes suggest that stack pressures in the 1.0 MPa range are necessary to achieve low and stable cell resistance [105, 106]. As a result, an understanding of the mechanical properties of lithium can assist in the design of LMSSB. Thus, there is a clear need to understand the elastic, plastic, and creep behavior of lithium to better determine the mechanical stability of the lithium-solid electrolyte interface

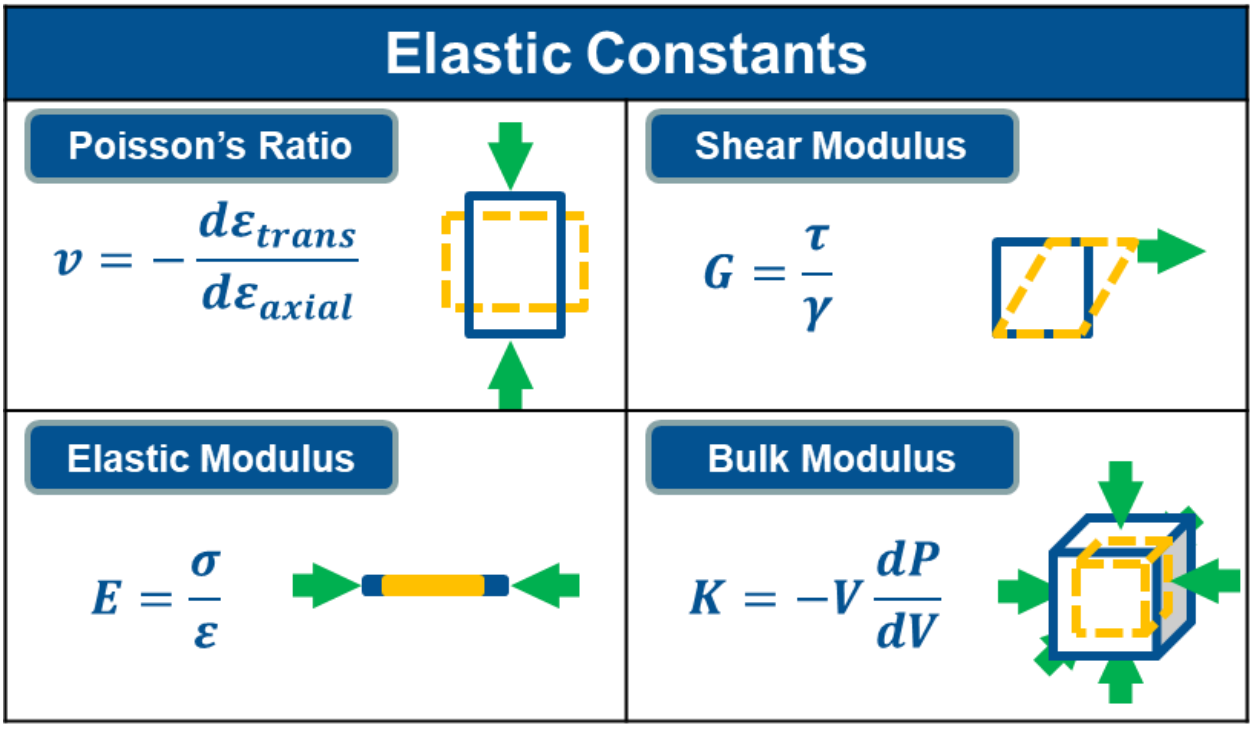

Figure 3.1: Definition and Schematic of the Four Elastic Constants

Previous studies of the elastic constants of lithium will often measure/calculate one or two constants then use literature values to obtain the other elastic constants (see **Figure 3.1**), at times resulting in values that are not self-consistent. As a result, the direct experimental measurement

of three elastic constants of lithium has not been performed previously. In this study, the Young's Modulus (E), Shear Modulus (G), and Poisson's ratio (v) were measured using acoustic analysis.

The yield strength and plastic deformation behavior of lithium metal is also not well characterized. For bulk lithium, the literature references are primarily limited to one study each of tension and compression [55, 61, 62, 111]. Reactivity with ambient air may have caused problems due to the formation of oxide/nitride surface layers during testing. In this study, a unique load frame was housed in an inert atmosphere (argon to prevent lithium reactivity under air) to characterize the deformation behavior of lithium. The stress-strain behavior was characterized in tension and compression to estimate the yield strength and plastic deformation properties. Once the yield strength of lithium was determined, the tensile and compressive time dependent deformation (creep) behavior was also characterized using the same unique load frame. The United States Advanced Battery Consortium (USABC), has published EV battery performance goals of 15 years with an operating temperature range of -30 to 52°C [27]. For lithium metal, these conditions represent a homologous temperature range (0.54-0.72) and time span under which significant creep is likely to occur. Thus, by varying the applied stress and measuring the strain rate response, it is possible to determine the creep mechanism and further provide a battery/vehicle designer additional information to predict the mechanical response of lithium metal anodes while in use. Due to these various vehicle-related conditions, understanding the elastic constants, yield strength and creep behavior of lithium metal is critical to the successful implementation of lithium metal anodes in LMSSB.

3.2 Results & Discussion

3.2.1 Elastic Constants

Longitudinal and shear wave transducers were used to measure Young's (E) and shear (G) moduli, respectively. E, G, and Poisson's ratio (ν) were determined using the respective wave speeds (V_l: longitudinal wave velocity; V_s: shear wave velocity) and the density (ρ) as in Equations 3.1, 3.2 and 3.3 [100, 102].

$$E = 2\rho V_s^2(1+\nu) \tag{3.1}$$

$$G = \rho V_s^2 \tag{3.2}$$

$$\nu = \frac{1 - 2\left(\frac{V_s}{V_l}\right)^2}{2 - 2\left(\frac{V_s}{V_l}\right)^2} \tag{3.3}$$

Furthermore, the bulk (K) modulus can be determined using the elastic constants calculated in Equations 3.1, 3.2 and 3.3 assuming isotropic behavior and Equation 3.4.

$$K = \frac{E}{3(1-2\nu)} \tag{3.4}$$

To assure attenuation or scattering at the interface between the transducer and the sample did not affect the measurement, the acoustic analysis was conducted for three sample heights (0.75, 8.83, and 12.35 mm, see **Table 3.1**). The elastic constants were found to be independent of sample size as to be expected when measuring an intrinsic material property (see **Figure 3.2**). From these data, average values for E, G, and K were determined to be 7.82, 2.83, and 11.1 GPa, respectively

(**Table 3.1**). The average Poisson's ratio was determined to be 0.381 (**Table 3.1**). To our knowledge, this is the first report of E, G, K, and v on the same lithium sample.

Height (mm)	Density, ρ(g/cc)	Wave Speed (km/sec)		E (GPa)	G (GPa)	K (GPa)	V
		Longitudinal, V_l	Shear, V_s				
12.35	0.53	5.27 ± 0.01 (N=4)	2.29 ± 0.01 (N=4)	7.80	2.82	11.18	0.38
8.83	0.54	5.48 ± 0.02 (N=6)	2.30 ± 0.02 (N=6)	7.79	2.80	12.12	0.39
0.75	0.53	5.08 ± 0.26 (N=6)	2.32 ± 0.02 (N=10)	7.88	2.88	9.92	0.37
Average				7.82	2.83	11.07	0.38

Table 3.1: Elastic properties of polycrystalline lithium at room temperature as measured by a pulse echo acoustic technique inside an argon glovebox

The elastic properties of lithium metal are important to understand the mechanical stability of the lithium-solid electrolyte interface in LMSSB. For example, Monroe and Newman estimated that the shear modulus of a solid electrolyte must be $\geq$ 2 times greater than lithium to prevent lithium metal dendrite/filament propagation [64]. In addition, recent analysis of the relatively high adhesion strength between lithium and solid electrolyte [106, 112] may also indicate that the elastic properties of lithium are important to consider when predicting stresses at these interfaces.

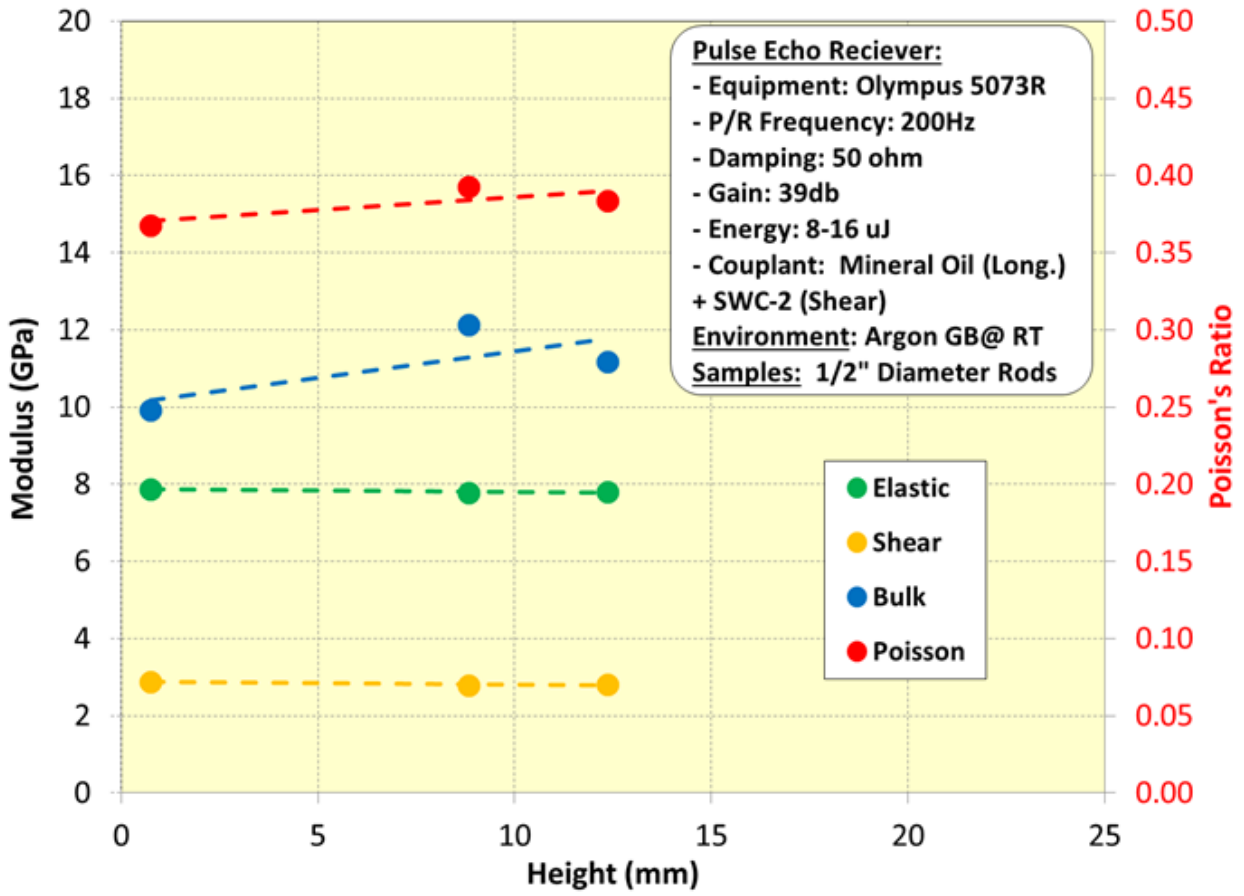

Figure 3.2: Elastic constants of lithium measured via acoustic pulse echo

Unfortunately, there have been few studies that characterize the elastic properties of lithium. Moreover, among the previous studies (see **Table 2.1**), it can be seen that there is notable disagreement in E values as they are more or less divided into two groups ranging between 7.8 to 8.0 and 10.5 to 10.6 GPa, and a couple of outliers at 1.9 and 5.0 GPa. The literature also contains E lithium values in a couple of reference books at 4.9 GPa but they are omitted from **Table 2.1** as their test method and conditions are not readily available [66, 68]. The E measured in this work is in excellent agreement with the other polycrystalline lithium measurements [60, 62], despite the use of different measurement techniques. For example, Robertson et al. [60] used acoustic measurements, while Tariq et al. [62] used tensile stress vs strain analysis to obtain E values of 8.0

and 7.8 GPa, respectively. Shultz et al. [61] used tensile testing and obtained an E of 1.9 GPa, however, it was believed that inadequate strain measurement accuracy likely resulted in values approximately four times lower than Tariq et al. [62] who used tensile testing along with an extensometer.

It is interesting to note that the higher E range was always measured on single crystals samples. Thus, we believe the form of lithium, i.e. polycrystalline or single crystal, distinguishes the two ranges of E. The polycrystalline E values comprise the lower E values while the single crystal values comprise the higher E values. Such a difference might be expected since the polycrystalline values are associated with an average value that includes multiple crystallographic orientations whereas the single crystal values are associated with a specific crystallographic direction. It is known that body-center-cubic (bcc) lithium is anisotropic [103, 113]. The Zener anisotropy ratio, A, ($A=2C_{44}/ (C_{11}-C_{12})$ where C_{44}, C_{11} and C_{12} are the elastic constants) is 8.43 compared to unity for an isotropic cubic single crystal [103, 113]. Thus, a difference is expected in modulus values between a polycrystalline and single crystal samples as is observed (Table 2.1).

3.2.2 Stress-Strain Behavior at Constant Strain Rate

3.2.2.1 Tension

The elastic and plastic deformation of lithium was studied by analyzing stress-strain behavior in tension at fixed strain rate (**Figure 3.3**). From **Figure 3.3** it was observed that initially there was a steep and linear increase in stress with increasing strain up to approximately 0.8 MPa stress and 0.4% strain. The slope of the stress-strain curve was determined to be 0.43 GPa (**Figure 3.3** inset) when extrapolating between the origin and the point at which the slope deviates from linearity (loss of linearity ($R^2 < 99\%$) was calculated as 0.40 ± 0.02 GPa).

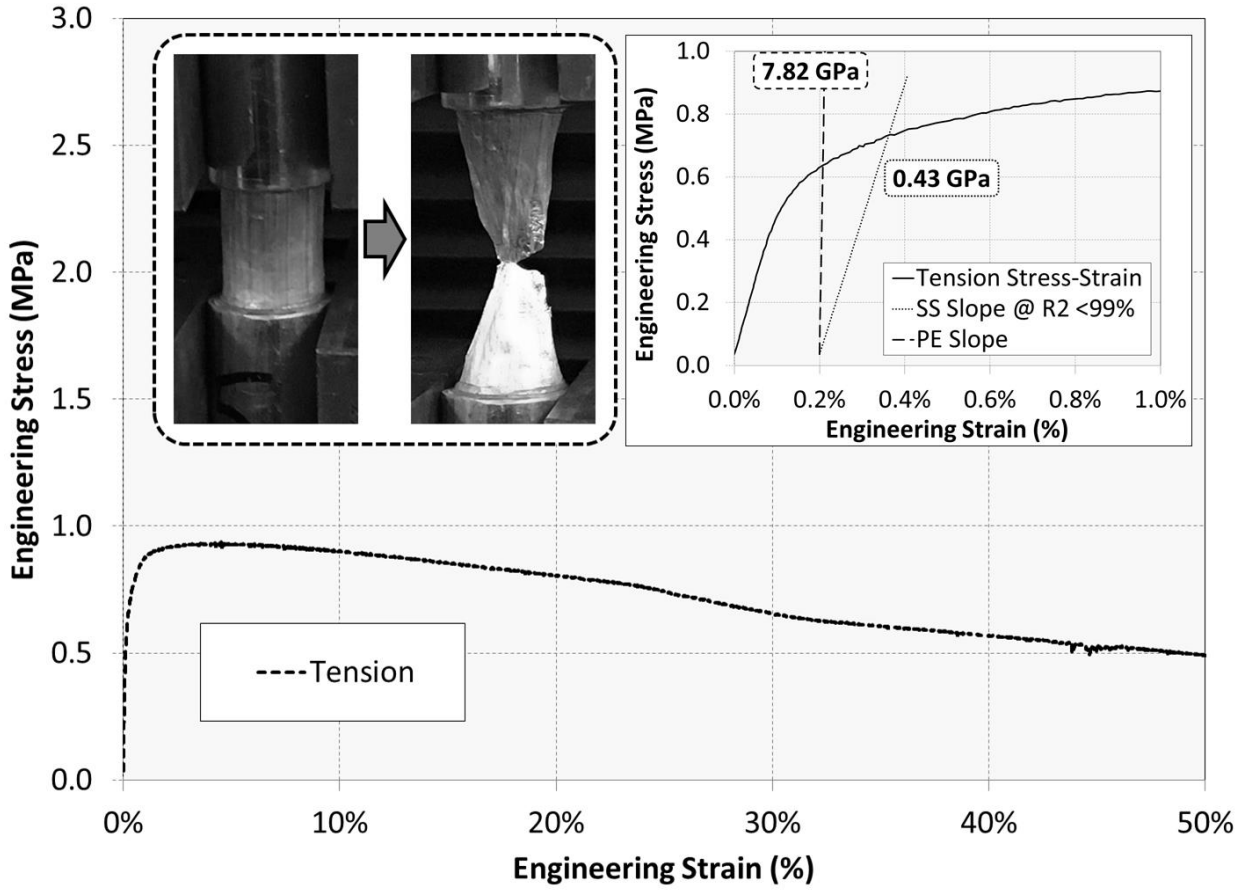

Figure 3.3: Room temperature tensile stress-strain behavior of lithium (15.5 mm height, 12.7 mm diameter, Sample # 170814.1). The inset shows the 0.2 % yield strength using the elastic modulus from the stress-strain curve (SS Slope) and pulse-echo acoustic measurements (PE Slope).

For comparison, the E taken from the acoustic measurement (7.82 GPa) is also plotted (**Figure 3.3** inset). Clearly the E estimated from the stress-strain curve is far lower than the E determined using acoustic measurements or the literature values (**Table 2.1**). Because it was difficult to determine which E to use, both values for E from (**Figure 3.3** inset) were used to estimate the yield strength using the 0.2% strain offset method. The yield stress was estimated to be 0.81 and 0.73 MPa (**Table 3.2**) when using E values of 7.82 and 0.43 GPa, respectively. These

yield strength values are in good agreement with literature values for polycrystalline lithium tested in tension (Table 3.2). At strains greater than 0.4%, the stress continuously decreased. From the inset in **Figure 3.3** it can be observed that significant plastic deformation was observed prior to fracture, confirming the ductile nature of lithium.

Microstructure	Method	$\dot{\varepsilon}$ ($x10^{-3}$ sec^{-1})	AR	σ_y (MPa)	Reference
Polycrystalline	Tension	0.11	10.6	0.60	[114]
Polycrystalline	Tension	2.0	N/A	0.76	[62]
*Polycrystalline	Tension (SS)	1.21	1.10	0.81	[42]
**Polycrystalline	Tension (PE)	1.21	1.10	0.73	[42]
Polycrystalline	Compression	1.67	2.07	0.64	[61]
Polycrystalline	Compression	5	3-5	15 – 105	[116]
Single Crystal	Tension	0.19	N/A	0.3	[115]
Single Crystal	Tension	0.2	N/A	0.2	[111]

Table 3.2: Yield Strength (σ_y) of lithium from literature and this study (room temperature). * σ_y estimated using E from slope of the stress-strain (SS) curve. ** σ_y estimated using E using slope from pulse-echo (PE) acoustic measurement

3.2.2.2 Compression

A dramatic difference in stress-strain behavior was observed when comparing tension vs compression. Representative plots of both the engineering and true stress-strain behavior of lithium in compression are shown in **Figure 3.4**.

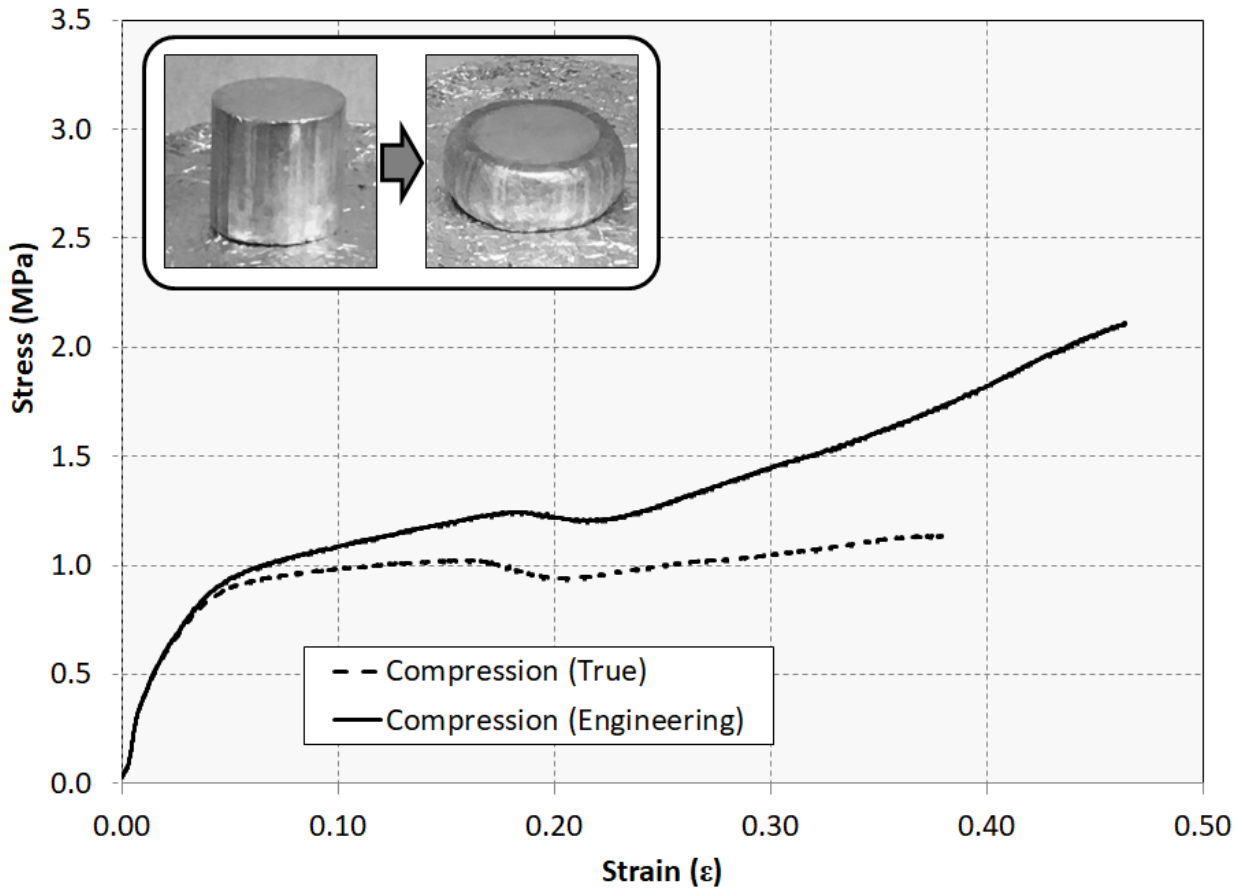

Figure 3.4: Room temperature compressive stress-strain behavior of lithium (12.3 mm height, 12.7 mm diameter, Sample # 170808.12)

As was done for tensile testing, the engineering stress-strain values were determined using the original sample dimensions. Since plastic deformation is a constant volume process (initial length x initial area = final length x final area), the instantaneous area could be estimated using the instantaneous sample height [103]. Using visual observation (**Figure 3.4** inset) it was also assumed that the instantaneous change in area was uniform along the longitudinal axis. Based on these assumptions, the following relation between engineering stress (σ_n) and strain (ε_n) to true stress (σ_t) and strain (ε_t) is shown in Equations 3.5 and 3.6. It should be noted that in calculating true stress, the engineering strain is added to unity in tension and subtracted in compression to account

for the shrinking or growing surface area (Equation 3.5). From these equations the true stress-strain curve was determined. By comparing engineering and true stress-strain behavior, it was clear that the true stress subtly increased compared to the engineering strain above ~ 5% strain, then dramatically increased above ~ 20%.

$$\boldsymbol{\sigma_t = \sigma_n(1 \pm \varepsilon_n)} \quad 3.5$$

$$\boldsymbol{\varepsilon_t = \ln(1 + \varepsilon_n)} \quad 3.6$$

In addition to the comparison between engineering and true stress, the shape of the compression curves were different compared to the tension curves. First, rather than a steep initial increase in stress with increasing strain, a gradual and non-linear increase in strain was observed between 0 to 3.93% ± 1.98% and up to a stress of 0.81 ± 0.10 MPa. The slope of this region is 30.5 ± 16.6 MPa and is characterized by an initial S-curve behavior (< 1 % strain), which was seen in all samples. Similar to what was observed in tension, we believe the highly ductile and relatively low E of lithium creates artifacts at low strains, e.g., load frame backlash and/or inhomogeneous sample-platen interface contact. Similar complications were observed by Shultz et al. [61] who characterized the stress-strain behavior of lithium. Second, ostensibly this inflection point at ~ 4 % strain could mark the transition between elastic and plastic behavior, however this would require the slope between 0 to 3.93% ± 1.98% strain to match that of the elastic modulus (7.8 GPa, see **Table 2.1** and **Table 3.1**). Clearly, it does not match, thus interpreting this inflection point as the yield point is incorrect. Third, the stress more-or-less continuously increased with increasing strain up to approximately 19 and 21% strain for the true and engineering stress-strain curves, respectively. Fourth, the slope of the stress-strain curve increases above 19 and 21%, for the

engineering and true stress-strain curves up to the point that the maximum measurable force was reached. The origin of the slight drop in stress between 18 and 22% strain is not known at this time, but similar behavior was observed in all four samples tested.

3.2.2.3 Tension and compression deformation comparison

In tension, lithium's behavior is similar to what is observed in highly ductile materials that do not work harden [103, 113]. In highly ductile materials, typically it is seen that as strain increases, first yielding occurs, followed by constant stress deformation, then a drop in stress due to necking, and ultimately fracture. However, in compression the stress required to increase strain continuously increased. We believe the lithium deformation behavior observed in compression in this work is similar to what was previously observed when testing highly ductile materials in compression [99]. For example, Cook and Larke [99] made similar observations when characterizing the deformation of highly-ductile copper in compression. In their work, the shape of the compression stress vs strain behavior was nearly identical to this work where two inflection points distinguished three strain regions and the stress generally increased with increasing strain. It was determined that frictional forces between load frame platens and the sample faces and the low sample aspect ratio, resulted in inhomogeneous deformation (barreling) which affected interpretation of the stress-strain behavior (**Figure 3.5**).

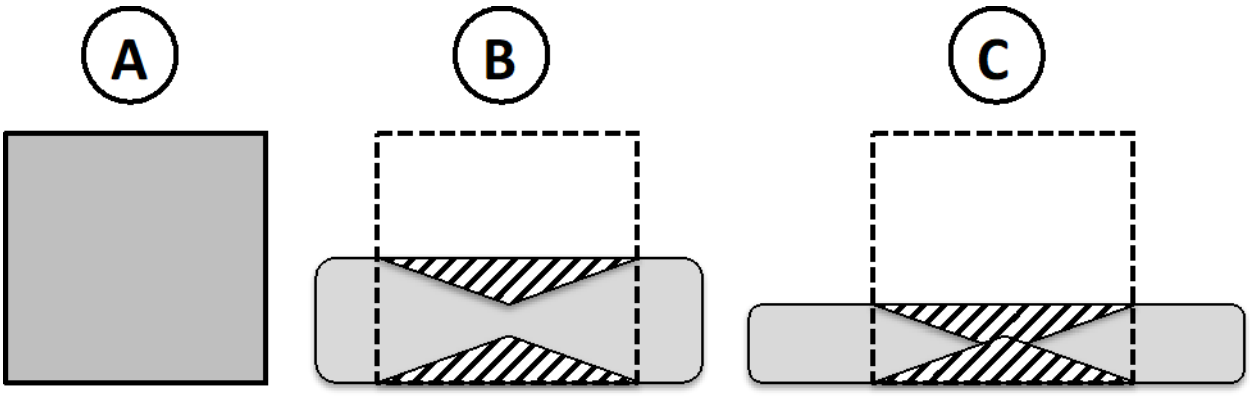

Figure 3.5: Schematic diagram depicting the evolution of a highly ductile sample geometry (barreling) during compression. The cross-hatched regions indicate where limited deformation occurs adjacent to the platens due to friction. A) original sample geometry, B) reduction in sample aspect ratio, and C) further reduction in aspect ratio to the extent that cross-hatched regions overlap. Adapted from [99].

In the initial region (between 0 - ~4% strain), homogenous deformation occurs. In the second region (between 4 - ~ 20% strain), frictional forces between the load frame platens and the sample faces prevent material flow (cross-hatched area representing hydrostatic regions **Figure 3.5b**) while the remainder of the sample volume freely flows (none cross-hatched area **Figure 3.5b**) causing the barreling effect. In the third region (between ~ 20% and the maximum strain), either the increase in cross-section area and/or the hydrostatic region overlap (**Figure 3.5c**) can combine to increase the stress required for further deformation. It was estimated that the contact area between the platens and the samples increased by approximately 25% (**Figure 3.5** inset). The increase in contact area confirms that that frictional forces likely played a role in affecting the stress-strain behavior. As mentioned by Cook and Larke [99], the magnitude of the frictional force and the sample aspect ratio affects the stress-strain behavior. These parameters go outside the scope of this work, but future studies should further investigate these effects.

3.2.2.4 Yield Strength Comparisons

A review of the literature reveals similarities and contrast in measuring yield strength (**Table 3.2**). First, in general the yield stress for tensile and compression testing are similar. Secondly, the yield stress for the polycrystalline samples is higher than that for the single crystals. This is expected due to the presence of grain boundaries acting as obstacles to dislocation motion, leading to increased strength [103, 113]. For example, the lowest two reported values (0.2 & 0.3 MPa) are both found in single crystal studies [111, 115]. Conversely, the largest measured yield strengths (15-105MPa at 298K) were reported in polycrystalline samples at sub-micron diameter size dimensions [116]. Despite a wide spread in methods (compression vs tension), aspect ratios (1.1-10.6) and strain rates (0.11-2.0 x 10^{-3} sec^{-1}) the polycrystalline measurements of micrometer size dimensions are observed over a small range (0.60-0.81MPa) [61, 62, 114]. Unlike elastic properties, the yield stress is dependent on microstructural features such as; grain size. Thus, reasons for the range of yield stress in literature could be a result of a difference in grain size. In addition, it could be due to a difference in the type of impurities and their concentration. Without knowledge of these variables it is not possible to explain the differences between the various studies. In addition, strain rate could affect the yield stress at room temperature, as observed by Tariq et al. [62].

3.2.3 Creep (Tension)

Given the low melting temperature of lithium (T_m=180.5°C =453.5 K) it is likely that the lithium metal anode will experience significant creep if held under tension or compression loading. The lithium creep behavior under tension and compression loading at room temperature (0.66

T/T_m) was investigated using the procedure described in Chapter 2. Tension creep was used to study the materials intrinsic behavior since, it does not suffer friction effects between the platens as observed in compression which can lead to inhomogeneous deformation resulting in specimen barreling, which will affect interpretation of the creep data as described in more detail in the next section.

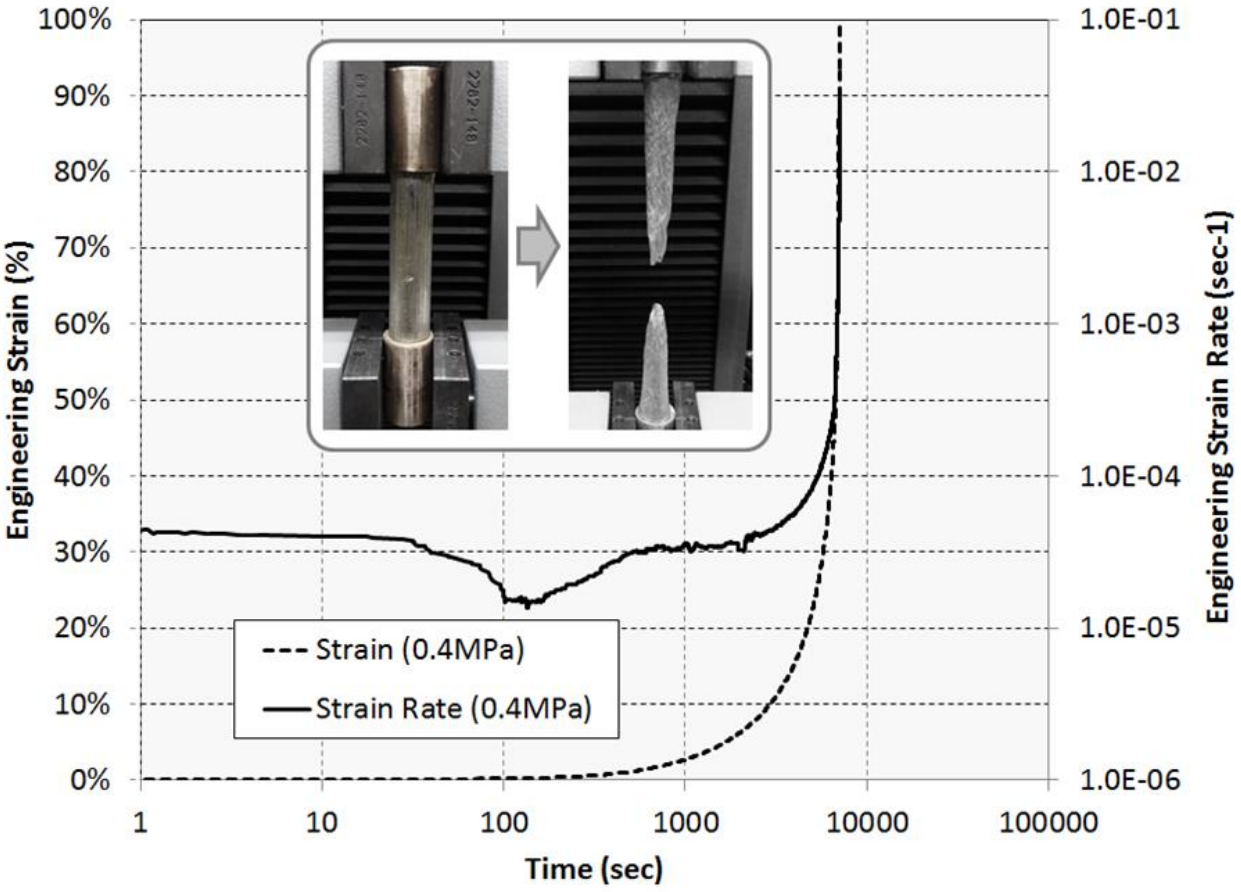

Figure 3.6: Room temperature tensile strain and strain-rate of lithium versus time.

A typical creep curve for tension loading at room temperature is shown in **Figure 3.6**. From **Figure 3.6**, several important points are noted. First, after about 135 s the strain rate reaches a minimum. Second, after 2,592 seconds the strain rate continually increases until failure occurs.

From the inset in **Figure 3.6**, it can be see that the sample necks down to a point indicative of a highly ductile material. The shape of the creep curve from **Figure 3.6** is in excellent agreement with those observed for ductile metals at high temperatures except typically a decreasing strain rate (primary region) is observed prior to the region where a minimum or steady-state creep rate is exhibited [71]. However, a primary region was not observed in this study, which could be attributed to the lack of work hardening as observed in the yield analysis. In the testing method used here, the transition from constant speed to constant load occurs rather suddenly in tension and leads to distortion in the calculated strain rate as the load frame changes control logic thus, making observation of the primary creep region difficult.

The creep mechanism for a material in general can be determined from the following equation 3.7 [71]:

$$\dot{\varepsilon} = A\sigma^{n} d^{-p} e^{\frac{-Q_c}{RT}} \qquad 3.7$$

Where $\dot{\varepsilon}$ is the minimum or steady-steady strain rate, A is a constant, σ is the stress, n is the stress exponent, d is the grain size, p is the grain size exponent, Q_c is the activation energy for creep, T is absolute temperature and R is the gas constant The creep mechanism can be determined by comparing experimental values of n and p and Q_c to theoretical predictions. For creep above T/T_m >0.5 the stress exponent is typically in the range of 1 or 3-7 [71]. An n value close to unity suggests creep is controlled by diffusional flow whereas for n values between 3-7, creep is controlled by a dislocation mechanism [71]. An n ≈3 is for creep controlled by dislocation glide whereas n ≈ 5-7 is for creep controlled dislocation climb. For n=1, p can be either 2 for creep controlled by lattice diffusion or 3 for creep controlled by grain boundary diffusion. For dislocation

mechanisms p is typically zero since, they are in general not dependent on grain size [71]. Q_c is typically related to the activation for lattice diffusion for diffusional flow and dislocation climb mechanisms, where transport is through the grain. In the case of diffusional flow controlled by grain boundary transport, Q_c is related to the activation energy for grain boundary diffusion.

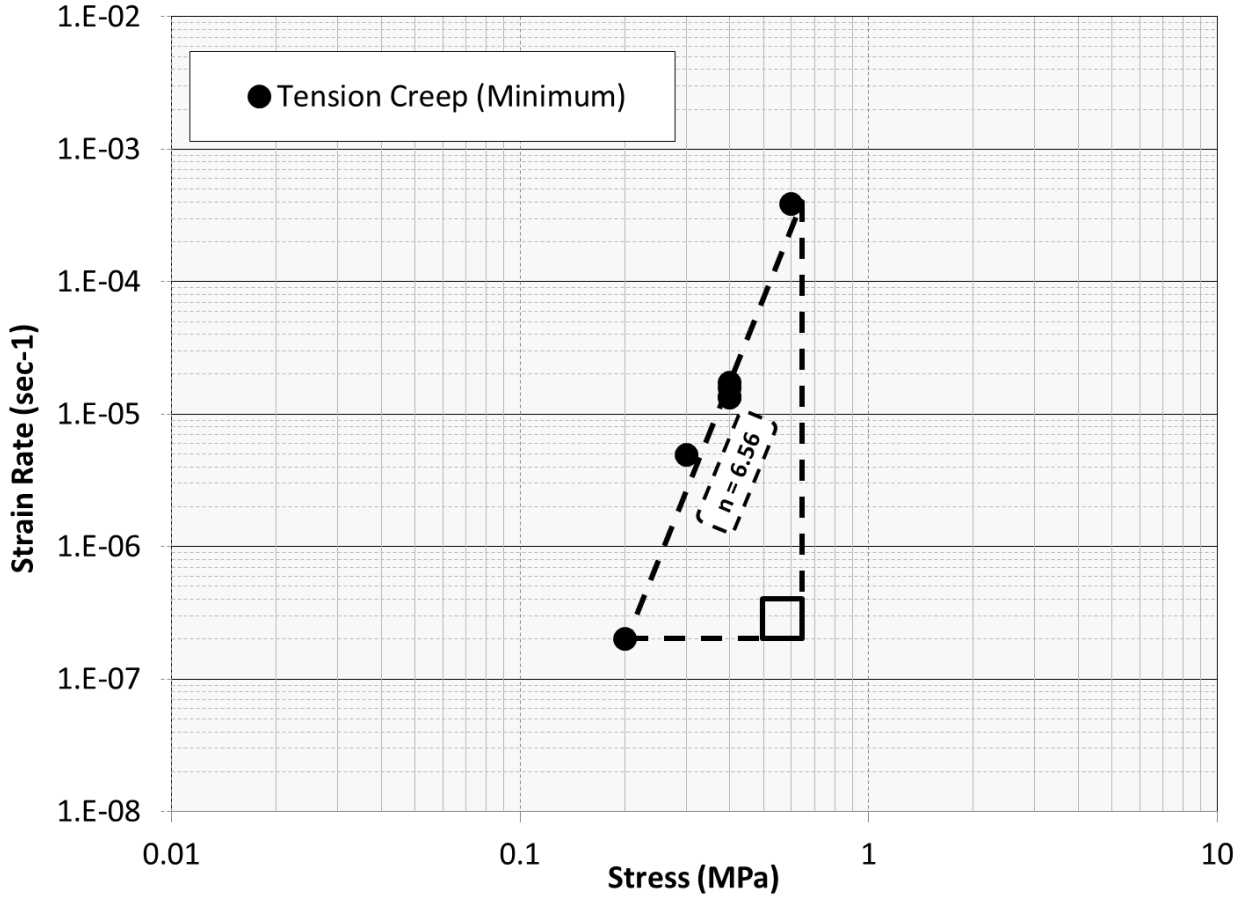

Figure 3.7: Minimum tensile strain-rate of lithium versus stress at room temperature.

The logarithm of minimum strain rate of lithium at room temperature is reported in **Table 3.3** and plotted as a function of the logarithm of stress in **Figure 3.7**. The slope of the curve yields the stress exponent equal to 6.56. This value suggests that the creep of lithium is controlled by dislocation climb [71]. Further confirmation of a dislocation controlled creep mechanism for

lithium is that fact the stress normalized with respect to the shear modulus (σ/G) for lithium is 2.2 $x10^{-4}$ at the low stress level and 7.1 x 10^{-5} at the high stress level, which is within the typical range where dislocation creep is exhibited [71]. At σ/G levels below about 10^{-4} diffusional creep mechanisms are rate-controlling, while at σ/G levels above 10^{-3} power-law breakdown occurs [71]. The value of the stress exponent for lithium tested in tension in this study is in excellent agreement with the stress exponent value of 6.4 for lithium at room temperature tested in compression by Sargent and Ashby [71], who suggested the creep of lithium is controlled by dislocation climb rate-limited by lattice diffusion.

Pressure		Aspect Ratio (H/D)	Minimum Secondary Creep	
σ (MPa)	σ/G		Rate (sec-1)	Strain (%)
0.200	7.13E-5	4.24	2.00E-7	0.25
0.301	1.07E-4	4.24	4.95E-6	0.51
0.396	1.42E-4	3.96	1.58E-5	0.36
0.400	1.42E-4	4.05	1.34E-5	0.20
0.400	1.42E-4	4.11	1.36E-5	0.26
0.400	1.42E-4	4.14	1.72E-5	0.37
0.600	2.13E-4	4.64	3.89E-4	5.67

Table 3.3: Tension Creep Minimum Secondary Creep Rate as a function of Pressure (room temperature)

The stress exponent for lithium can also be compared to the stress exponent for other alkali metals with the same structure (body-centered cubic) such as sodium and potassium [71]. The

stress exponent for potassium is equal to 6.4, in excellent agreement with that for lithium. The stress exponent for sodium is equal to 5.0, also in general agreement with that for lithium. The results of this study suggest that the creep of lithium, sodium and potassium is governed by same mechanism, diffusion-controlled dislocation climb. In order to test this idea it was decided to compare the creep rates of the alkali metals (lithium, sodium and potassium) at room temperature normalized with respect to lattice diffusion versus stress normalized with respect to the shear modulus [71]. The creep rate of the lithium, sodium and potassium must be normalized with respect to lattice diffusivity since lithium (T_m=453.5 K), sodium (T_m=371 K) and potassium (T_m=337 K) have different melting temperatures. The logarithm of the room temperature strain rate for lithium (this study) and lithium, sodium and potassium from Sargent and Ashby [71] normalized by the room temperature lattice diffusivity lithium ($D=3.1x10^{-1}$ cm^2/sec), sodium ($D=1.94x10^{-1}$ cm^2/sec) and potassium ($D=3.1x10^{-1}$ cm^2/sec) [71] is plotted as a function of logarithm stress normalized by the room temperature shear modulus of lithium (this study), sodium (G=1.53GPa) and potassium (G=0.661GPa) [71] in **Figure 3.8**.

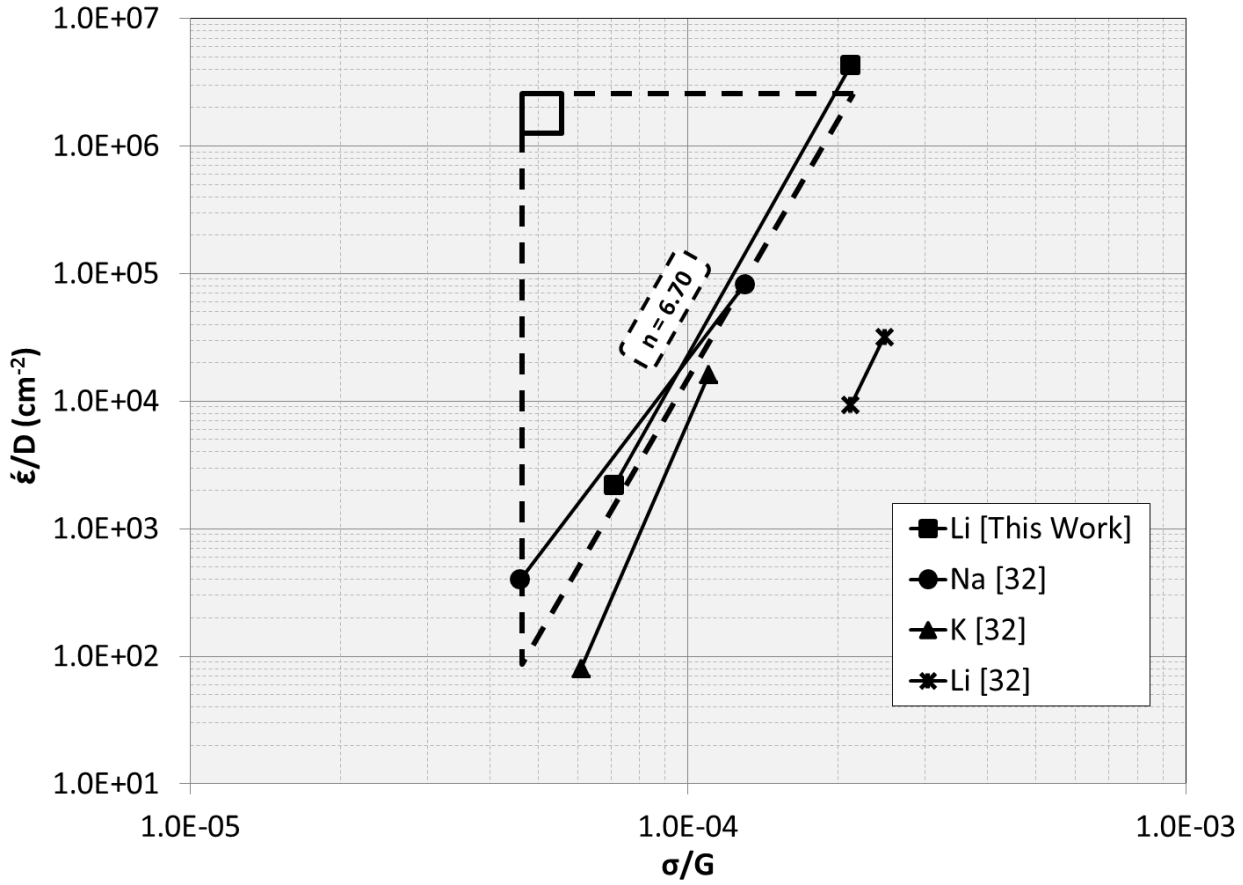

Figure 3.8: Room temperature strain-rate normalized by diffusivity vs stress normalized by shear modulus for various alkali metals [71] and lithium from this work [42].

From **Figure 3.8** several important points are noted. First, it is observed that the lithium data for this study and the data for potassium and sodium fall on nearly the same line. Second, the slope of this line is the stress exponent with a value of 6.70. These results confirm that the creep behavior of the alkali metals is controlled by dislocation climb rate-limited by lattice diffusion. Third, the creep data for lithium from Sargent and Ashby does not fall on the line with the rest of the data for the alkali metals. At a given strain rate lithium is about a factor of two times higher than the rest of the alkali metals. This is surprising since sodium, potassium and lithium were all tested by Sargent and Ashby [71] under compression loading. Reasons for this difference are not

apparent, however, Sargent and Ashby [71] state that the sample aspect ratio for the lithium samples was smaller than that for the potassium and sodium samples. It is known that as the aspect ratio decreases the load to produce the same reduction in height increases as discussed in more detail in the compression sections [71]. Thus, it is expected that the lithium samples with the lower aspect ratio will exhibit a higher strength than the potassium and sodium samples with a higher aspect ratio. This prediction is in agreement with results shown in **Figure 3.8**. Future studies should investigate the tensile creep of lithium at relevant automotive battery temperatures, e.g., -20 to 52°C; 0.56 to 0.71 T/T_m [27].

3.2.4 Time and stress dependent deformation vs load (compression)

Previously in this study, the stress-strain behavior of lithium was characterized in compression by varying the load (stress) and measuring the resulting strain. In this part of the study, the load in compression was kept constant and the strain-rate was measured. Based on our previous work [63, 105, 106] we believe LMSSB will require a constant compressive load to assure contact is maintained between lithium and the solid electrolyte during cycling. How much compressive stress is not known, but our previous solid-state cycling studies of lithium metal used a constant nominal compressive stress of 1 MPa [63, 105, 106]. We believe 1 MPa was sufficient to minimize the effect of pressure on cell impedance during cycling. Using 1 MPa as a relevant nominal value, this study characterized time dependent deformation at various constant stresses below and above 1 MPa (0.8 to 2.4 MPa; engineering stress). Strain-rate vs time and strain vs time plots are shown for an initial stress of 1.48 MPa (**Figure 3.9**).

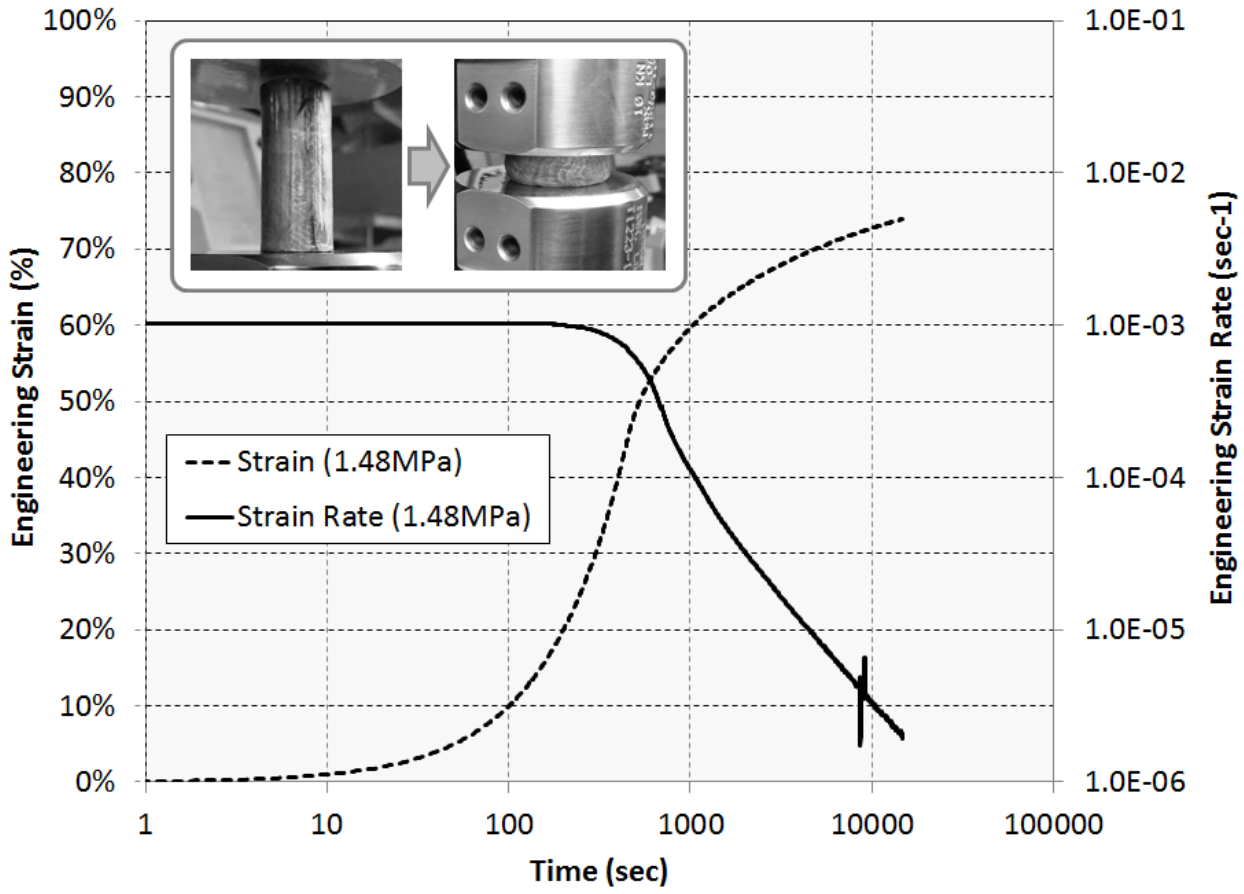

Figure 3.9: Room temperature engineering strain and strain-rate vs time and for lithium under compression.

Several distinctions can be made compared to tensile creep behavior. First, the shape of strain-rate vs time curve differs from a conventional tensile creep curve. In compression (**Figure 3.9**) the strain rate was initially held constant until the target compressive load was reached, once the target load is reached the strain-rate decreased with time. This behavior was observed for all samples held at constant compressive load. Conversely, in tension once the target load was reached the strain-rate was relatively constant, but eventually increased with time (**Figure 3.6**). In compression, barreling increased the sample area, thus decreasing the stress and therefore decreasing the strain-rate with time (**Figure 3.9**). In tension, necking decreased the sample area,

thus increasing the stress in the necked region and therefore increasing the strain-rate with time (**Figure 3.6**). Returning back to compression testing, it was also apparent that the strain-rate dramatically changed based on the time, and therefore degree of barreling, at which the strain rate was measured. For example, the strain-rate at 1000 sec was 10^{-4} sec^{-1} whereas at 10,000 sec the strain-rate was ~ in the 10^{-6} sec^{-1} range. The decrease in strain-rate was likely due to frictional forces and an increase in cross-sectional area, hence decreasing the stress.

Pressure		Aspect Ratio	Rate (sec-1)		
σ (MPa)	σ/G (10^{-4})	(H/D)	5C (720sec)	1C (3600sec)	0.5C (7200sec)
0.80	2.85	2.12	1.93x10-4	2.85x10-5	1.12x10-5
1.00	3.56	2.40	1.45x10-4	2.34x10-5	9.26x10-6
1.20	4.28	2.57	1.04x10-4	1.40x10-5	5.05x10-6
1.48	5.28	1.89	7.83x10-5	1.13x10-5	4.44x10-6
2.40	8.54	2.03	4.02x10-5	6.01x10-6	2.63x10-6

Table 3.4: Compression Creep Strain Rate as a function of Pressure and Time (room temperature)

A summary of the strain-rates vs initial stress are shown in Table 3.4 and plotted logarithmically in **Figure 3.10**. Because the strain-rate varies with time (**Figure 3.10**), the strain-rates estimated at various times are plotted as a function of the initial compressive stress. The times (12, 60, and 120 min) were selected to represent LMSSB charging or discharging times, i.e. the time a lithium electrode would be held during either a single charge or single discharge. It was observed that the higher the initial applied stress, the faster the strain-rate decreased for a given time. This would agree with the fact that the higher the load, the faster the lithium barrels, the

slower the strain rate at a fixed time. It was also observed that the greater the time, the slower the strain rate for a given fixed initial stress. This too would agree with the observation that the longer the time, the greater the degree of barreling, resulting in a slower strain-rate for a given fixed initial compressive load.

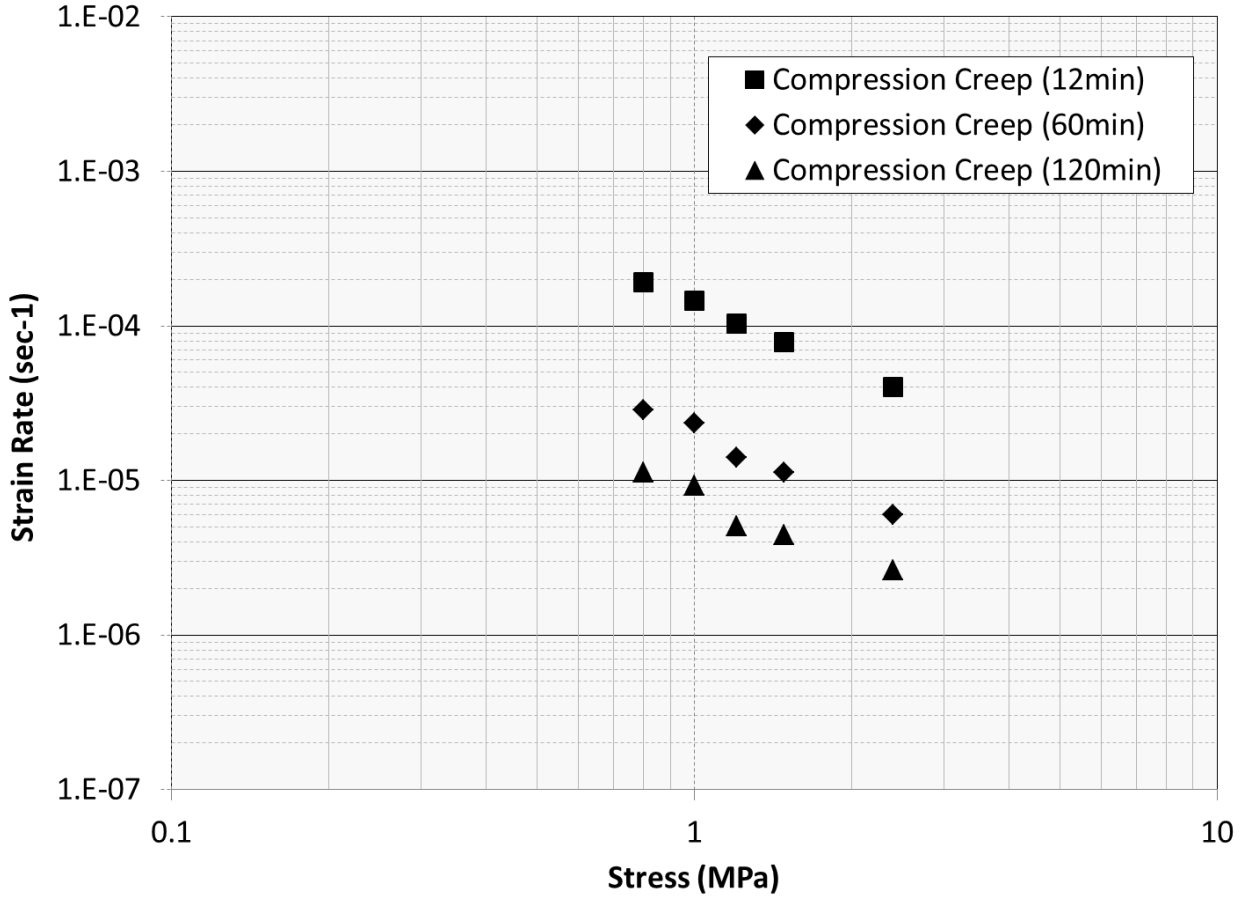

Figure 3.10: Room temperature strain-rate vs stress as a function of time. The three time points were taken to represent a LMSSB charged or discharged in 12, 60, and 120 minutes.

3.2.5 Implications to LMSSB

We believe this is the first comprehensive study of the elastic, plastic, and time-dependent mechanical properties of lithium. The intent was to characterize salient properties to help evaluate

the feasibility of LMSSB for a myriad of applications ranging from microelectronics, space, automotive, to grid technologies. The implications could be as follows.

First, this study analyzed the elastic properties using an acoustic technique to determine E, G, v and K. We also summarized and compared Young's modulus from literature and determined that the form, single vs polycrystalline, had an impact on the elastic properties of lithium.

Second, we analyzed the stress-strain behavior in tension and compression. Lithium is a highly ductile material that likely does not work harden. In compression, the highly ductile nature of lithium caused barreling that was a result of frictional forces between the platen and lithium sample face an increase in cross-sectional area. These elastic and plastic mechanical property constants will be important in analyzing the mechanical stability of the lithium-solid electrolyte interface. We believe LMSSB will cycle polycrystalline lithium, thus the polycrystalline properties may be more relevant, or at least for analysis of the deformation of lithium at the macroscopic scale. In addition, the unusual behavior observed in compression stress-strain analysis helped to elucidate the time-dependent compression deformation behavior.

Third, the creep behavior was measured in tension. The behavior was more-or-less conventional where the strain rate increased with time due to contraction in cross-sectional area and eventual necking. It was from the tensile creep tests that constitutive equations were used to determine that lithium deformation was governed by power-law creep (dislocation climb) when a stress relevant to LMSSB was applied (~ 1 MPa). The creep mechanism determined in this study for alkali metals should help guide analysis not only of lithium deformation during LMSSB cycling, but perhaps in the use of other alkali metals such as; sodium and potassium as anodes.

Fourth, we believe the time and stress dependent deformation vs load (in compression) analysis most closely mimics LMSSB operation. Based on our experience in cycling lithium metal

electrodes paired with solid-electrolytes, we used relevant compressive loads to study time-dependent deformation of lithium (~1 MPa).

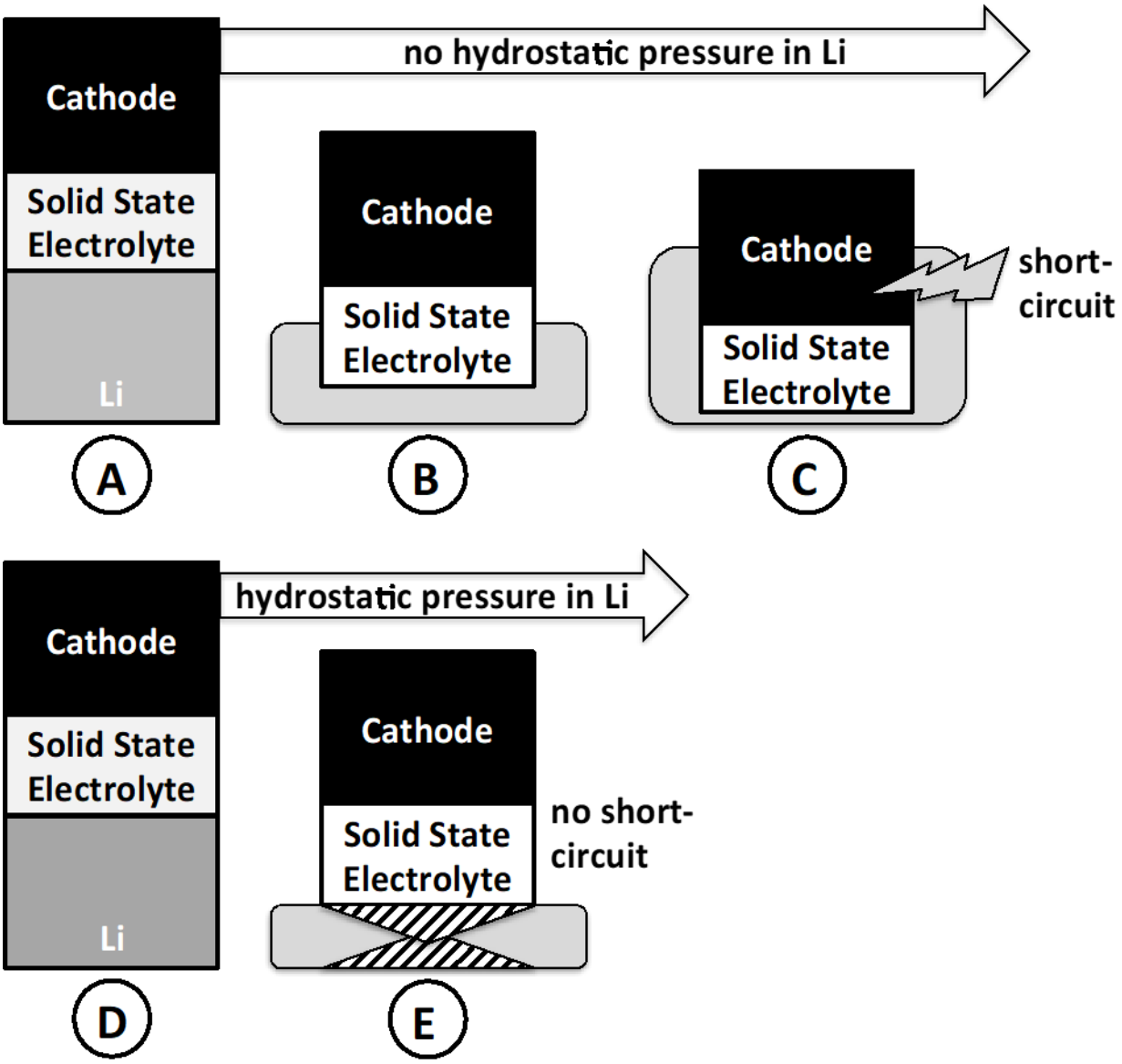

Figure 3.11: Under compression; two possible scenarios determined by the deformation behavior of lithium: (A-C) with no adhesion between components, lithium could deform to eventually short-circuit against the cathode; (D-E) if lithium adheres to the solid-electrolyte and current collector, frictional forces.

Further possible implications for LMSSB performance are illustrated in **Figure 3.11**. If lithium freely flows without hydrostatic stress caused by friction, the cathode/solid-electrolyte could cause lithium to flow and eventually short-circuit with the cathode (**Figure 3.11A-C**). If the compression (constant strain rate and time dependent) observations made in this material study also occur in a LMSSB, which we believe is likely, frictional forces between lithium and the current collector and lithium and the solid-electrolyte will create hydrostatic stresses that impede deformation. These hydrostatic stress zones would prevent lithium flow and short-circuiting (**Figure 3.11D-E**). Both the magnitude of the initial stress and the time (as shown in **Figure 3.10**) will likely affect scenarios in **Figure 3.11**. The lithium anode aspect ratio and frictional forces will have significant effects on the cycling of lithium under compressive stresses.

3.3 Conclusions

The high specific and gravimetric capacities of lithium are attractive features for an anode; however, it is difficult to assess the feasibility of LMSSB without understanding the mechanical behavior of lithium. Thus, the goal of this study was to establish a database of elastic, plastic, and time-dependent properties of lithium. The bulk, elastic, plastic, and time-dependent mechanical properties of polycrystalline lithium were measured at room temperature. Elastic properties were measured using an acoustic technique (pulse-echo). The Young's modulus, shear modulus, and Poisson's ratio were determined to be 7.82 GPa, 2.83 GPa, and 0.381 respectively. The stress-strain behavior of lithium in tension and compression was characterized using a unique load frame housed in an inert atmosphere. The yield strength was in the range between 0.73-0.81 MPa. The time dependent deformation in tension was dramatically different compared to compression. In tension power law creep dominated with a stress exponent of 6.56, suggesting dislocation climb

as the rate-controlling mechanism. Furthermore, it was shown that the creep behavior of other alkali metals with a body-centered structure is also controlled by dislocation climb. In compression, time-dependent deformation was characterized over a range of stress believed to be germane to LMSSB (0.8 to 2.4 MPa). At all compressive stresses, significant barreling and a decrease in strain rate with increasing time were observed. We believe the time-dependent properties characterized in compression closely resemble the stress environment that mimics the stresses during LMSSB operation. Thus, the effects of sample aspect ratio and friction (or adhesive forces) should be considered, in the design of LMSSB, to determine how much lithium deforms during operation. The data and analysis in this study will help future studies and guide the development of LMSSB.

3.4 Acknowledgements

Funding support from the Ford-University Michigan Alliance program (Grant # UM0163) is acknowledged. Thanks are given to James Boileau and Kent Snyder for helpful conversations. Jeff Wolfenstine would like to acknowledge support of the Army Research Laboratory.

Chapter 4

Characterizing the Mechanical Behavior of Lithium in Compression

This chapter describes the lithium metal solid state battery (LMSSB) specific sensitives of lithium metal's mechanical properties, including bulk lithium's response to changes in AR, temperature and SR, as well as foil lithium to low AR and the resulting theory of hydrostatic pinning [98].

4.1 Introduction

Batteries are central to personal electronics and the burgeoning growth of electric vehicles. Though significant progress has been made in improving the performance of Li-ion batteries, a step increase in performance, lower cost, and improved safety are required [29]. Solid-state batteries or batteries using solid electrolytes and lithium metal comprise a growing field of battery research. By replacing the standard carbon graphite anode with lithium metal, a roughly 50% gain in cell energy is possible [35, 36]. However, to be useful in the transportation market a LMSSB would have to meet long-life requirements such as 15 years calendar life and 1,000 cycles [27].

Recently it has been shown that despite a dramatically lower elastic modulus in the bulk form (i.e. elastic modulus E = 7.8 GPa by mechanical load frame [42], 8.2-9.8 GPa by nano-indentation [117], 11.1 GPa by DFT modeling [63]), lithium is able to penetrate relatively stiff solid-state electrolytes such as LLZO ($E \approx 150$ GPa) and LPS ($E \approx 13$ GPa) [42, 118, 119]. When lithium penetrates a solid electrolyte, short-circuiting occurs thereby causing an abrupt drop in voltage. Thus, knowing how and why lithium penetrates solid electrolytes is important to

eventually enable the development of viable LMSSB. How this is possible is still not clearly understood, despite intense research. For example, our recent work characterized the elastic, plastic and creep properties of bulk-scale lithium specimens in tension and compression [42]. In related work by other groups, it has been shown that the yield strength of lithium may significantly increase with decreasing size domains such as in micro and nano-pillars [116, 120] and in thin films [121] using nano-indentation. The increased strength of lithium at micro-size scales could help explain how relatively soft lithium is able to penetrate hard ceramics in actual Li/SSE cells. Similarly, it has been shown that yield strength or flow stress increases with increasing strain rate in both compression [61] and tension [62, 122]. In addition, it is generally known that the yield or flow stress decreases with increasing temperature, a trend seen in our work in compression and by others in tension [62, 122].

While the intent of these and other recent studies focused on understanding the fundamental properties of lithium metal, we believe that the mechanical behavior can be dramatically changed by several external variables imposed by the intended application. First, to mitigate polarization during discharge due to depletion [123, 124, 125, 126], LMSSB will require compressive stress. As a result, we would expect the interfacial dynamics to be controlled by the behavior seen in compression rather than tension testing [42]. As was previously described by Masias et al., lithium is hypothesized to show hydrostatic pinning in its bulk region owing to surface adhesion effects at its interface with both the solid-state separator and the anode current collector, battery case wall or whatever other structure is designed to maintain the compressive stress required [42]. Second, commercial LMSSB will use lithium electrodes that are < 50 μm thick. This dramatically changes the aspect ratio compared to recent studies (done at aspect ratio 2 or greater) and will amplify interfacial effects between current collector foil and the solid electrolyte. Third, it has been shown

that strain rate affects lithium mechanical behavior; however, the simultaneous impact of decreasing aspect ratio and compressive strain rate is not well understood. Fourth, it is known that temperature affects mechanical properties, but the combined effects of low aspect ratio and compressive loading are not known at this time. It follows, that the purpose of this work was to study the mechanical behavior of lithium in compression as a function of aspect ratio, strain rate, and temperature. The effective compression flow stress at room temperature was found to increase with decreasing aspect ratio (1.86 MPa at AR 0.045 and strain rate of $1x10^{-3}$) and increasing strain rate (1.39 MPa at 1.0 s^{-1} strain rate and aspect ratio of 2). The impact of geometric size (aspect ratio) and strain rate were shown to be cumulative with a peak effective elastic/plastic transition flow stress of 1.91 MPa at AR 0.23 and 1.0 s^{-1} strain rate at room temperature. Additionally, as temperature increased, the effective elastic/plastic transition flow stress significantly decreased (i.e. 0.21 MPa at 132 °C, T_H = 0.90 and base strain rate and aspect ratio) across all aspect ratios. We believe the measurements, correlations, and observations in this study can inform the development, design and manufacturing of LMSSB.

4.2 Results & Discussion

The mechanical behavior of lithium rods were characterized in compression as a function of sample aspect ratio, strain rate and temperature. Additional compression experiments were performed with lithium foils of varying geometry at constant temperatures and strain rates. Initially the effect of each variable is discussed individually, followed by a study of the combined multifactor effects.

4.2.1 Lithium rods and aspect ratio

The stress-strain behavior of lithium was analyzed in compression using cylinders with aspect ratios (height/diameter) ranging between 0.28 and 2.10. A representative stress-strain curve

is shown (**Figure 4.1**) for a sample tested at AR 2.10, $1x10^{-3}$ s^{-1} strain rate and 26°C. In general, two distinct stress-strain regions were observed. In Region I at low strains (< 4.31% on average for N = 81, where N = is the number of experiments performed), all specimens exhibited a relatively steep slope, ostensibly, appearing as the elastic modulus (*E*) in a typical stress-strain curve. However, the slope of the linear part of the stress-strain curve in Region I is not comparable to the typical *E* value for lithium (7.82 GPa) [42] measured using an acoustic technique. As previously observed by Masias et al., the slope of the line in Region I is not likely E, because at 26°C the homologous temperature of lithium is 0.66. Instead, we believe significant plastic deformation occurs even at low strains, thereby changing the interpretation of the linear portion in Region I. Similar behavior was observed by Cook et al. who studied the compression behavior of copper [99]. At low strains, a linear region appeared to resemble *E*, however the slope was 62 times lower (1.9 GPa) than what is expected for the Young's modulus of copper (117 GPa). In this study, the slopes of the curves in Region I were nominally 212 times lower (average 36.9 MPa) than what was expected (7.82 GPa) for lithium at room temperature. We believe the linear behavior at low strains, whether it is in lithium or copper, could be an artifact of analyzing metals that exhibit significant ductile behavior.

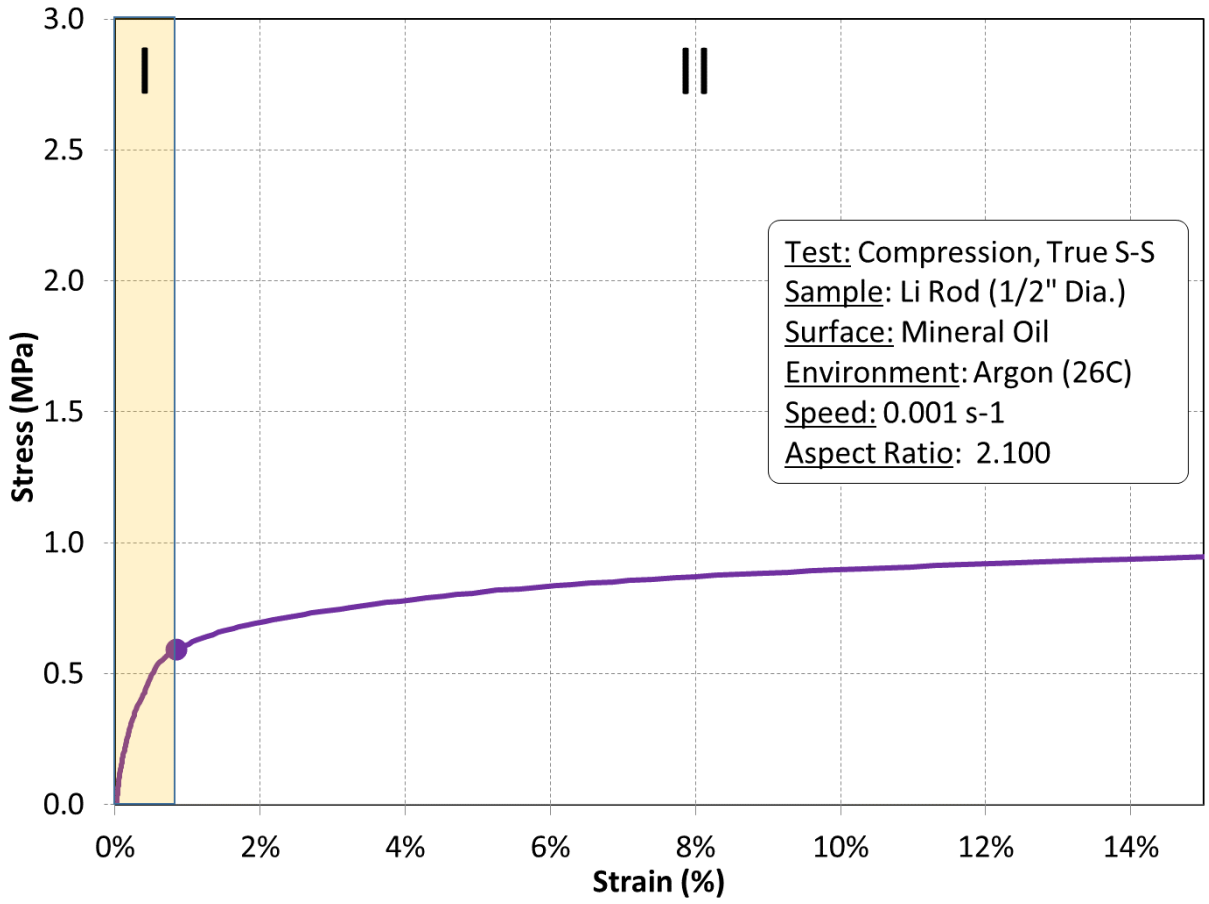

Figure 4.1: Representative stress strain curve of lithium in compression showing region I and II (0.66 T_H, 1 x10^{-3} s^{-1}, AR 2.10)

As the stress and strain increased into Region II, the behavior changed and was strongly affected by the aspect ratio (**Figure 4.2**). First, as the aspect ratio decreased, the stress at which the behavior transitioned from Region I to Region II increased. Because the slope in Region I is not *E*, we do not believe it is appropriate to refer to the stress at which the behavior transitions from Region I to Region II as the yield stress. Due to the significant plastic deformation in these tests, we believe it is more appropriate to refer to the stress that delineates Region I from Region II as the flow stress (σ_{flow}). Flow stress is typically the stress required to sustain plastic deformation over large degrees of deformation with negligible work hardening. The extent to which the aspect

ratio, and therefore we believe the frictional forces, affect the flow stress is shown in **Figure 4.2**. Similar behavior was observed in compression tests of copper as a function of aspect ratio [99]. Secondly, the slopes in region 2 increased with decreasing aspect ratio. For example, the slopes in Region 2 for aspect ratios of 2.0, 0.5 and 0.25 were 2.49, 3.41 and 6.80 MPa between the Region I/II transition and 15% strain, respectively. Again, the same behavior was observed for copper in compression tests [99]. Ostensibly, what could be interpreted as work hardening, where the stress increases with increasing strain in Region II, is instead a manifestation of frictional effects between the platens and lithium. As we showed previously [42], lithium does not work harden at room temperature and modest strain rates. Thus, the increase in stress with increasing strain in Region II likely results from non-uniform sample deformation "barreling," which is due to frictional forces between the load frame platens and the lithium cylinders. As we previously described, frictional forces created hydrostatic stress at the platen-lithium interface, thus increasing the stress required to cause plastic flow [42].

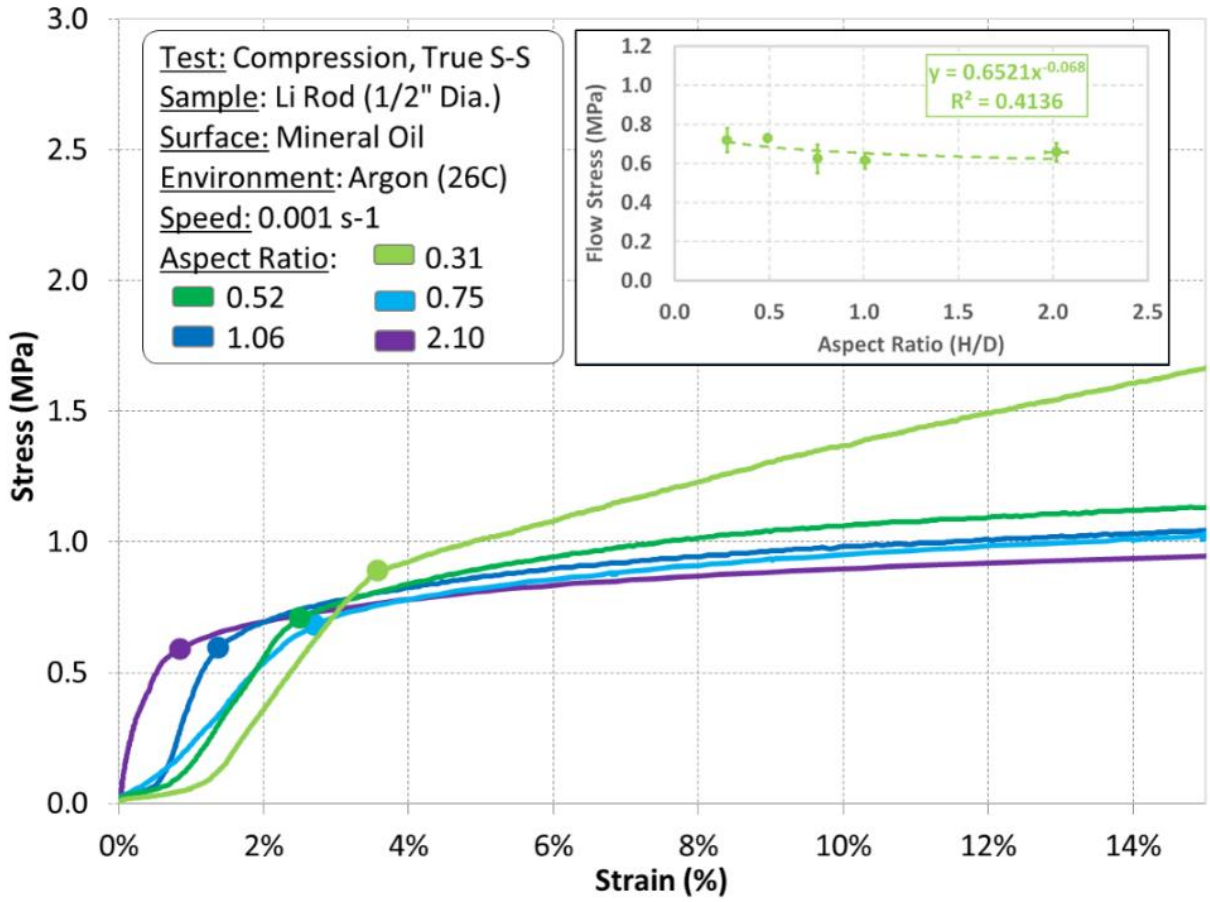

Figure 4.2: Stress-stain behavior of lithium metal cylinders of various aspect ratios (compression). The scatter points on the inset plot represent the average of all 25 individual tests under their corresponding settings, while the error bars represent the standard deviation.

The flow stress for 2.0 and 0.25 aspect ratios were 605 and 834 kPa, respectively. Two external references are in good agreement with the values measured in this work as a function of aspect ratio and strain rate [42, 126]. The individual flow stress values (plotted as an average in the inset) measured at 0.66 T_H and $1x10^{-3}$ s^{-1} strain rate are shown as a function of aspect ratio in **Figure 4.2**. It can be seen that varying solely aspect ratio in the band of this work has a mild effect on flow stress, however it will be shown later that simultaneously varying temperature or strain rate at the same time as aspect ratio has a more pronounced effect.

4.2.2 Lithium rods and temperature

Raising the temperature had a significant effect on the resulting stress-strain behavior in compression. Compression stress strain behavior was characterized at 26, 73, and 134 ˚C using a strain rate of $1x10^{-3}$ s^{-1} and varying aspect ratio (**Figure 4.3**). As expected and previously shown, increasing the temperature lowers the flow stress **(Figure 4.3**, representative data for AR=2). This response as a function of temperature is well known and inverse to that seen in materials for increasing strain rate [43]. Unlike at the characterization conducted at fixed temperature (26 ℃) described in **Figure 4.2**, the effect of aspect ratio was more pronounced as the temperature increased (**Figure 4.3** inset). For example, at 26 °C the flow stress was 656 kPa and 718 kPa for AR of 2.02 and 0.28, respectively. However, at 134 °C, the flow stress was 225 kPa and 367 kPa for AR of 2.03 and 0.28, respectively. Thus, the increase in flow stress with decreasing AR was 63% higher at 134 °C compared to only 9% at 26 °C. The reason for this will be discussed in the multifactor analysis below.

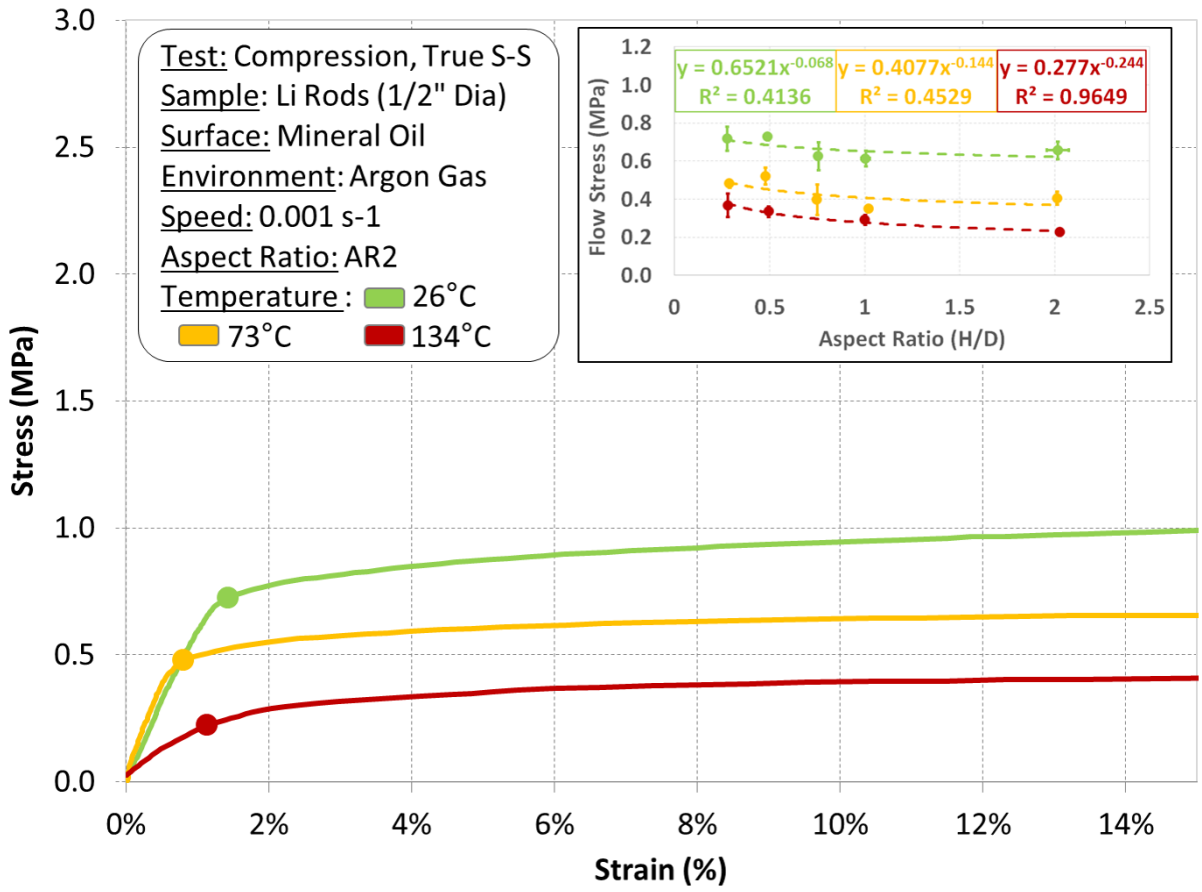

Figure 4.3: Stress Strain as a function of temperature & aspect ratio ($1x10^{-3}$ s^{-1}). The scatter points on the inset plot represent the average of all 50 individual tests under their corresponding settings, while the error bars represent the standard deviation.

The stress-strain temperature relation is most often described by the Zener-Hollomon parameter where the strain rate is correlated with temperature according to Arrhenius behavior [127, 128]. For this series of experiments, either the strain rate or temperature was varied, but not simultaneously, so a determination of the Zener-Hollomon parameter or activation energy is not possible, but would make for an interesting future study. [43, 127, 128].

The strain hardening behavior of a material can be approximated by Holloman's equation, $\sigma = K\varepsilon^n$, where n is the strain hardening exponent (SHE) and K the strength coefficient when temperature and strain rate are held constant [129]. The SHE is an expression of the dislocation

quantity and motion arising in a material due to plastic flow. As a result, the SHE can be thought of as a measure of the balance of work hardening (i.e. dislocation generation and pile up) and dynamic softening (i.e. new grain growth or dislocation annihilation) during plastic flow [130]. This reflects the equilibrium due to the formation of new grains and the corresponding grain boundary motion.

As the temperature is raised, more energy is provided for dislocation movement to promote recovery and/or recrystallization. As a result, strain hardening rates are known to generally decrease in most metals with increasing temperature, as the additional thermal energy boosts dynamic softening, however this was not observed consistently in lithium (see **Figure 4.4**) [43]. An analysis of the SHE of lithium as temperature was performed for a range of aspect ratios to investigate the contribution of size effects and related friction changes. As can be seen in **Figure 4.4**, for AR2.02 and AR1.01 there is a subtle increase and for AR0.76, AR 0.49 and AR0.28 a subtle decrease in the SHE as a function of temperature. In the case of lithium across the temperature changes we measured, this dynamic softening was not significantly greater than the work hardening occurring resulting in a mostly level strain hardening exponent, n (see **Figure 4.4**).

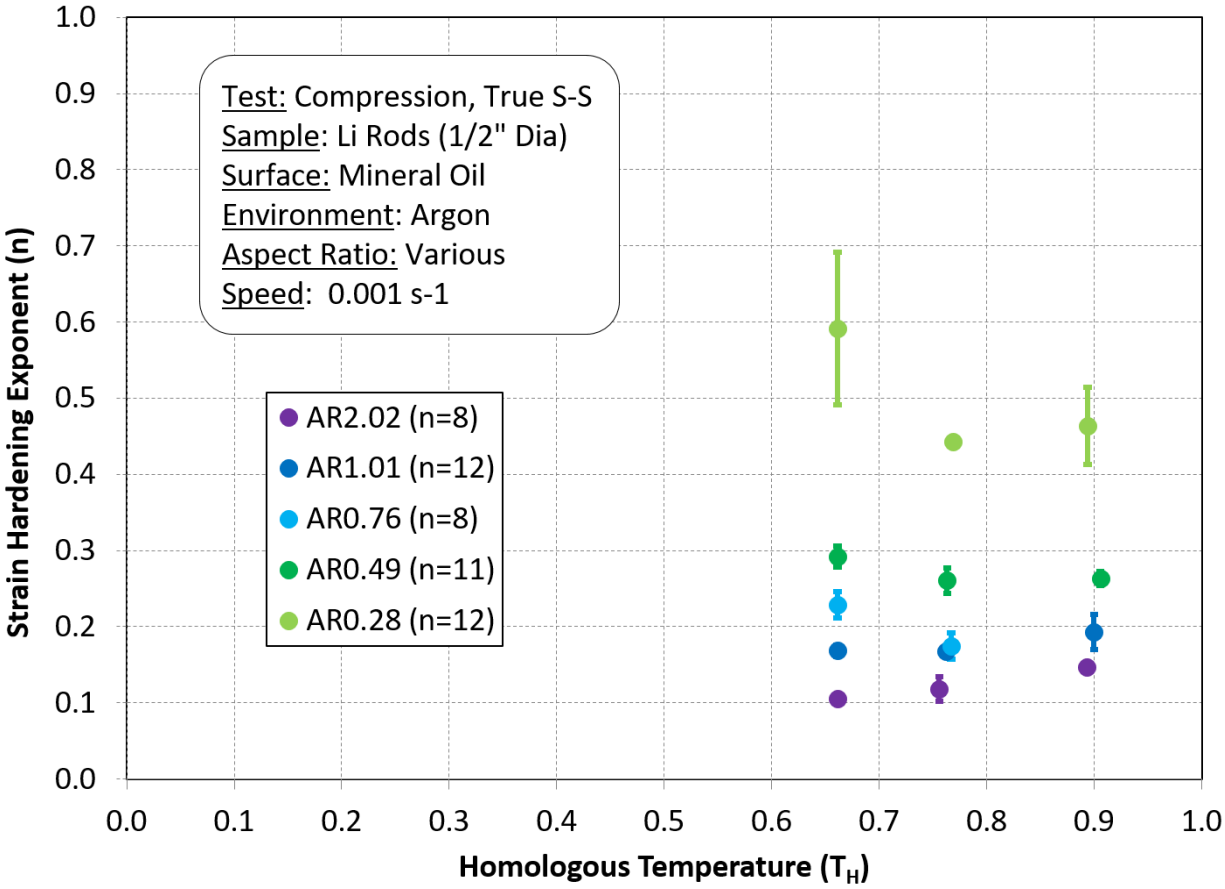

Figure 4.4: Strain Hardening Exponent as a function of temperature

The trend seen in increasing flow stress as a function of decreasing temperature is also seen in tension. Despite the different testing sample preparations and measuring methods, there is generally broad agreement (**Figure 4.5**). As the temperature increases, the flow stress, whether measured in compression or tension, decreases with increasing temperature [62, 114, 122].

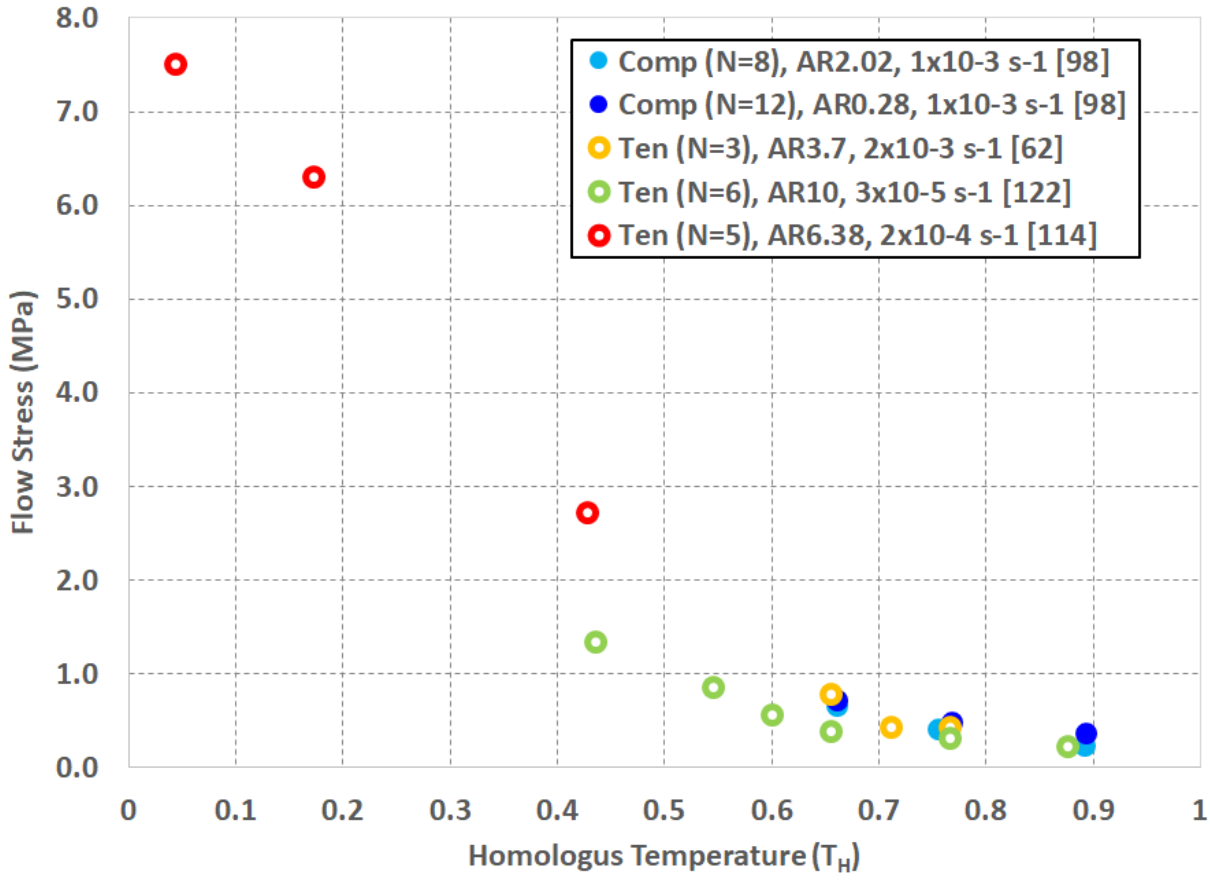

Figure 4.5: Lithium Flow Stress as a function of Homologous Temperature [62, 98, 114, 122]

4.2.3 Lithium rods and strain rate

The strain rate was also shown to have an effect on the stress-strain behavior of lithium in compression, (see **Figure 4.6**). As can be seen in **Figure 4.6**, increasing the strain rate to 3.16 $x10^{-2}$ s^{-1} has a similar impact on the strain curve as slowly (1 $x10^{-3}$ s^{-1}) testing a sample with a low aspect ratio (AR0.28), see **Figure 4.3**. As the strain rate is increased further to 1 s^{-1}, the resulting curve rises to the onset of flow stress and then continues with a similar slope thereafter, with the ratio of before and after slopes also approaching unity as a function of increasing strain rate (**Figure 4.6**).

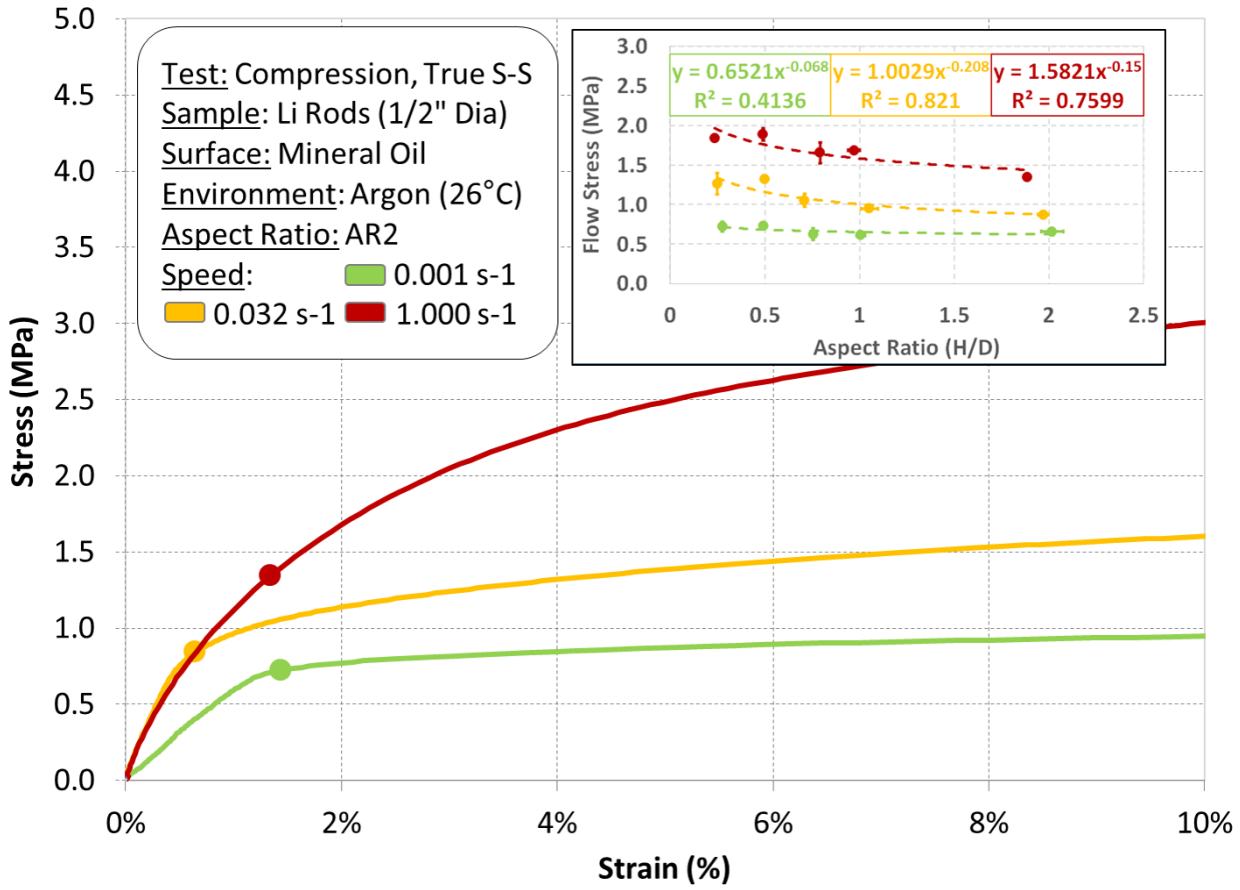

Figure 4.6: Stress Strain behavior of lithium in compression as a function of strain rate & aspect ratio (0.66 T_H). The scatter points on the inset plot represent the average of all 55 individual tests under their corresponding settings, while the error bars represent the standard deviation.

The trend of increasing yield strength as strain rate is broadly similar to that shown by LePage et al., Fincher et al. and others [61, 62, 122, 131] but differs in several key respects, likely related to the range of strain rates and test methods used. First, as the strain rate (s^{-1}) increased from 10^{-3} to 10^{-2} to 10^{1}, the distinction between elastic and plastic strain diminished. For example, at a strain rate of 10^{1} the stress-strain curve appears as a continuous arc. Second, the testing performed in this study was conducted in compression using lithium rods of AR $\leq$ 2, while other

studies used higher aspect ratios or were done in tension (LePage et al) to quantify stress-strain behavior. Despite the differences in method and sample shapes, the broad trend between strain rate and flow stress is consistent across various studies, see **Figure 4.7.**

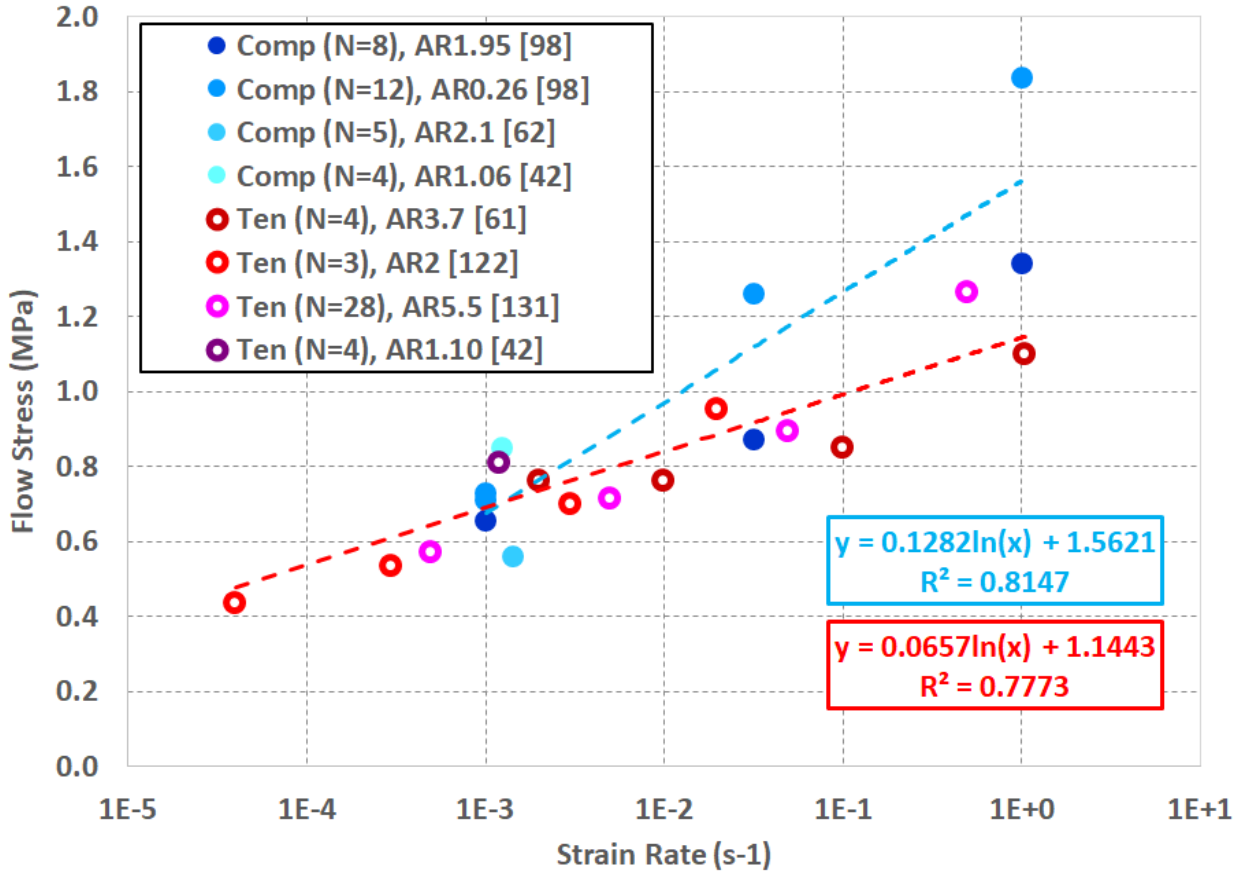

Figure 4.7: Lithium Flow Stress as a function of Strain Rate at Room Temperature [42, 61, 62, 98, 122, 131]

Previously, compression deformation testing determined the onset of creep at room temperature in the range of $1x10^{-4}$ s^{-1} [42], so the ASTM standard (1 x 10-3 s^{-1}) was chosen as the strain rate minimum [95]. If a strain rate at or below the secondary creep steady state rate is chosen, then lithium will behave as a viscoelastic material rather than plastically given that it has sufficient

time to deform via creep mechanisms. The maximum rate of 1.56 s^{-1} was calculated as the practical test machine limited upper boundary for the sample sizes of interest given speed limit of 2500 mm/min. After considering load cell safety limits, a strain rate of 1 s^{-1} was chosen as the strain rate ceiling for these experiments.

The impact of strain rate on stress agrees with the behavior seen in other metals [132]. Due to the rather low melting point of lithium metal (180.5°C), the room temperature evaluation corresponded to a homologous temperature of 0.66, well above the 0.50 value commonly marked as the recrystallization temperature, often considered as the beginning of hot working [44]. Flow stresses of 656 kPa, 871 kPa and 1,343 kPa were measured for the largest samples (N=8, AR1.95) measured at 1 x10^{-3} s^{-1}, 3.16 x10^{-2} s^{-1} and 1 s^{-1}, respectively. The smallest samples (N=12, AR0.26) experienced flow at stresses of 718 kPa, 1,260 kPa and 1,838 kPa at the same strain rates. As can be seen in these results and in **Figure 4.6**, increasing the strain rate of testing significantly influenced the resulting flow stress.

The impact of strain rate on the SHE was also measured (see **Figure 4.8**). As the strain rate increases, the time for dynamic softening is progressively shorter, often leading to the strain hardening term being dominated by the work hardening contribution. It is unclear if this is the dominant hardening mechanism in lithium. However, this general trend in other materials was not observed in lithium, as the SHE increased as function of strain rate across all aspect ratios measured, with a factor of 4 increase for the case of AR1.95 for the strain speeds measured. This result could suggest that the diffusional flow of dislocations in lithium maybe relatively slow at the absolute strains and timescales measured compared to other materials such as steel [43]. It should be noted that our values for strain hardening were all calculated at hot working temperatures, defined as above the recrystallization temperature, estimated at $T_H > 0.5$ for pure

metals [44]. Although other metals such as aluminum exhibit decreasing SHE as temperature rises, most of this decline occurs under cold-working temperatures (defined as $T_H < 0.5$) and only reaches a low level plateau in the hot working temperature zone [43]. As a result, it is likely that in the cold working temperatures range, lithium would exhibit higher SHE.

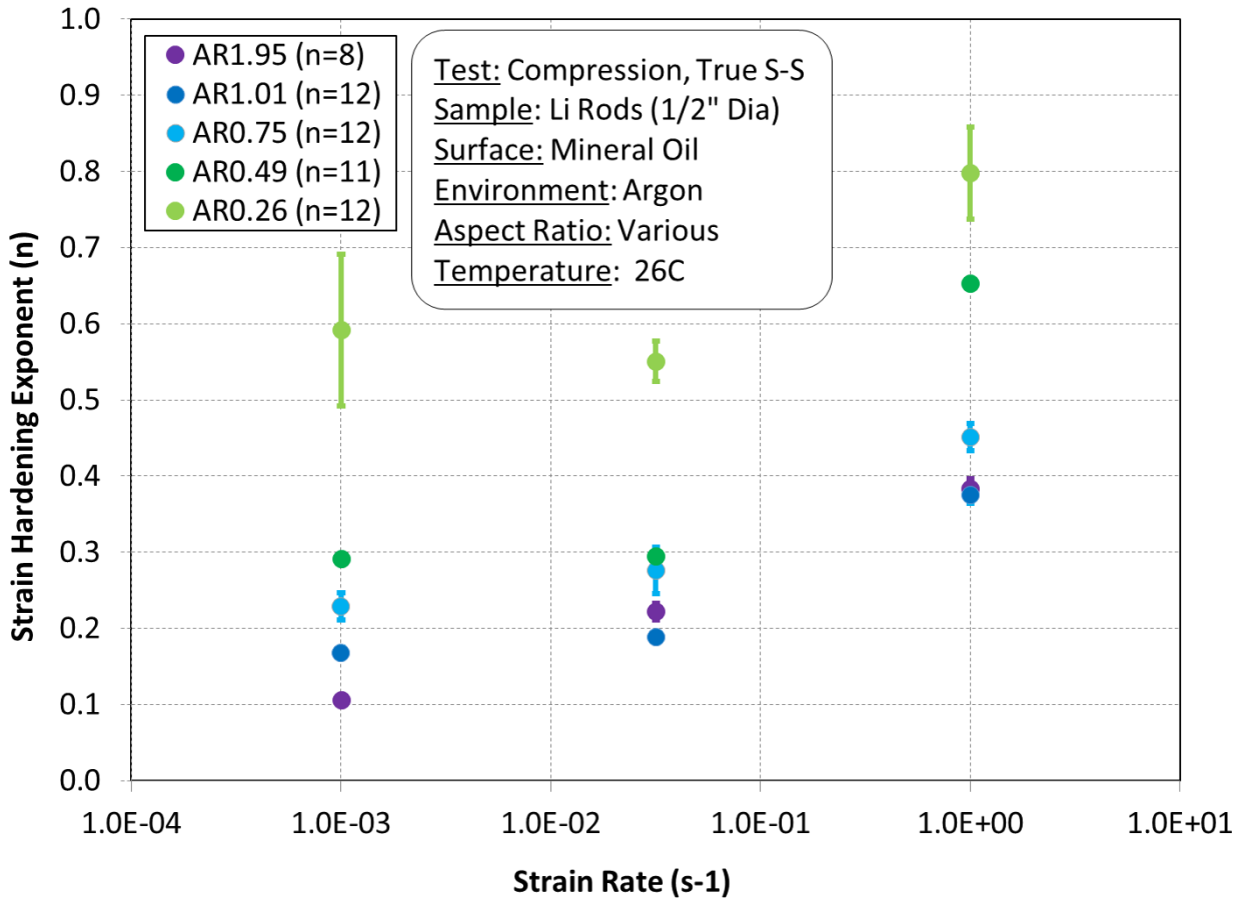

Figure 4.8: Strain Hardening Exponent as function of strain rate

A further review of the stress strain curves with increasing temperature and strain rate shows a continuously increasing stress, i.e. an absence of a stress peak. Stress peaks can be suggestive of a dynamic softening dominated by recrystallization as this process involves the creation of new, softened grains. The lack of a stress peak with increasing temperature or strain

rate suggests the greater influence of dynamic recovery or dislocation annihilation [130, 133]. A dynamic plot of the strain rate sensitivity exponent compared amongst three different strain rates is shown in **Figure 4.9**. Due to data collection scheme employed, each data series had a different time and strain basis, as a result a linear interpolation of the two nearest points between 0.5% strain intervals for each data series was first determined. Once the locally interpolated stress was found for exactly equivalent values of strain, this was used in concert with the well-known power law expression relating flow stress to strain rate, $\sigma = C\dot{\varepsilon}^m$, where m = strain rate sensitivity exponent (SRSE) [132]. This analysis was performed from the first 0.5% strain interval following yielding (1.5%) until 15% and then from 15% to 30% at every 1.0% strain interval as the behavior was well behaved. The SRSE ranged from m = 0.076 – 0.181 considering all the values measured, however when comparing the three values of m at specific strain points, the range was much smaller, for example m = 0.076-0.110 at 1.5% and m = 0.156-0.179 at 11% strain respectively. From 11% strain forward, the 1 s^{-1} strain rate test condition reached our equipment load limit (500N), terminating the test and leaving only 2 strain rates to be compared between 11% and 30% strains, also shown in **Figure 4.9**. Here we can also see that the SRSE appears to hit a plateau of 0.177 at 30%. The collected data through 11% for the other two calculated values of strain rate exponent also implies that those data sets would have likely reached a similar plateau. The reduced range of strain rate sensitivity, m = 0.156-0.179, occurring at T_H = 0.66 of lithium aligns well with metals such as copper and titanium seen by Boulger [134] and reported by Hosford [43]. The SRSE is expected to be insensitive to stress in BCC metals, and this insensitivity was seen after ~5% strain was achieved as is evidenced by the plateaus seen in **Figure 4.9** [132, 134]. During the analysis of dynamic strain rate sensitivity it is possible for friction effects to lead to increased stress and therefore contribute to the changing strain rate sensitivity.

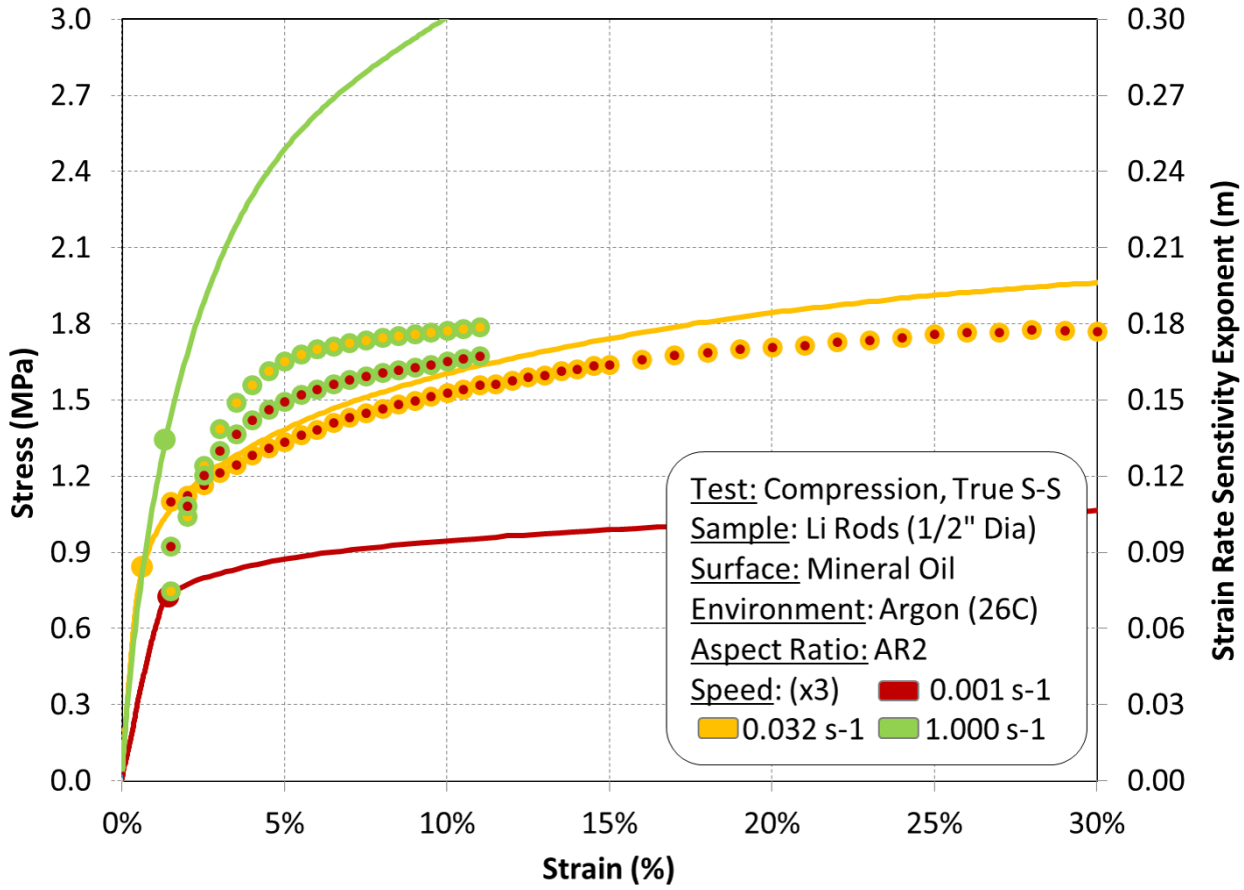

Figure 4.9: ***Strain Rate Sensitivity Exponent as function of strain rate***

4.2.4 Lithium foils

The 81 lithium rod experiments shown in sections 2.1-2.3 were performed using 12.7mm diameter samples of various heights. To further explore the impact of decreasing aspect ratio, an additional twelve experiments were performed using lithium foil of three diameters (8, 12.7 and 14 mm) but equivalent height (0.75 mm) see **Figure 4.10**. An additional, six foils were roll pressed to achieve a smaller height and two of these were then annealed to control for the

introduction of microstructure change during pressing. These six samples were cut to a diameter of 9.5 mm and are all shown in **Figure 4.10**.

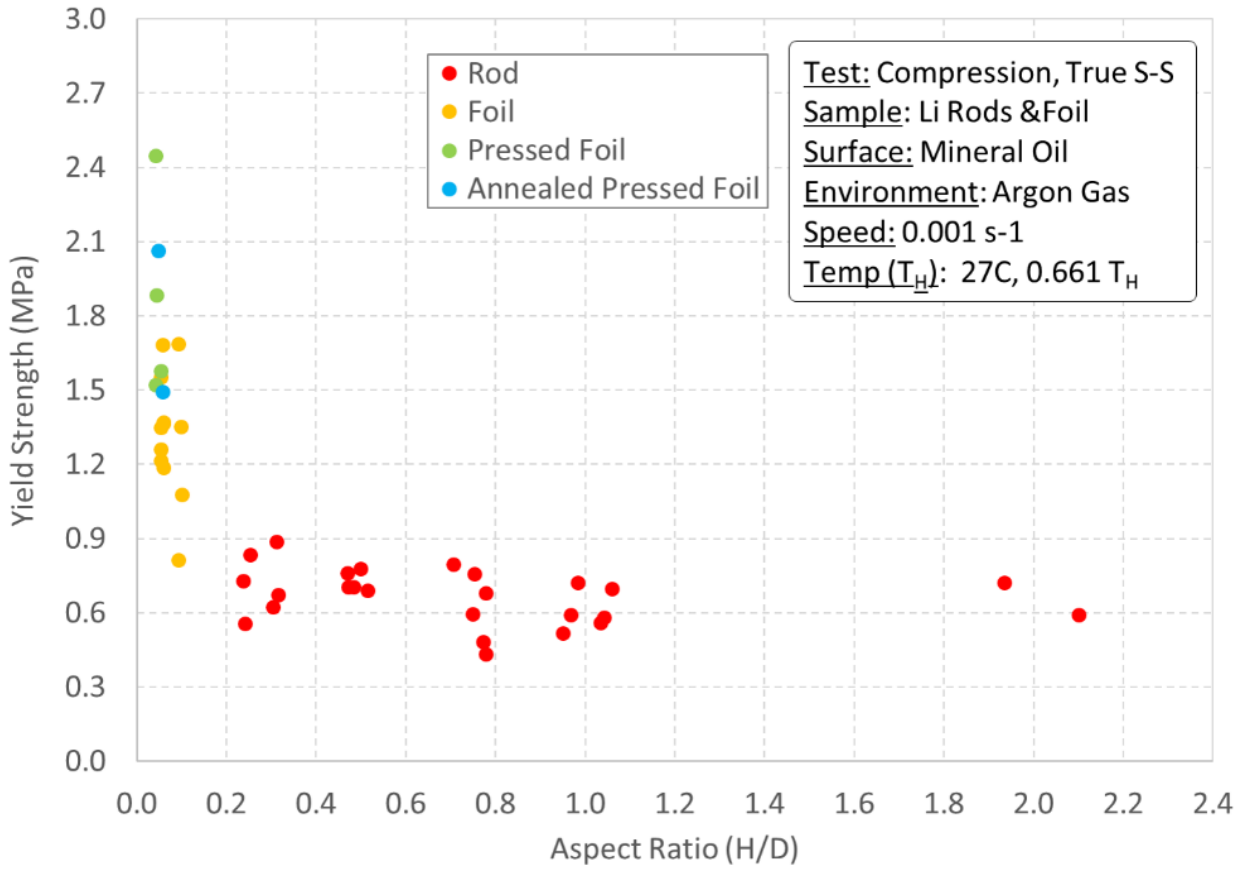

Figure 4.10: Yield Strength as a function of aspect ratio for lithium foil and rods

With the introduction of lithium foils, aspect ratios between 0.045 and 0.095 were achievable, significantly lower than the 0.24 aspect ratio that seemed to be the practical limit of the lithium rod based technique. The yield strengths measured at these lower ARs were significantly higher (AR0.045, N=4 yielded at 1.86 ± 0.21 MPa) and consistent with the trend lines established at larger ARs (see **Figure 4.11** and inset). Additional testing using annealed samples

yielded similar results (AR0.53, N=2 yielded at 1.78 ± 0.20 MPa) confirmed that our rolling process did not impart a microstructure change.

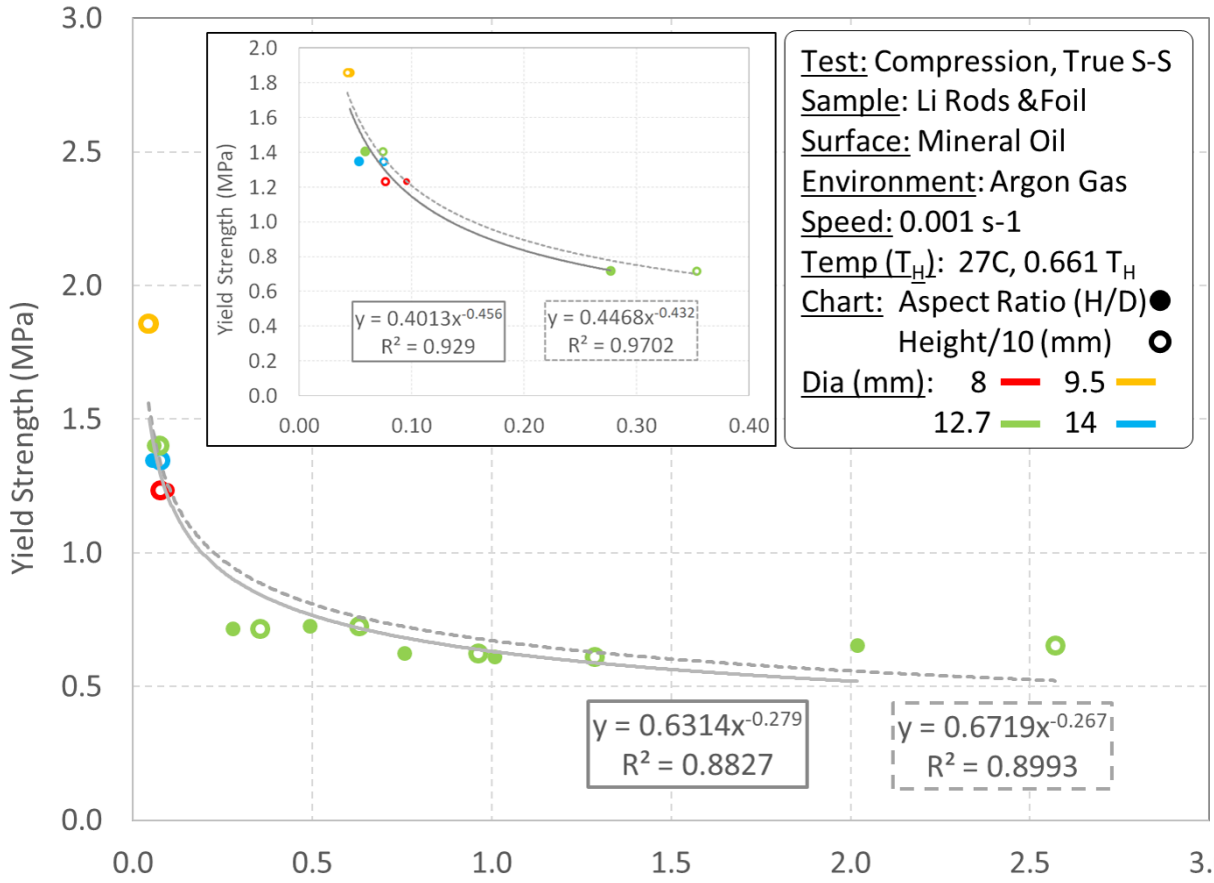

Figure 4.11: Yield Strength as function of aspect ratio and height across lithium rods and foil dimensional groups

In a battery, the AR of actual use is likely to be orders of magnitude smaller than that of the typical compression AR2 [95] and tension AR4 [96] performed during bulk mechanical testing. Our research effort is an attempt to bridge the bulk AR2 compression standards with decreasing ARs that move towards more battery device relevant dimensions. Based on existing lithium ion battery engineering principles we can estimate the likely ARs of future lithium metal based solid

state batteries [42]. For example, an electrode areal capacity of 4 mAh/cm^2 with a 50% excess lithium (to account for loss over time) would require a lithium thickness of only 30 um. Extending this electrode areal capacity target to approach battery capacity values commonly used in smart phones, hybrids and electric cars (2, 5, 60 Ah) would require large surface areas (500, 1,250, 15,000 cm^2), leading to correspondingly tiny ARs ($1.2x10^{-4}$, $7.5x10^{-5}$ and $2.2x10^{-5}$).

By extending our study to lithium foils spanning ARs of 2 to 0.045 we can see a corresponding range of yield strengths from 0.66 to 1.86 MPa, even while maintaining constant temperatures and strain rates. Measuring such a strong rise in yield strength as a function of aspect ratio has potentially significant implications for future lithium anode designs and we feel is an important result for both the battery and mechanics community.

4.2.5 Multifactor sensitivities and the Cook and Larke model

The impact of aspect ratio in tandem with temperature on flow stress is plotted in **Figure 4.3**. As can be observed, increasing the temperature has the effect of significantly decreasing the flow stress for all samples of lithium. It can also be seen that the reduction in aspect ratio also mildly increases the flow stress regardless of temperature.

The impact of increasing the strain rate in addition to varying the aspect ratio is shown in **Figure 4.6**. Here we can see that increasing the strain rate has a correspondingly large impact on increasing the flow stress, again seen across all lithium samples. It is also seen that the effect of increasing flow stress appears to be increasing as aspect ratio decreases, potentially having a significant effect on thin film lithium with very low aspect ratios.

Various efforts have been made to model the mechanical strength needed in a separator to prevent the penetration of lithium dendrites [64, 65]. Based on these modeling results, it has been estimated that a polymer separator with twice the shear modulus of lithium would be able to inhibit

penetration. Attempts to apply this result to solid separator systems such as LLZO have proven challenging, as despite a LLZO shear modulus (59.6 GPa [135]) significantly greater than lithium (2.83 GPa [42]), penetration has been well documented [118]. The ability of lithium metal to penetrate solid state separators such as LLZO has raised significant questions about our understanding of the mechanics involved and has led to renewed interest in the mechanics of the lithium solid state interface [118]. Analysis of this interface can be complicated by numerous compounding factors such as surface roughness, wettability, and the presence/evolution of a solid electrolyte interphase (SEI).

In one work attempting to model the lithium solid state interface, Newman and Ferrese describe a lithium anode with an aspect ratio of $1x10^{-4}$, similar to what we project you would find in a small LMSSB [42]. These authors assume that lithium is constrained to movement in only one axis in the direction of the cathode for simplicity. As a result, when lithium is pushed again a battery cell wall, this is how it is constrained and prevented from squeezing out of alignment with the separator and cathode. During our study of lithium compression, we have observed the real world resistance of lithium to being squeezed out and attribute it to hydrostatic pinning, similar to what has been proposed by Cooke and Larke for a copper system [99]. Further, the authors assume a constant yield strength of lithium of 0.655 MPa based on the work of Tariq et al., likely owing to the limited published lithium metal mechanics data available at the time [62]. This work highlights the sensitivity of the lithium flow stress to aspect ratio, temperature and strain rate, demonstrating that yield strength depends strongly on the testing conditions. We have shown that the lithium yield strength can either be several times smaller when heated (0.26 MPa at 0.893 TH, AR2 and $1x10^{-3}$ s^{-1}) or multiples larger at reduced sizing (1.86 MPa at 0.661 TH, AR0.045 and

$1x10^{-3}$ s^{-1}). The strong alignment with other researchers seen in temperature (**Figure 4.5**) and strain rate (**Figure 4.7**) supports the trends of sensitivity seen in this work.

Previous mechanical testing of the relatively soft metal copper in compression has yielded some similar results to our study of lithium [99]. As was referenced in the subsection on stress strain behavior as a function of aspect ratio, the initial elastic region slope deviates strongly from the yield strength determined by other methods for both copper and lithium. Additionally, the increased stress seen after flow begins in the absence of work hardening can also be attributed to the hydrostatic pinning phenomena proposed by Cook and Larke. During our experiments, our test samples and platens were lubricated with mineral oil and yet significant barreling was seen. As a result, the flow under compression is reduced and the resulting flow stress to maintain plastic deformation is increased substantially beyond the traditional yield strength. A conceptual schematic visualizing the impact of strain rate and temperature changes on the hypothesized zones of hydrostatic pinning is shown in **Figure 4.12**. When the two pinned regions meet and the region of flow is severely reduced it maybe that an effective flow stress plateau is reached, hypothesized to be in the range between 14 and 20 MPa [136].

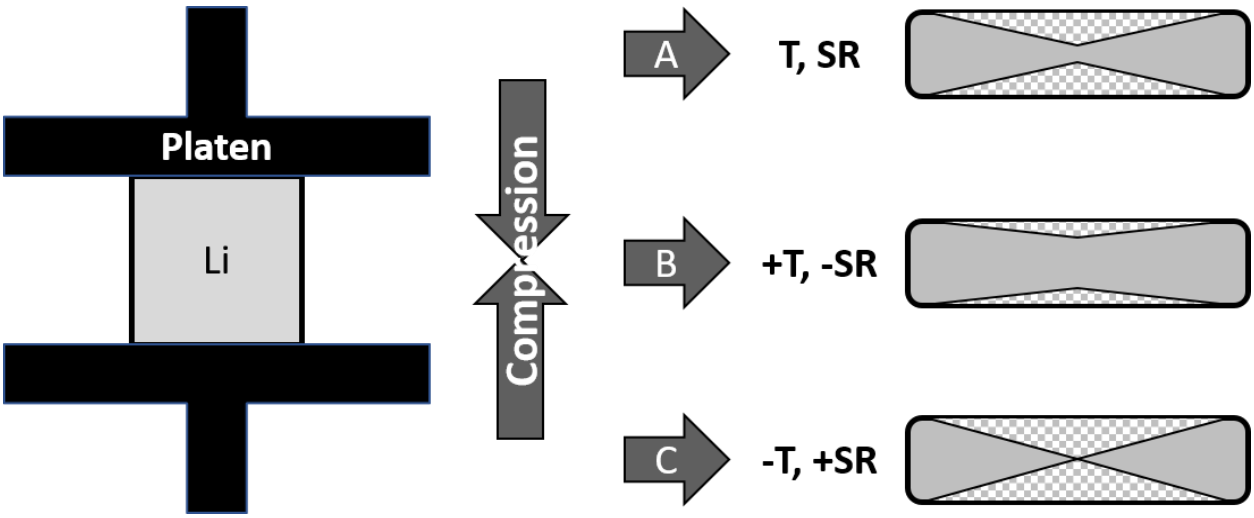

Figure 4.12: Schematic diagram depicting the conceptual evolution of a highly ductile sample geometry (barreling) during compression under various conditions. The cross-hatched regions indicate where limited deformation occurs adjacent to the platens due to friction. A) Room Temperature (T) and ASTM Strain Rate (SR), B) Reduction in pinned material cross-hatched zone created by raising temperature (+T) and lowering strain rate (-SR), C) Growth in flow trapped material region as a result of lowering temperature (-T) or increasing strain rate (+SR) [42, 99]

Although these values are high for lithium, they are far below the theoretical limit for yield. The maximum theoretical yield strength of a material can be estimated as the shear modulus divided by 2π to 30, or in the case of G_{Li} = 2.83 GPa , approximately 94 to 450 MPa [42]. By viewing the theoretical flow stress upper limit of lithium in context of the recent micro-pillar [120] and thin film [121] work, the size-based strengthening of lithium metal may explain the observed penetration of solid-state electrolytes seen in the literature [118].

4.3 Conclusions

LMSSBs hold the potential for significantly improved energy densities compared to traditional lithium ion batteries [35]. The potential for these energy improvements and challenges remaining manufacturing lithium anodes have been highlighted by the US automakers in a recent call for proposals for beyond lithium ion cells and anodes by the USABC [137]. By varying the

geometry, temperature and strain rate of compression testing of lithium billets, the resulting flow stress was found to vary by almost one order of magnitude (0.21 to 1.86 MPa). Flow stress was shown to be strongly inversely proportional to temperature and directly proportional to strain rate. Modern battery designs are likely to experience the temperature and strain rate regions evaluated, indicating that the effective yield strength of lithium in actual devices will likely also vary by at least an order of magnitude.

Lithium's flow stress varied consistently with other materials as a function of temperature [43, 132] and in particular, BCC metals with regards to strain rate [127, 128, 134]. Despite being well lubricated, lithium exhibited significant barreling in compression, in line with the hydrostatic pinning previously reported in highly ductile copper [99]. By combining the previously measured elastic constants of lithium [42] with the empirical and theoretically determined maximum flow stress of lithium, it was possible to place an upper bound of strength of 94 to 450 MPa [138]. This upper range of theoretical strength encompasses the lithium values reported micro-pillars [116, 120] and thin films [121]. The measured variable sensitivity of lithium flow stress measured in this work and others can provide further insight into the mechanisms involved in the mechanical penetration of hard ceramics such as LLZO by what is traditional thought of as soft lithium metal [118].

4.4 Acknowledgements

The Ford-University Michigan Alliance program (Grant # UM0163) funding support is acknowledged. Thanks are given to Jeff Wolfenstine and Kent Snyder for helpful conversations.

Chapter 5

Safety Considerations of Lithium Metal Solid State Batteries

The improved safety performance of lithium metal solid state batteries (LMSSB) is often cited as an inherent benefit without any technical support other than removal of the flammable liquid electrolyte. This study holistically addresses the safety properties of lithium metal in LMSSB using a Fault Tree Analysis approach and then investigates the main identified areas of concern, namely water exposure, air exposure and vibration [139].

5.1 Introduction

The ubiquity of portable electronics and recent growth in electric vehicles has been spurred by the steady improvement of the LIB. However, despite significant product engineering and research efforts worldwide, the average annual rate of specific energy improvement has been 8%/year and this rate is slowing down [29, 140]. LMSSB or batteries using a solid as a combination electrolyte/separator and lithium metal as the anode are the most promising next generation battery cell type. The incorporation of lithium metal in place of the traditional carbon anode can lead to a significant gain in cell energy density [35]. However, there remain many life and performance questions regarding this cell type [36, 126]. To meet the needs of the automotive market, LMSSBs would need to meet long life requirements such as 1,000 cycles and 15 years calendar life [27]. Despite the potential importance of the addition of lithium metal to battery energy, significant unknowns remain regarding its behavior. For example, some of the basic mechanical properties of lithium such as the elastic constants, plastic responses and creep

mechanisms have only recently been investigated [42]. Additionally, the mechanical behavior in temperature, strain rates (i.e. charge/discharge rates) and aspect ratios of most relevance to battery applications are also a field of active research [98]. To date there has been limited safety testing of solid state electrolyte materials, with initial efforts focused on using existing LIB techniques such as accelerated rate calorimetry, ARC [89].

Although Sony commercialized the first LIB for the consumer electronics market in 1991, it wasn't until 2008 with the serial production of the Mercedes Benz S400 Hybrid Electric Vehicle that the technology entered the automotive market [29]. Since then, the transition from aqueous based chemistries such as Lead Acid (PbA) and Nickel Metal Hydride (NiMH) to the family of LIB chemistries based on flammable inorganic solvents has been completed for the traction power in almost all hybrid, plug-in hybrid and electric vehicles. The wide-spread adoption of this technology has also promoted additional research into the safety of LIBs in automotive applications on a, mechanical [47, 48], thermal [49, 50], electrical [51, 52] and systems basis [53, 54].

As an evolving next generation battery system, LMSSB are a rather immature technology, with significant questions regarding basic system feature such as chemistry, cost, durability and safety. To this end, a FTA was performed of LMSSB to identify possible safety hazards and durability deficits of interest (see **Figure 5.1**). The usage of lithium metal in the LMSSB would mark the return of the material to secondary battery mass production for the first time in decades [45, 46]. The nature of reaction of lithium metal to environmental exposure, i.e. atmosphere in terms of quality and liquid water in terms of safety, was highlighted in the FTA and is not well studied. Advocates of LMSSB point to increased safety performance over the LIB based on the replacement the flammable liquid solvents with a solid electrolyte as an inherent benefit.

However, the safety implications of the addition of lithium metal, a highly reactive pyrophore which exothermically decomposes water into hydrogen gas [41], is often overlooked. The potential hazards of lithium metal can range from mild performance issues in the case of exposure to environmental gases (oxygen and nitrogen) and water vapor to severe in the case of liquid water. As a result, maintaining LMSSB mechanical case integrity during normal use (i.e. vibration) and abnormal abuse (i.e. mechanical shock, crush) will be of greater importance compared to LIBs. Additionally, beyond the potential hazards of external cell case failure, internal mechanical failure may also pose new safety hazards in LMSSB. For example, an additional durability and potential safety issue identified by the FTA was the brittleness of the solid state electrolyte and their susceptibility to facture under either vibration (in use) or mechanical shock (under abuse). These three potential faults, Water Exposure, Air Exposure and Vibration were determined to be of greatest interest following the FTA and constitute the focus of this work.

5.2 Results & Discussion

5.2.1 Fault Tree Analysis

A Fault Tree Analysis (FTA) was performed to determine the new potential safety considerations in LMSSBs. As LMSSBs are only in the research stage, particularly for automotive applications, the more general design philosophy of FTAs was deemed preferable to that of an FMEA. Our FTA was built on a large FTA performed on LIBs in a previously published study [53]. The research focus of the previous FTA was to consider safety considerations introduced by the transition from aqueous battery chemistries such as lead acid and nickel metal hydride to lithium ion and was performed between 2011 and 2014 for the US automotive safety regulator, NHTSA [53]. By design, the previous FTA only considered hazards arising from the changes in battery chemistry, and served as a guide for the current study in analyzing the potential

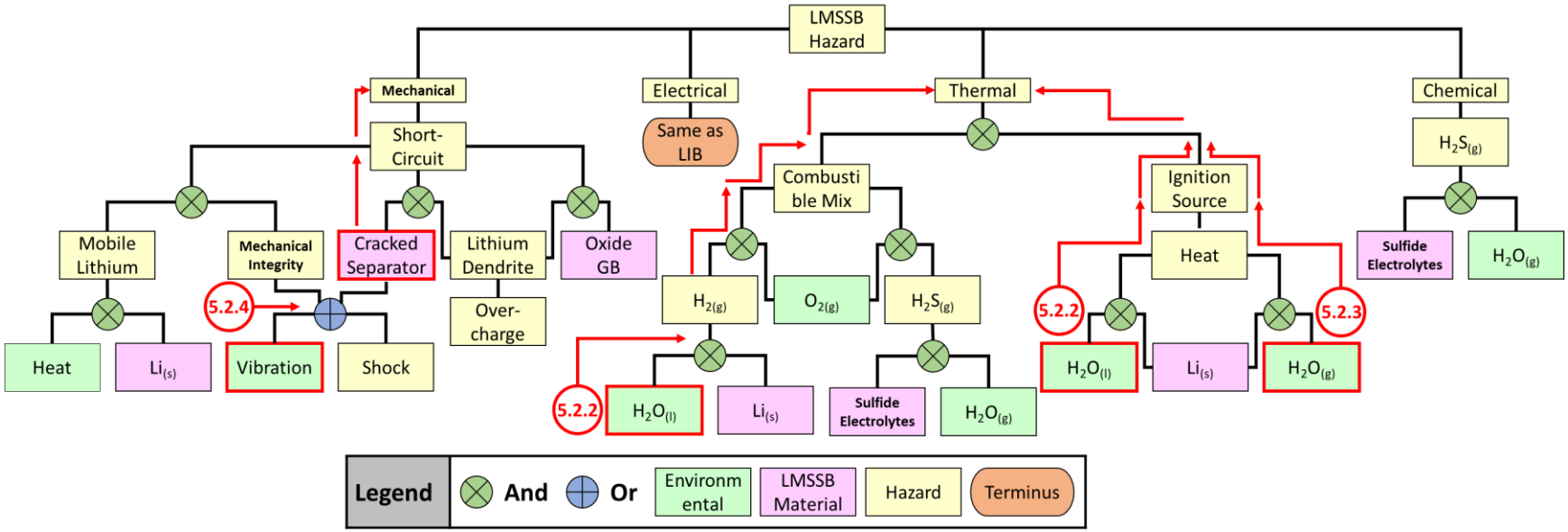

Figure 5.1: Fault tree analysis of LMSSB described in sections 5.2.2 (Water Exposure), 5.2.3 (Air Exposure) and 5.2.4 (Vibration) are highlighted in red.

transition from LIB to LMSSB. The two main materials changes considered in this study were the replacement of carbon with lithium anodes and the inorganic flammable solvent based electrolyte and polyolefin thin film separators with solid ceramic or glass electrolytes.

5.2.1.1 FTA: Mechanical Branch Faults

Most mechanical branch faults hazards are unaffected by the transition from LIB to LMSSB chemistries (see **Figure 5.1**). For example, the US safety regulation FMVSS 305's mechanical retention requirement of the battery pack is unaffected by chemistry [141]. However, one potentially significant difference is the mechanical durability of the solid electrolyte material itself. Compared to the polyolefin thin-film of LIBs, the electrolyte/separator in LMSSB in many cases maybe susceptible to cracking. In automotive applications, regular vibration patterns under normal use are characterized by long duration, repetitive, relatively low acceleration pulses, such as 1-8 g for 15 minutes [142]. Mechanical shocks experienced during abusive failure conditions are characterized by shorter duration, relatively high acceleration pulses such as 50-150 g for 11-18 milliseconds [142].

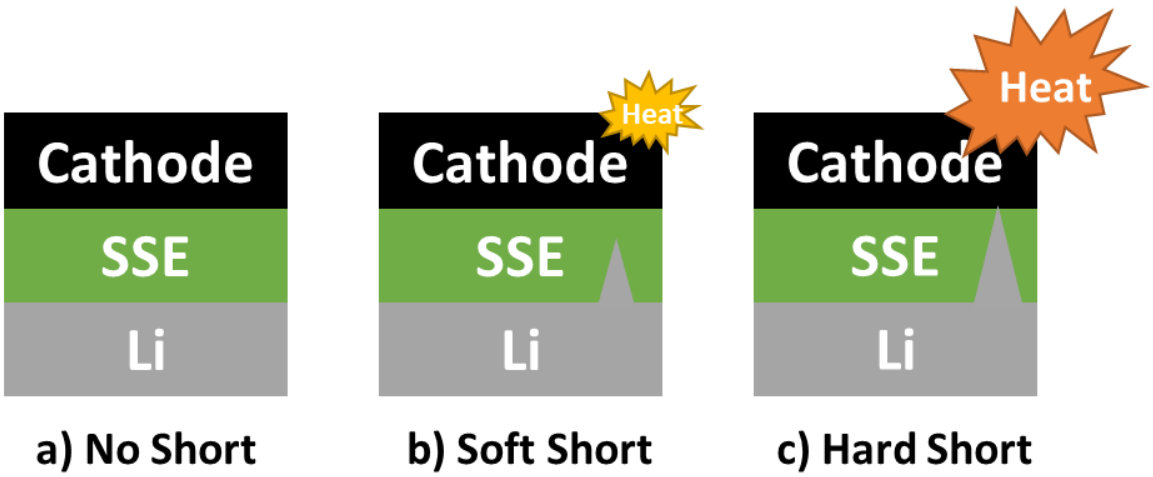

Figure 5.2: Schematic of Potential Short-Circuit Evolution in LMSSB from a) No short, b) Soft Short and c) Hard Short

If either vibration during normal use or mechanical shock during abuse caused the solid state electrolyte to crack, it could expose an open conduction path across the cathode and anode, potentially leading to an electrical short-circuit (see **Figure 5.2**). In the best case of mechanical damage, a mild or soft short-circuit could lead to increases in the cell self-discharge rate and could be temporary as successive plating and stripping of lithium dynamically changes the structure of anode/separator interface (see **Figure 5.2b**). In the worst case, a severe or hard short-circuit may lead to shunting of significant electrical currents leading to localized joule heating, which could cascade into a thermal runway of this cell (see **Figure 5.2c**). Additionally, a mechanical integrity issue may be complicated by elevated temperatures which could melt the lithium (180.5°C melting point) [**143**] and allow it to flow out its designed location leading to a short-circuit (see **Figure 5.2**). For the oxide materials which form ceramics, there is also a known failure mode of overcharge events leading to the growth of lithium dendrites which can penetrate the grains and grain boundaries (GB) [118].

5.2.1.2 FTA: Electrical Branch Faults

No unique electrical hazards were identified with the transition from LIB to LMSSB (see **Figure 5.1**). This is due to the comparable cell voltages between cells with a graphite versus lithium metal anode. Additionally, a LMSSB would be implemented in an electrically similar manner as an LIB in terms of module/pack/electrical bussing design in an electrified vehicle, thereby introducing no new electrical hazards. For example, the main electrical hazard concern in the US vehicle safety regulation, FMVSS 305 requires maintaining a 500 ohms/volt isolation between the propulsion system and the vehicle's structure [141]. This requirement is not impacted by the choice of battery chemistry in the case of LMSSB versus LIB or otherwise.

5.2.1.3 FTA: Thermal Branch Faults

The thermal branch was found to be the largest source of potential hazards for LMSSB (see **Figure 5.1**) as in the case of LIBs [53]. To trigger a thermal event, both an ignition source and a combustible mixture is required. In the case of LMSSB, the exothermic decomposition of lithium metal in contact with liquid water [41] is able to generate sufficient heat (net heat of reaction of 201.7 kJ/mol) to serve as an ignition source. It has been estimated that 1500 vehicles each year are submerged in the USA, which given the estimated 193 million vehicles in the US vehicle parc makes this a rare event [144, 145j]. Given the strongly exothermic nature of lithium metal's reaction with water, studying the behavior of LMSSB's during water immersion is an important safety topic.

Existing LIBs have been tested thoroughly in salt water immersion baths as part of various safety test standards [79], regulations [84] and research studies at the cell [144] and pack level [146]. Broadly these tests have shown the opportunity for mild self-discharge (slow short-circuit) of cells, leading to corrosion at terminals and temperature rises in the water bathes, but not

significant safety events. No comparable studies have been performed of LMSSBs and demonstrating similar safety behavior to LIBs will be critical to alleviate safety concerns among vehicle manufacturers. In addition to the possibility for generating an ignition source through heat as described above, LMSSB may also be able to generate a combustible mixture, thereby resulting in a thermal event. This could be created by either the generation of hydrogen gas (H_2) as lithium metal decomposes liquid water [41] or hydrogen sulfide (H_2S) gas as solid sulfur electrolytes are decomposed by moist air [147]. The explosive ranges of hydrogen sulfide and hydrogen gas in air are 4.5-45.5% and 4-75% as published by OSHA, respectively [148, 149]. Lithium metal decomposes into lithium hydroxide (LiOH) on contact with liquid water and in the process generates hydrogen gas [41]. Moist air decomposes many sulfide solid electrolytes materials and can generate hydrogen sulfide gas [147].

5.2.1.4 FTA: Chemical Branch Faults

The main unique chemical hazard identified as being associated with LMSSB was the possible generation of hydrogen sulfide gas resulting from the decomposition of sulfide solid electrolytes in contact with moist air [147]. Although in the thermal branch discussion, the explosive range of hydrogen sulfide was identified as 4.5 to 45.5%, it should be noted that these values far exceed the permissible exposure levels set by OSHA of 50ppm for up to 10 minutes as a general industry peak value due to the gas's toxicity [148]. It is also notable that the requirement of FMVSS 305 to maintain electrolyte leakage to 5L or less would be made redundant by the transition to a solid electrolyte based battery [141].

5.2.1.5 FTA: Hazards Summary

Based on the unique issues identified in the FTA of LMSSB, an experimental plan of study was developed to explore the potential safety hazards. A pattern of external environmental (either

atmospheric or test environment) factors acting on the unique materials of LMSSBs was observed. During any vehicle safety incident it is common for water to be applied to a damaged vehicle, as a result the possibility of LMSSBs to create a thermal event when exposed to water is of significant safety importance (see Section 5.2.2). Air exposure is considered to be more of a quality, rather than safety issue, but the importance of pure lithium in the LMSSB assembly and the ease with which a cell could be ruptured during abuse led to its evaluation (see Section 5.2.3). The possibility of certain LMSSB electrolyte materials, namely ceramics and glasses, to crack during vibration and mechanical shock was also identified as a priority safety hazard to investigate (see Section 5.2.4).

5.2.2 Water Exposure

Lithium metal is known to exothermically react with liquid water, leading to the precipitation of lithium hydroxide (LiOH), evolution of hydrogen gas (H_2) and a net heat of reaction of 201.7 kJ/mol [41, 150]. In the case of an EV powered by a LMSSB, based on battery engineering design parameters, it is possible to establish a relation between lithium metal and EV range. For such a LMSSB powered EV to achieve 300 mile range, it would need approximately 7 kilograms of lithium (see **Figure 1.7**) [150]. This amount of lithium could theoretically release 204 MJ of thermal energy if it was all exposed to liquid water, a heat value approximately equivalent to 4.6L of gasoline. Based on this large amount of potential heat content, it is important to clarify the quantity and manner in which lithium might be practically exposed to liquid water in a LMSSB automotive application.

Figure 5.3: Water Exposure Test Chambers, (L) Chamber #1, (R) Chamber #2

Initial experimental efforts were devoted to confirming the heat generation of lithium's water exposure aligned with the identified mechanism above and used Chamber #1 described in the Section 2.3.3 and Section 5.2.2.1 (see **Figure 5.3L**). Lithium samples in range from 0.2 to 1.0 grams were submerged in water either attached to weights (see **Figure 5.4** and **Figure 5.7**) or sandwiched in between glass slides held together by springs (see **Figure 5.5** and **Figure 5.7**), which applied an approximately fixed amount of load.

Figure 5.4: Lithium foil is attached to a copper weight to enable it to be submerged in water in an insulated vessel (Chamber #1), 30 second duration and x4 time speed.
Video URL: https://youtu.be/zUNamZn1p8M

Submerged samples generated the highest amount of heat and bubbles as all of the emitted hydrogen gas passed through the water bath. The wrapped samples emitted a lower amount of bubbles over a more prolonged period of time and provided an opportunity to see a decomposition wave front through the glass slide wrapping. By using approximately the same weight of lithium foil held between glass slides, but with varying thickness we can study the impact of water inlet geometry under the fixed load setup of wrapped samples in Chamber #1 (see **Figure 5.5** and **Figure 5.8**).

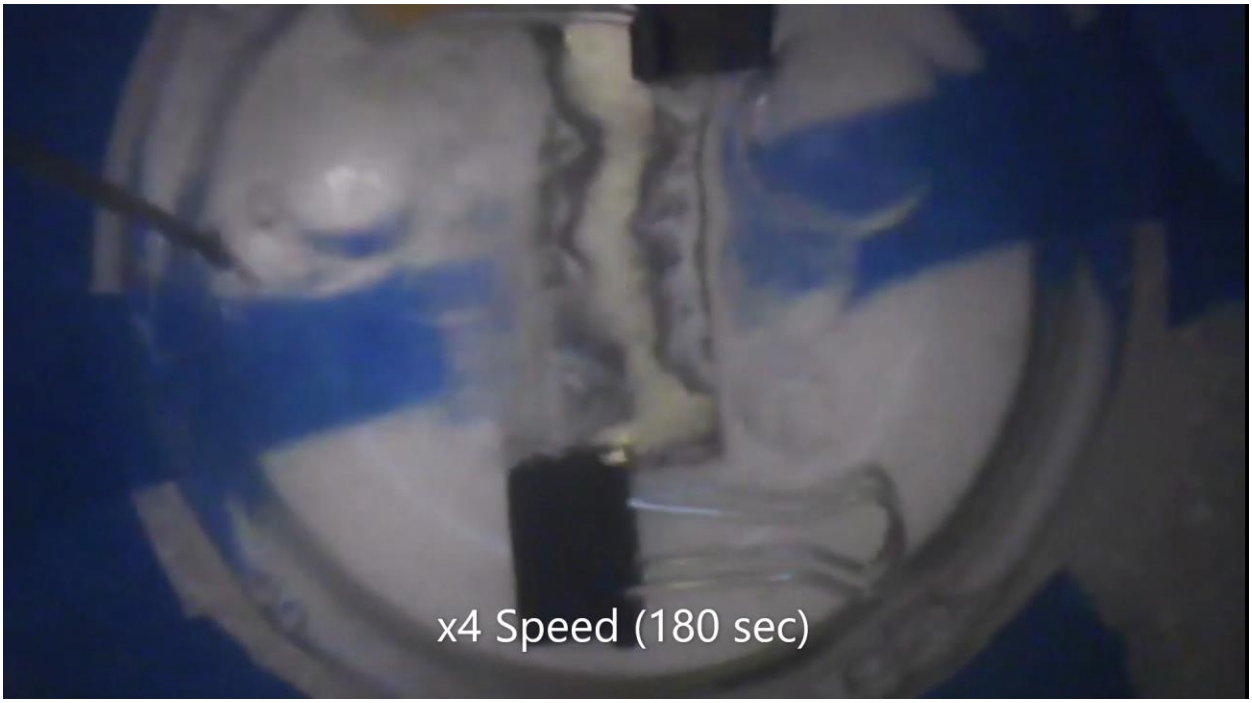

Figure 5.5: Lithium foil wrapped in between glass slides is exposed to water in an insulated vessel (Chamber #1), 180 second duration and x4 time speed.
Video URL: https://youtu.be/fQarv5VQI8U

Following these initial experiments, a second water exposure container (Chamber #2, see **Figure 5.3R**) and lithium holder (acrylic circular) were fabricated (see **Figure 5.6** and **Figure 5.11**). This experimental setup allowed us to submerge lithium foil in water while maintaining a fixed thickness available to water for inlet. Additionally this lithium holder has in plane symmetry and allowed for the development of an optical lithium consumption calculation described in Section 5.2.2.2.

Figure 5.6: Lithium foil disk is placed in between two circular sheets of acrylic and exposed to water in an insulated vessel (Chamber #2), 11.5 minutes duration and x32 time speed.
Video URL: https://youtu.be/KcypK1dS_4g

During these second rounds of experimentation, the trends in thermal heat generation of lithium were confirmed in smaller sample sizes. Additionally, the circular jig provided a greater degree of dimensional control and allowed us to use the lithium thickness as a variable during water exposure. In a practical LMSSB design, lithium metal will need to be very thin, in the range of 50 um, and in either a laminate or jellyroll structure. As a result, even under full water immersion of an exposed LMSSB cell, lithium's basal plan will be shielded from water, leaving only the edge plane as a reaction front. A second benefit of the circular jig was improved imaging of the lithium reaction itself which enabled the development of an optical lithium consumption calculation method to complement the thermal method developed with Chamber #1 (see **Figure 5.11**).

5.2.2.1 WE: Thermal Method

Initial confirmation of the theoretical thermal heat generation capability of lithium metal in water was explored using Chamber #1 (see **Figure 5.3L**). Within this test jig, a range of lithium samples were allowed to fully react and the resulting maximum temperature generated measured. By performing a heat balancing assessment using the specific heat capacity and weights of all the jig components, it was then possible to compare this empirical value to the theoretical value. A range of lithium weights fabricated as either submerged or wrapped types were tested in this manner (see **Figure 5.7**).

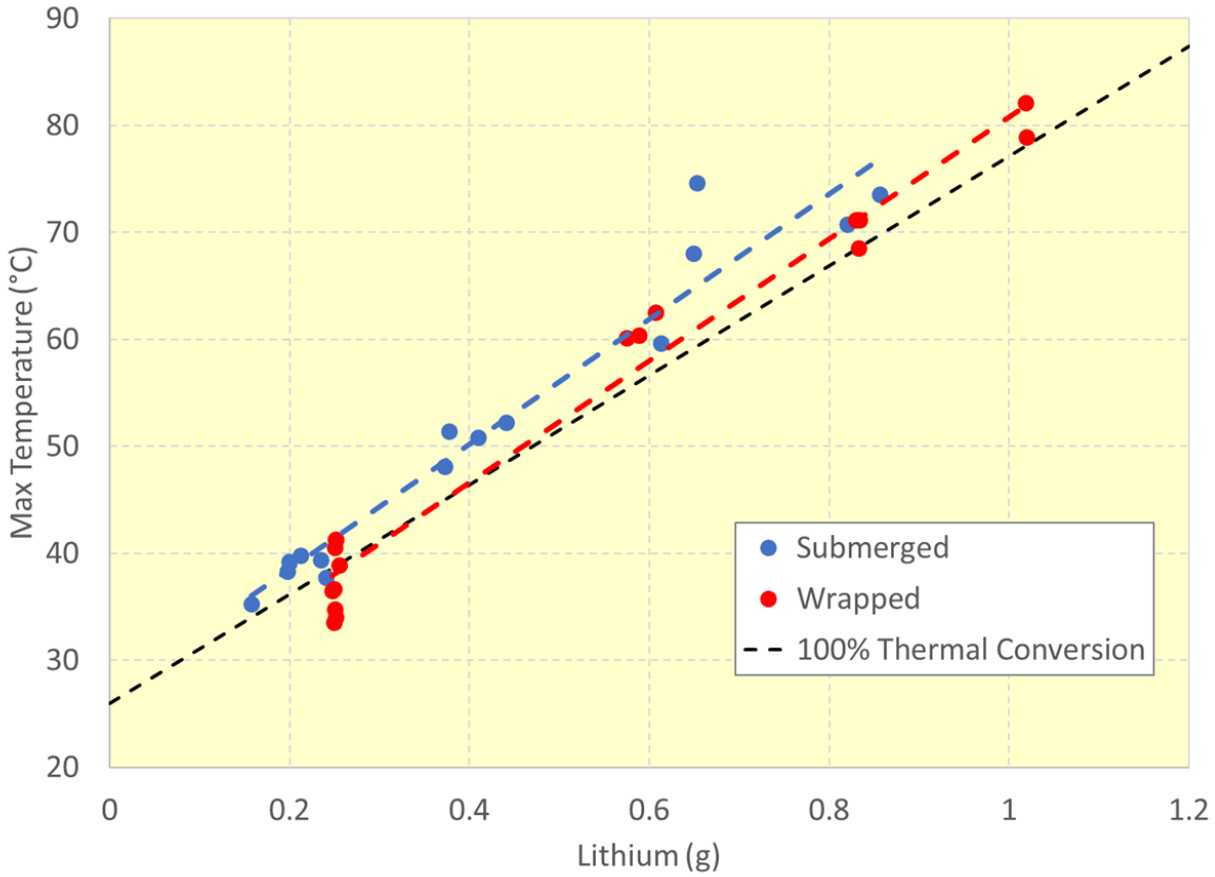

Figure 5.7: Max temperature recorded as function of weight for submerged and wrapped lithium samples tested in Chamber #1

A comparison of these values against a line representing 100% thermal conversion of lithium metal shows a very strong and predictable linear correlation, supporting our proposed mechanism for heat generation. The empirical data was found to slightly exceed the predicted value for 100% conversion at times, which we believe is an artifact due to the generation of local hotspots. Our measured maximum temperature is for the water bath only, but the 100% thermal conversion temperature assumes all materials in the jig (i.e. water and glass) are simultaneously at the same temperature.

Following the confirmation of the thermal method across a variety of lithium weights, the impact of sample height was also explored. In future LMSSB design it is possible that water exposure to the internal electrodes may occur while they are under compression (i.e. fixed load) or not (i.e. fixed thickness). The potential impact of compression load on water exposure was explored using the wrapped lithium in Chamber #1 (fixed load) and the circular jig in Chamber #2 (fixed thickness) setups described in the methods Section 2.3.3.

In the Chamber #1 setup, a fixed load was provided in the wrapped lithium samples resulting in a progressive reduction of the water inlet path as the lithium was consumed. In the circular jig Chamber #2 setup, a fixed gap thickness was set to match the initial lithium height but independently maintained. As can be seen for both scenarios in **Figure 5.8**, in all testing decreasing the original lithium thickness significantly impacted the average temperate rise rate measured during water exposure. In both fixed load and thickness cases decreasing the lithium thickness from 2.25 to 0.75 mm reduces the average temperature rise rate approximately an order of magnitude from 0.15 °C/sec to 0.01 °C/sec. The fixed load setup appears to modestly depress

the fastest rates and elevate the slowest rates, perhaps by reducing the time spent at maximum thickness and minimum thickness while exposed to water.

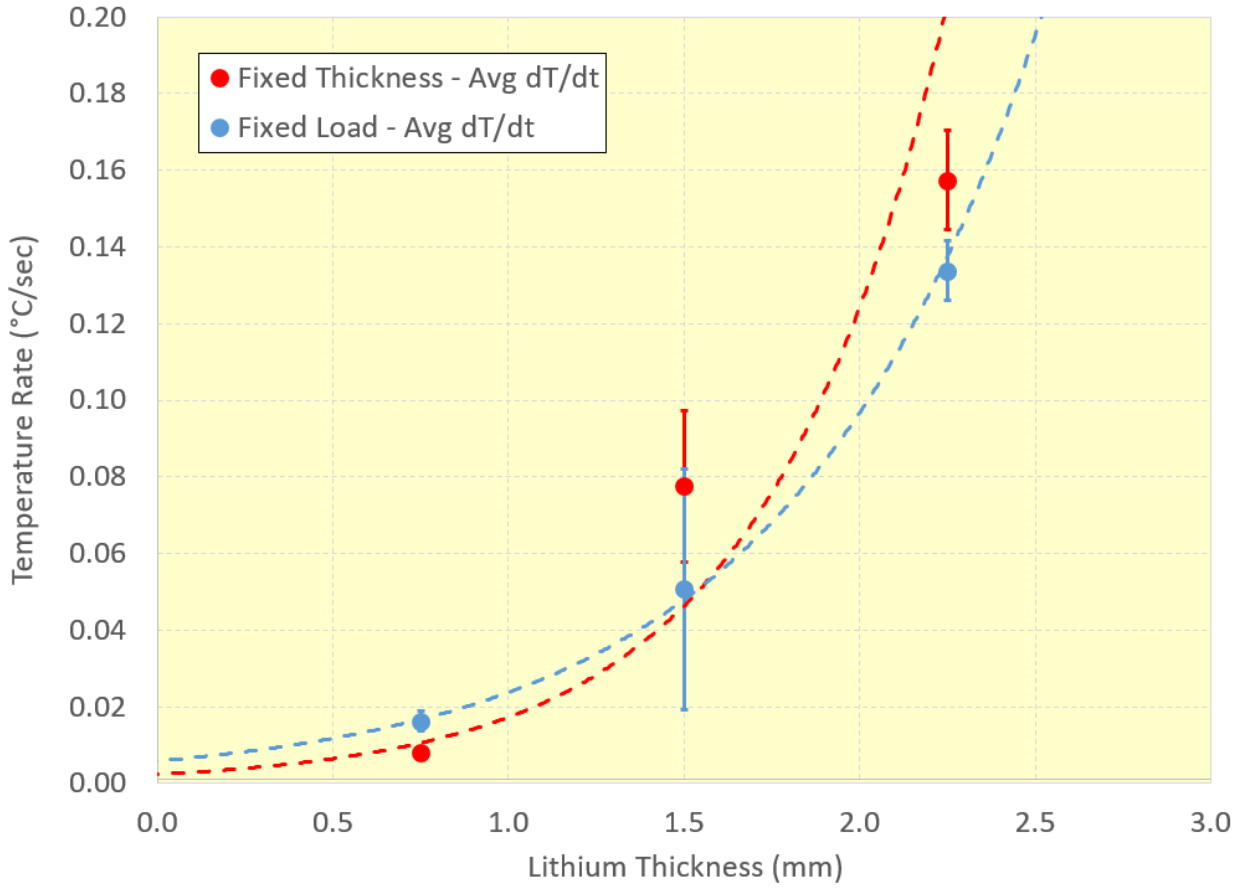

Figure 5.8: Average Rate of Temperature Rise (°C/sec) of lithium metal in water held between glass under either fixed load or fixed gap thickness condition

The impact of fixed load versus thickness was more significantly seen in the overall level of thermal conversion (%) (see **Figure 5.9**). For a fixed thickness, 100% thermal conversion was recorded at 2.25 mm, but only approximately 58% at 0.75 mm, indicating that the inlet path for water was otherwise obstructed. As efficient LMSSB designs will require electrode thicknesses at least one order of magnitude smaller than 0.75 mm, it seems that under a fixed thickness scenario, potentially very little lithium metal would react in the event of an edge plane exposure.

In the case of the fixed load, a conversion of 80% was recorded for all thicknesses, indicating that approximately 20% of the lithium was always left inaccessible to water by the shrinking inlet gap thickness under fixed load. In the thinnest samples measured, the variable thickness of the fixed load scenario had the effect of increasing the level of conversion compared to the fixed thickness setup, potentially by promoting the movement of gas flow and precipitates created as the reaction proceeds, thereby promoting the lithium/water reaction (see **Figure 5.9**).

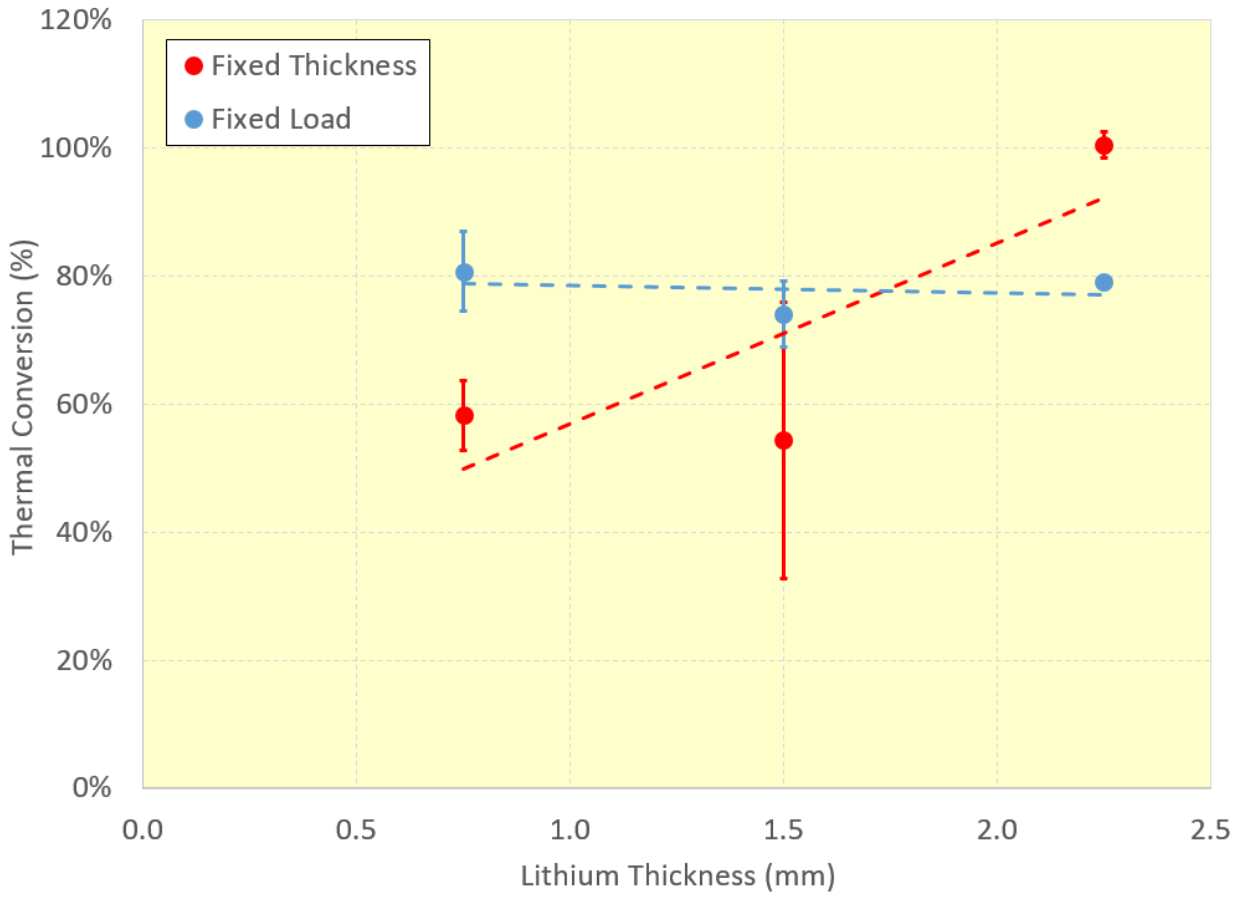

Figure 5.9: Thermal conversion (%) of lithium metal in water held between glass under either fixed load or fixed gap thickness condition

The direct correlation between heat generation and lithium exposure to water allows us quantify the rate of lithium consumption (mg/sec). Further, in the case of Chamber #2 and its fixed thickness setup, we can also normalize this reaction rate by water inlet size (mg/sec*mm) (see **Figure 5.10**). A review of the trend line in **Figure 5.10** indicates that the rate of consumption falls significantly faster than could be explained by merely accounting for the shrinking water inlet size. Based on a review of the thermal data and experiment video (see **Figure 5.6** and associated video) the impact of capillary forces limiting the exit of hydrogen gas and entry of water become more severe as water inlet thickness shrinks is hypothesized.

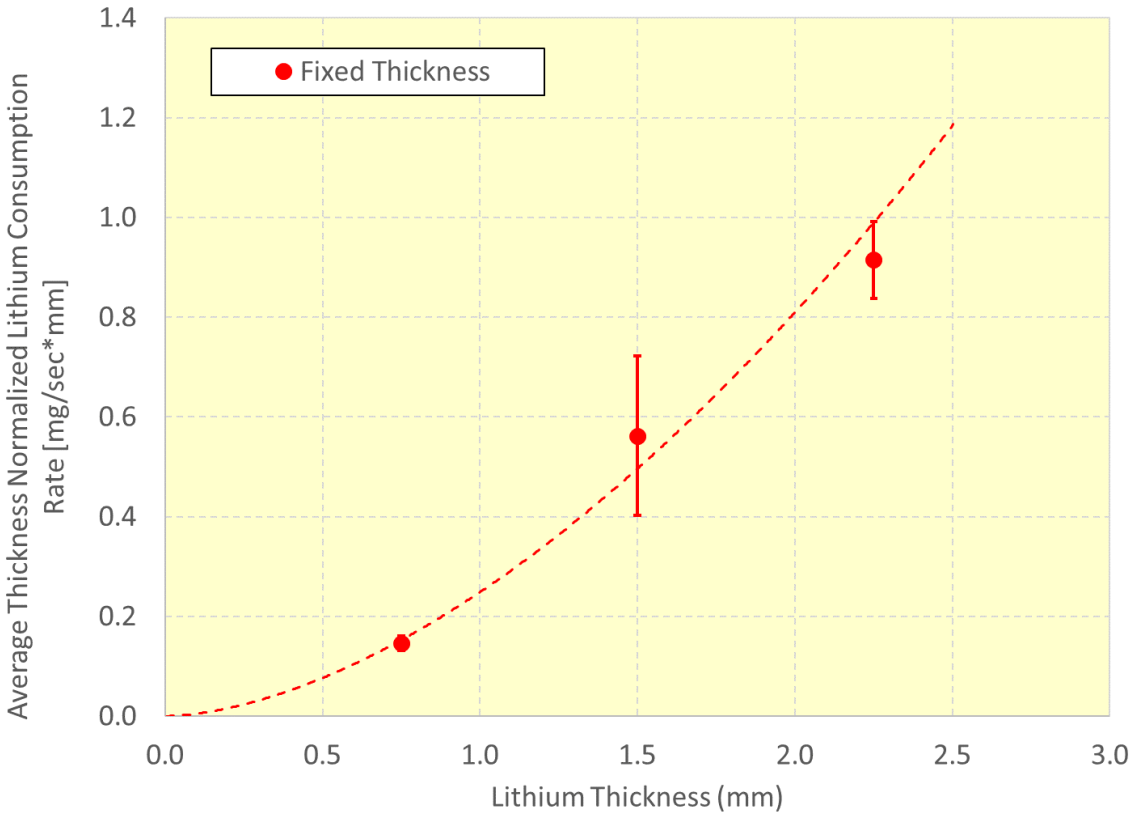

Figure 5.10: Thickness normalized consumption rate of lithium metal (mg/sec*mm) exposed to water in between glass held at a fixed thickness

5.2.2.2 WE: Optical Methods

In an effort to corroborate the results of the thermal method used in Section 5.2.2.1, a separate optical method was developed using the acrylic circular jig and Chamber #2. The new circular jig used four set screws to maintain a constant gap height set by a precision feeler gauge. This jig was paired with the redesigned water bath (Chamber #2) featuring less water & a magnetic stir bar as well as an improved smart phone camera lens & backlighting setup. In addition, the ImageJ processing software was utilized to quantify the amount of lithium consumed based on a visual observation of lithium surface area [107]. Various lithium discs of 750 um thick foil were arch punched and tested individually or stacked to achieve thicker lithium samples (see **Figure 5.13**).

The circular, transparent jig allowed for a visual examination of the lithium/water reaction in a uniform two dimensional plane. As each reaction progressed, noticeable hydrogen gas bubbling was observed and is pictured in **Figure 5.11d** and **Figure 5.11e**. Additionally, it was possible to observe the generation of reaction precipitates during the active reaction and then upon post-test examination of the testing jig (see **Figure 5.11f**). The most likely precipitate is lithium hydroxide which has a solubility limit of 12.8g/100ml at 20°C in water, which translates to about 2.78g of lithium for our 75ml reaction vessel. Although we used about order of magnitude less lithium (0.34g in the case of our thickest test sample, see Section 2.3.3) than what is required to precipitate lithium hydroxide in our entire reaction vessel, in the constrained local environment of the lithium metal itself this concentration threshold would be more than exceeded. As additional support for the local generation of lithium hydroxide, during post-test disassembly, the layer of white precipitate film found inside the test jig were readily dissolved with the additional water.

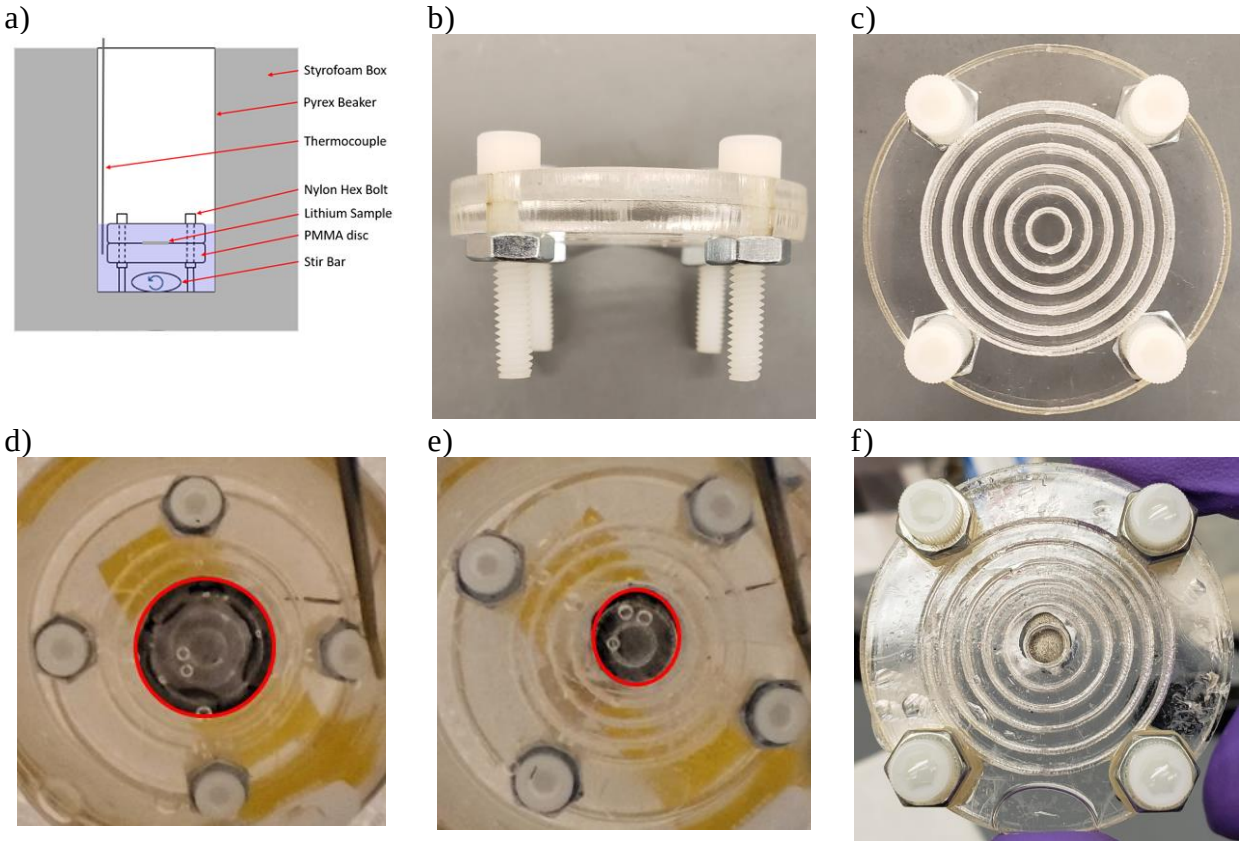

Figure 5.11: Lithium foil water exposure in precision jig (a) schematic of entire setup, (b) circular jig side view, (c) circular jig, top view, (d) circular jig immediately after water exposure and (e) after the main reaction event, ImageJ estimated 64% of surface remains, (f) post test, with circular jig removed from water

During the exposure of lithium to water there is also a visible blackening which occurs as the reaction begins. This darkened lithium promptly disappears as the lithium is reacted more fully, leaving no residue. Based on the color and reactants available, it hypothesized that we are observing the temporary generation of solid lithium carbonate before it is readily dissolved into the water environment. The solubility of lithium carbonate in water is 1.29g/100ml at 25°C which would require 0.18g of lithium in our reaction vessel. Although in the case of lithium carbonate, there is sufficient lithium to create a precipitate in our experiments, the intermediate reactant of carbon dioxide is likely the limiting factor in its generation.

The generation of hydrogen bubbles and a precipitate layer suggest that the interaction between lithium and water in a geometrically confined space may proceed in a complicated fashion, with both phenomena competing with water for access to exposed lithium surfaces. A schematic of these competing mechanisms at the lithium/water interface is depicted in **Figure 5.12**.

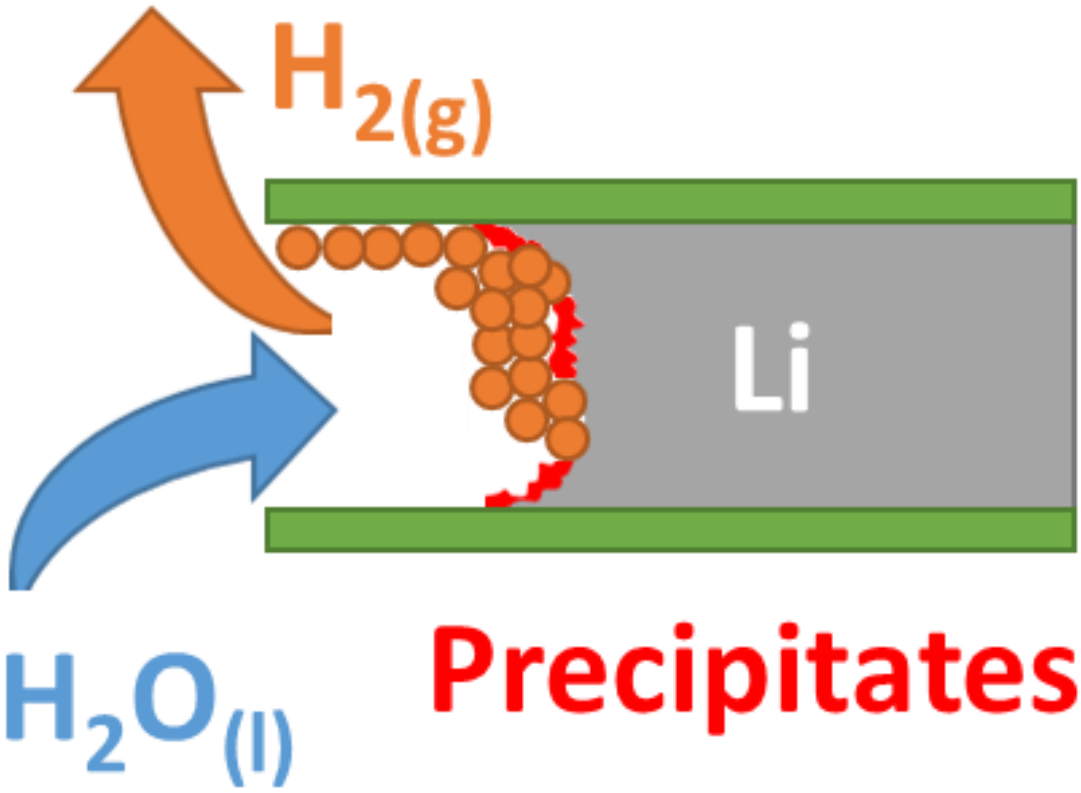

Figure 5.12: Schematic of lithium/water interface during a mechanically constrained exposure

After developing the complementary optical test method, the two lithium consumption analysis methods were used in tandem in an electrode thickness study. Using the circular jig,

lithium foil stacks of 1, 2 and 3 foil punches or 750, 1500 and 2250 µm thickness and matching jig edge plane gaps were exposed to water (see **Figure 5.13**). As can be seem in most cases, the average and standard deviations of the thermal and optical methods gave overlapping results.

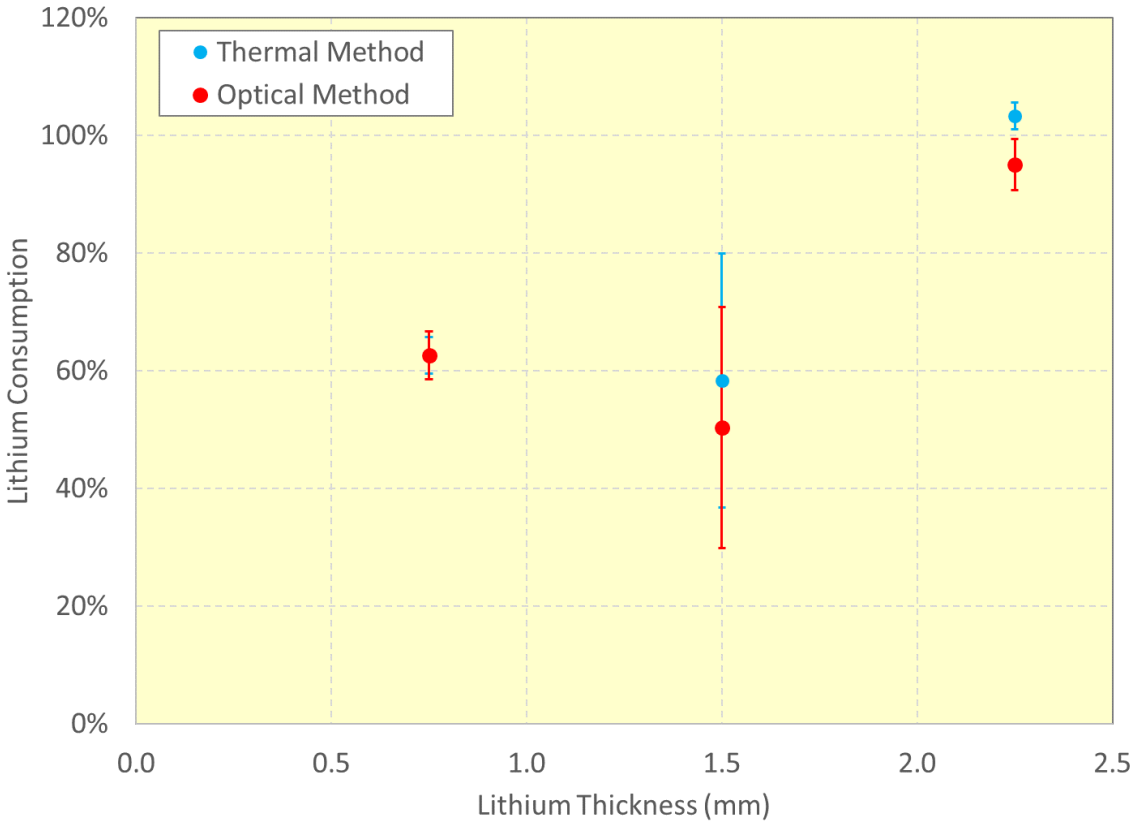

Figure 5.13: Lithium consumption as a function of thickness by the thermal and optical methods.

5.2.3 Air Exposure

When lithium is exposed to moist air, a two step decomposition mechanism yields lithium hydroxide (LiOH) from water vapor which then reacts with carbon dioxide to form lithium carbonate (Li_2CO_3) on the surface [151]. As a means to prevent this, various researchers have attempted to add protect the lithium surface with a variety of coatings [152, 153]. However these coatings can add significant complexity and quality challenges to a product already difficult to

mass produce. Additionally, due to the generation of surface lithium hydroxide and lithium carbonate layers, this reaction is self-limiting. As a result, this reaction does not typically generate enough heat to create a combustible mixture but does result in significant quality concerns.

The quality of lithium metal used during battery assembly is typically only described in chemical terms, such as 99.9% metals basis purity. However, during lithium cell assembly, it has been shown to be beneficial to mechanically scratch the surface [154] thereby scrapping off the native contamination layers of surface films [155] and increasing the reflectivity of the surface. This procedure of scratching lithium until "shiny" is a qualitative technique which for the mass production of lithium metal batteries would require formalization into a quantitative procedure. One such quantitative tool is distinctness of image (DOI) tool used for paint quality appraisal. For example, the BYK wave-scan dual tool consists of a laser beam (high gloss), infrared LED (medium gloss) and CCD camera (dullness) to optically scan the image forming qualities of a surface caused by structures ranging in size from <0.1 mm to 30 mm [108]. This optical profile is then analyzed by being passed through mathematical filters to yield a quantitative value. Due to the matte nature of lithium metal, the dullness rating proved to be the most useful metric. Dullness is defined as a measurement of light scattering, with the scatter value of the overall camera field of measure divided by the max quantity of light reflected in the sensor center and attributed to structures < 0.1 mm.

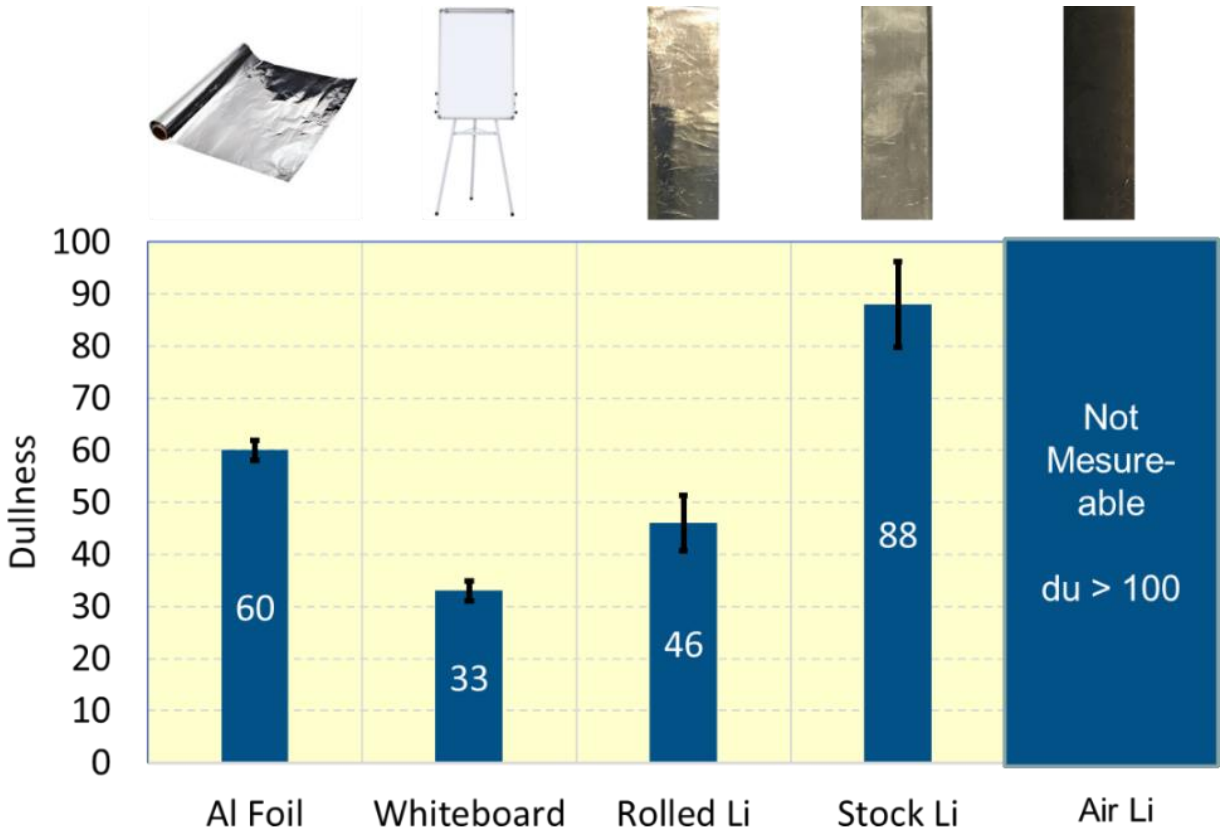

Figure 5.14: Wave-scan dullness of lithium foil (stock, rolled and air exposed) and various reference materials

Various different test samples were prepared for surface dullness analysis by the wave-scan tool. Strips of purchased lithium foil were cut and used either as received or after hand roll-pressing in a glovebox using glass tools. By roll-pressing rather than abrading the lithium surfaces, it was possible achieve a more consistent surface. Lithium samples were then transferred to a -50°C dew point dry room for testing by the wave-scan tool. The lithium samples were tested 5 times each immediately after having their containment bags opened in the dry room and then again thirty minutes later. Additionally three other common smooth lab surfaces were tested for comparison, aluminum foil, a whiteboard and a countertop (see **Figure 5.14** and **Table 5.1**).

Sample	Dry Room Time (min)	Measurements (N=)	Dullness Rating		
			Average	Std. Dev.	COV (%)
Rolled Lithium Foil	0	5	46.2	3.0	6.4
	30	5	46.0	1.2	2.6
Stock Lithium Foil	0	5	87.6	4.1	4.7
	30	5	88.3	2.7	3.1
Aluminum Foil	N/A	10	60.4	0.9	1.5
Whiteboard	N/A	9	33.3	1.0	2.9
Countertop	N/A	9	87.5	9.2	10.6

Table 5.1: Dullness measurement of various surfaces

Both lithium samples showed consistent dullness ratings initially and after 30 minutes in the dry room environment. The stock lithium foil had a dullness rating of 88.3 ± 2.7 compared to the rolled lithium with a value of 46.0 ± 1.2, showing a significant decrease. The dullness ratings for a phenolic resin lab countertop was 87.5 ± 9.2, comparable to the stock lithium in value if not in consistency. Aluminum foil was measured at 60.4 ± 0.9, a value lower than the stock lithium, but higher than the roll pressed lithium foil. The lowest level of dullness measured was for a whiteboard at 33.3 ± 1.0, the only surface measured to be more reflective than the rolled lithium (see **Table 5.1**). Following this initial characterization, the lithium samples were transferred to the room environment {~11°C dew point), whereby both surfaces began to immediately blacken (see **Figure 5.15**). After approximately 5 minutes, each surface was measured for dullness and reported the maximum device reading of 100, confirming a significant change in the lithium surface due to moisture exposure.

a) b)

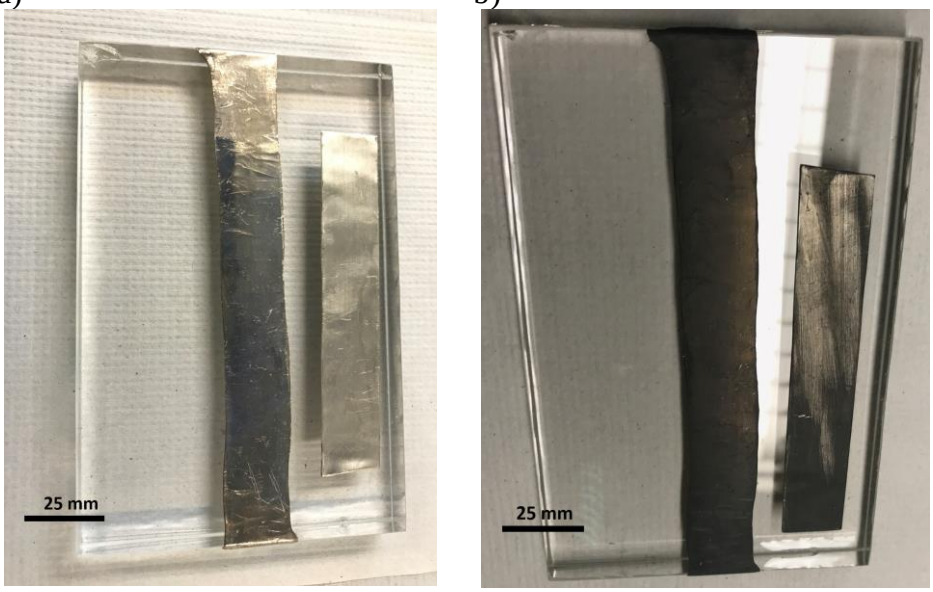

Figure 5.15: Lithium samples, (L) roll pressed and (R) as received in different environments. (a) Dry room (-50°C dew point) after 30 minutes and then (b) open atmosphere (11°C dew point) after 5 minutes.

The measured values of dullness were matched to the qualitative level of shininess seen in all the samples measured in order of least dull as Whiteboard < Rolled Lithium (Dry Room) < Aluminum Foil < Stock Lithium (Dry Room) < Countertop < Rolled & Stock Lithium (Atmosphere). The agreement between the quantitative assessment of the wave-scan method and the qualitatively observed level of dullness validated the viability the proof of concept of this approach. If LMSSB are to be mass produced, production in a glovebox (~-80°C dew point) is not viable and based on our initial findings likely not necessary. Although much more advanced surface analysis techniques such as XPS [156], TOF-SIMS [157] and AES [158], already exist and can be very informative regarding the surface composition and structure, these methods can be costly in terms of time, expertise and funds. We believe our experimentation with the commonly available wave-scan method, can provide a low cost, fast in-line supplement to these existing analysis techniques.

5.2.4 Vibration

Two of the three main classes of materials being considered for solid state electrolytes, oxide ceramics, sulfur glasses and polymers, belong to historically brittle families of materials. In a LMSSB, the electrolyte also functions as the separator, in charge of preventing short-circuits which raised concerns in our FTA in the event of mechanical failure due to vibration or mechanical shock.

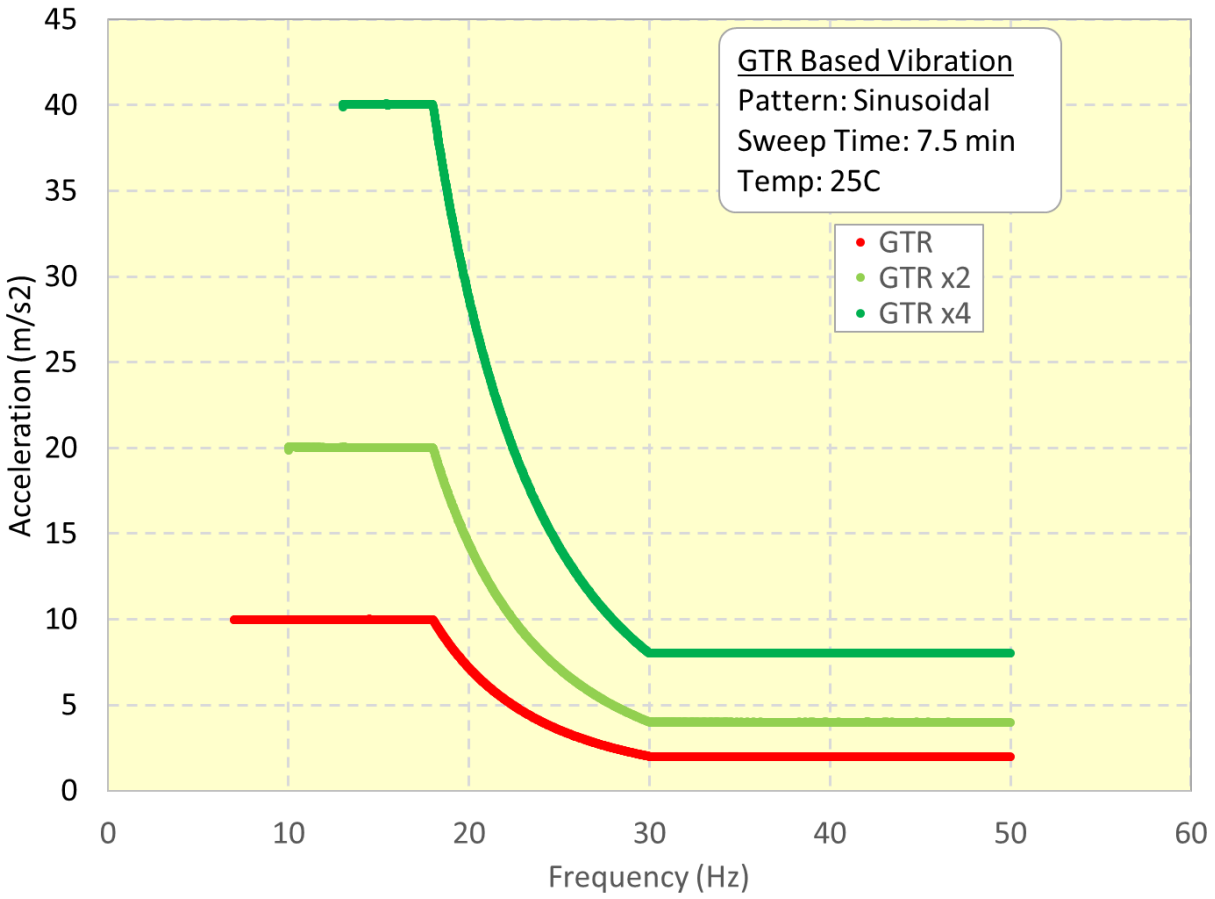

Figure 5.16: GTR vibration pattern, frequency vs acceleration for standard pattern, x2 and x4 maximum acceleration

To initially evaluate the vibration performance of a solid state electrolyte, the test pattern from the UN Global Technical Regulation (GTR), #20 Electric Vehicles Safety, adopted from the ECE R100 regulation, Appendix 8A was used [84]. This pattern's maximum acceleration is 10 m/s^2 with each sub cycle lasting 7.5 minutes, repeated 24 times for a total test time length of three hours. After pellets were tested at the prescribed test pattern, a custom sub cycle with twice and then four times the maximum acceleration was run on each sample (see **Figure 5.16**).

To deliver this vibration pattern, a custom vibration plate was fabricated along with restraint attachments to accommodate four, ½ inch diameter LLZO disks. Initially a rubber pad was placed to shield two of the LLZO disks and two were in contact with the bare aluminum. Qualitatively the test samples were able to show marginal surface damage after being run through the standard GTR Vibration test pattern (see **Figure 5.17**).

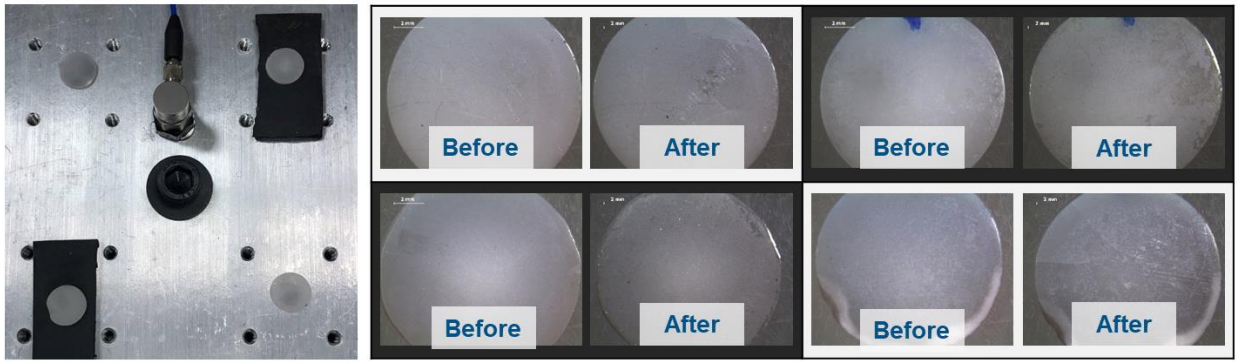

Figure 5.17: LLZO disk vibration plate, disk images before and after.

To facilitate a quantitative study of the vibration impact on the solid electrolyte materials, an in-situ Electrochemical Impedance Spectroscopy (EIS) setup was added to the vibration plate. For these pellets, EIS was run after two, ten and twenty four standard GTR vibration sub cycles, followed by once after a x2 and x4 maximum acceleration sub cycle (see **Figure 5.18**).

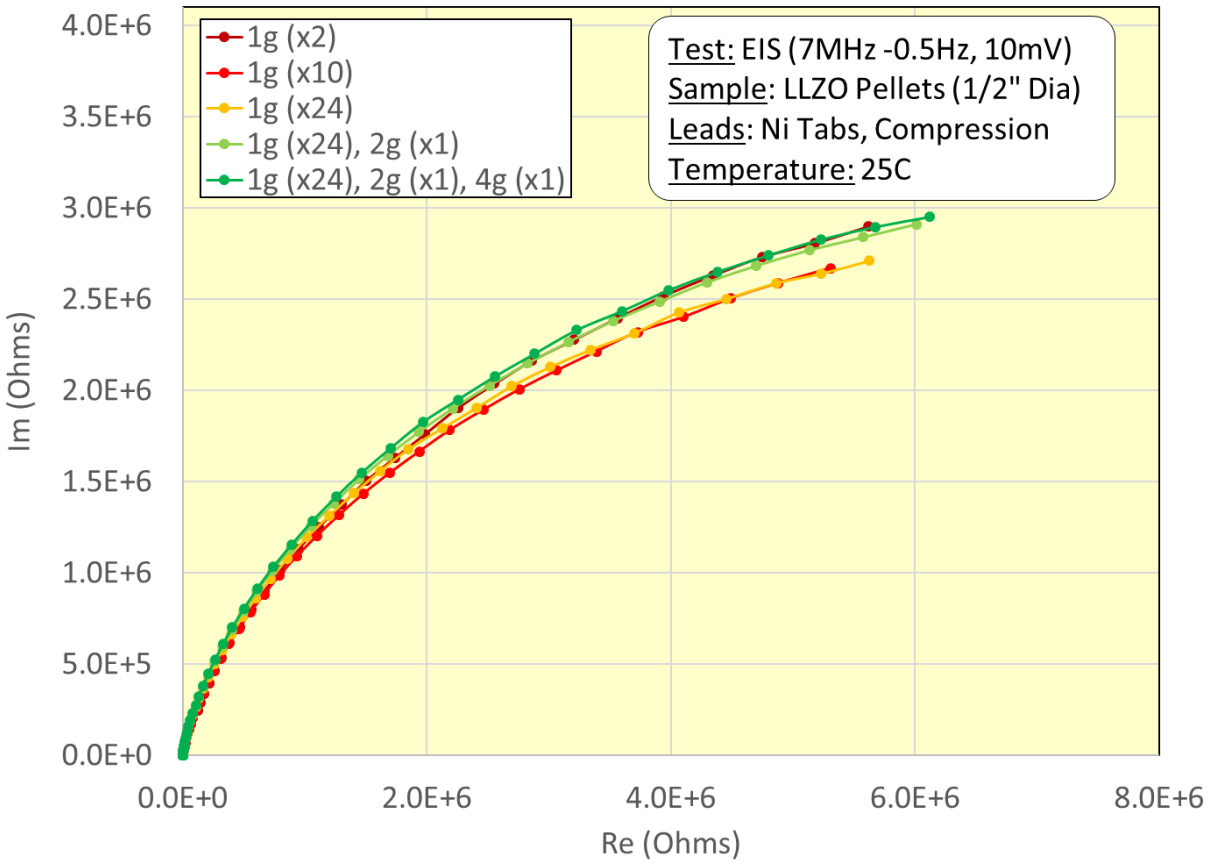

Figure 5.18: Electrochemical Impedance Spectroscopy of LLZO Pellets during Vibration testing using a modified GTR Test Pattern

Each of the five individual EIS curves was then analyzed and the ohmic resistance for each solid state electrolyte connection calculated (see **Figure 5.19**). Following a slight drop in resistance as the vibration test progressed, the ohmic and charge transfer (**Figure 5.18**) resistances were stable and unaffected by the increasing amounts of mechanical vibration [150]. These stable resistances indicate that these solid state electrolyte disks were able to survive a basic regulatory vibration test, as well as an increase of x2 and x4 acceleration severity for a short period of time. In vehicle crash events it is possible to reach acceleration values of 200-400 m/s^2, so future

mechanical stability testing of solid state electrolyte materials may focus on mechanical shock testing, as opposed to vibration stability.

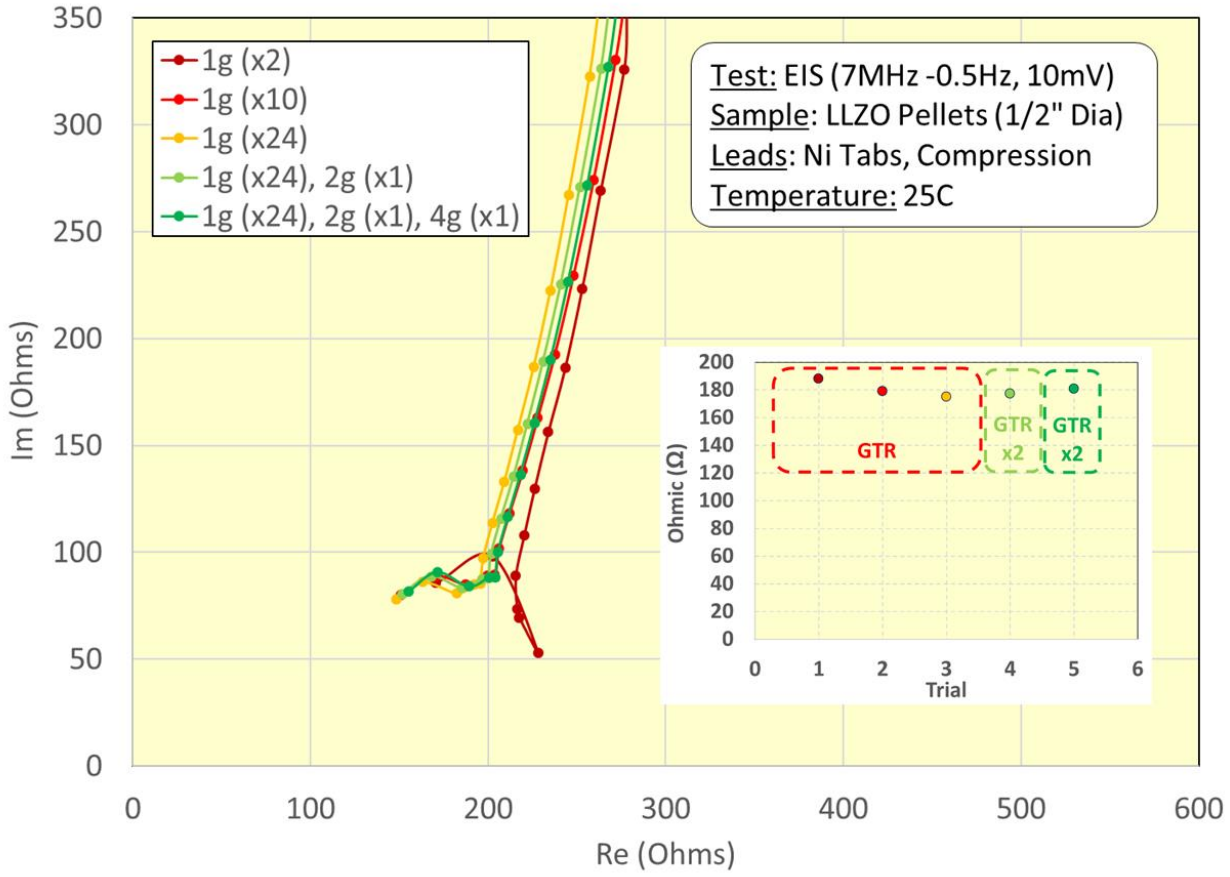

Figure 5.19: EIS plot of LLZO solid electrolyte samples following various GTR vibration sub cycles.

The thickness of the LLZO samples tested ranged between 0.6-0.8mm, which is approximately one order of magnitude thicker than an energy efficient LMSSB design would require. This sample thickness and geometry was set by the constraints of the LLZO synthesize and the sample preparation technique used, rather than an ideal case. Nevertheless we feel these samples were able to serve as proof of concepts and aid the development of a test and evaluation procedure. While it was promising that no sample fractured and that all measured EIS charge-

transfer and ohmic resistances were unaffected by the vibration testing used, further work will be needed to understand the likely response of LMSSB to vibration. As solid state electrolyte samples become thinner and full cell designs incorporating these materials become more mature, the vibration results of such tests will become more meaningful to the development of specific LMSSB products.

5.3 Conclusions

LMSSB may be able to significantly improve upon the specific energy and energy density of traditional LIBs. As an additional benefit, the replacement of the inorganic flammable solvent based liquid electrolyte is touted as giving this battery type a safety advantage in addition to improved energy. However, during our study we were able to perform a fault tree analysis (FTA) which identified several new LMSSB specific safety and quality related failure mechanisms not present in LIBs which warrant further research.

During our research we prioritized three of these faults, water exposure, air exposure and vibration as they applied broadly to the field of potential next generation solid state electrolyte materials options. By performing a range of lithium water exposure experiments we were able to confirm the theoretical heat generation mechanism. Additionally we studied how the electrode sizing of an actual battery may strongly limit the availability of lithium which is free to react with water in the case of a cell breach. We were also able to demonstrate the proof of concept of using existing wave-scan paint appearance tools to quantify the surface quality of lithium foil. Additionally, LLZO solid state electrolyte disks were shown to be able to survive an international regulatory vibration test and a more severe modified test pattern. Although the removal of the LIB flammable electrolyte in place of a solid electrolyte in the LMSSB may lead to a noticeable

improvement in safety, we have identified several open areas of research regarding the ultimate safety performance of lithium metal containing cells.

5.4 Acknowledgements

The Ford-University Michigan Alliance program (Grant # UM0163) funding support is acknowledged. Thanks are given to Samir Tawfik for experimental support and Kent Snyder for helpful conversations.

Chapter 6

Conclusions and Future Research

6.1 Summary

Recent progress in the development of solid state electrolytes has renewed the possibility of rechargeable lithium metal-based batteries [31, 32]. The significant energy density benefit provided by lithium metal has historically been limited by its tendency to form dendrites, inhibiting its life and safety prospects [1, 33, 34]. As the leading candidate for the beyond lithium on (BLI) battery type, the lithium metal solid state battery (LMSSB) has begun to attract significant research attention. Recent research has shown that shortcomings exist in the mechanical understanding of lithium metal. This is clearly evidenced by reports of "soft" (E_{Li} = 7.8 GPa) [42] lithium metal penetrating [118] relatively stiff solid state electrolytes (E_{LLZO} = 150 GPa, E_{LPS} = 13 GPa) [118, 119], despite mechanical model predictions excluding this as a possible scenario [64, 65]. Determining the fundamental mechanical properties of lithium and the study of its safety implications in general in the LMSSB system was the central focus of this dissertation.

6.1.1 Mechanical Properties of Lithium Metal

This research seeks to improve the understanding of the fundamental mechanical properties of lithium using two types of techniques, non-destructive acoustic resonance and uniaxial stress-strain deformation. In this study, two independent elastic constants of lithium were measured on the same sample for the first time, allowing explicit determination of all four elastic constants [42]. This complete set of elastic constants was measured by a pulse echo acoustic technique and will

particularly augment the quality of lithium mechanical models. Also in this study, the elastic, plastic and visco-elastic behavior of bulk lithium under ASTM test conditions was measured. These properties were studied under uniaxial stress-strain deformation in tension and compression and performed on a range of bulk lithium samples.

Furthermore this study was also extended to explore LMSSB application specific sensitivity factors, specifically aspect ratio, temperature and strain rate. As this study examined the impact of aspect ratios, temperatures and strain rates likely in a LMSSB, the mechanical behavior was observed to change dramatically. Depending on the test conditions, the yield strength of lithium was found to vary by approximately one order of magnitude (0.21 – 1.86 MPa) in testing [98].

The observed behavior aligned well with the hydrostatic pinning model (see **Figure 3.5** and **Figure 3.11**) previously seen in copper [42, 98, 99]. The flow stress of lithium was measured to increase as the aspect ratio decreased (**Figure 4.2**, **Figure 4.10** and **Figure 4.11**), the temperature decreased (see **Figure 4.3** and **Figure 4.5**) and the strain rate increased (see **Figure 4.6** and **Figure 4.7**). The direction of these trends is consistent with hydrostatic pinning model which as shown in **Figure 3.5**, accounts for the increase in the total flow stress as a result of regions of limited deformation due to friction forces in pinned material adjacent to the platen. The impact of the sensitivity factors studied, aspect ratio, temperature and strain rate, on the size of the pinned regions is summarized in **Figure 4.12**.

6.1.2 Safety Properties of Lithium Metal

The transition from aqueous based battery chemistry such as lead acid and nickel metal hydride to the inorganic chemistries of LIBs significantly raised energy density as well as introduced new safety concerns [33, 34]. As research in the development of LMSSB to potentially

supplant LIBs, it is important that safety not be taken for granted. The holistic, top-down FTA of safety in LMSSB identified the reactivity of lithium and the brittleness of solid state electrolytes as the two main concerns.

To achieve 500 kilometers of range, a LMSSB powered EV needs approximately 7 kilograms of lithium, which contains a heat content equivalent to 4.6 L of gasoline (see **Figure 1.7**) [150]. Our study confirmed that the water reaction with lithium is exothermic (see **Figure 5.7**) and results in hydrogen gas. It also showed that in the size domains relevant to LMSSB, this gas generation and the formation of precipitates (see **Figure 5.12**) led to a reduced reaction rate (see **Figure 5.8** and **Figure 5.11**). As a result, only a small fraction of the lithium in a LMSSB may be able to react with water, even under the worst case of complete water immersion. This result will have significant implications for the design of LMSSB vehicles.

The FTA also identified the reactivity of lithium metal to moist air as an area for concern and this was determined to take the form of a durability/quality issue as opposed to a safety issue given the limited amount of heat generated. To quantify the extent of lithium surface reaction a proof of concept repurposing of an existing automotive paint surface tool was performed. Additionally, our initial vibration studies on LLZO showed no significant damage to the pellet integrity, as measured by an optical appraisal and in-situ EIS measurements, after more than 3 hours of automotive vibration testing.

6.2 Future Research

6.2.1 Assessment of LIB EV Cell Technology

Future research into the properties of lithium metal for solid state batteries should be motivated by an assessment of the technological needs of LMSSB to supplant LIB in the automotive application. To perform a holistic approach of the challenges facing lithium metal in

LMSSB, the scale of the gap of 7 key performance features necessary of all automotive batteries is instructive. The assessed performance of a range of LIB EV cell technology in 2021 against the USABC EV performance requirements is shown in **Figure 6.1** [27].

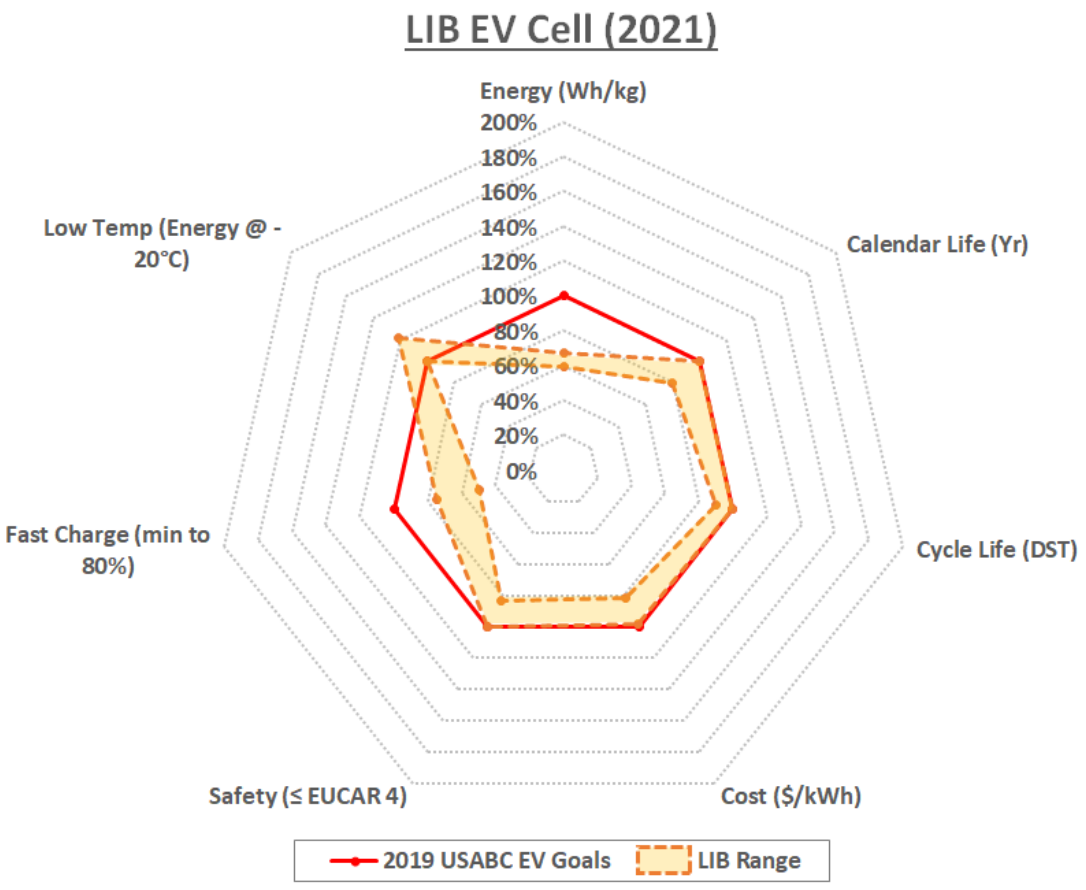

Figure 6.1: LIB EV Cell Performance in 2021 against the 2019 USABC EV Battery Goals [27]

A review of **Figure 6.1** shows that the main deficit of LIB technology at the present time is specific energy (Wh/kg). As was shown in **Figure 1.5**, the historical rate of LIB energy improvement has been dramatic but slowing, raising questions about its long term viability to meet automotive needs. On the other hand, LIB technology has proven itself capable of meeting the

calendar and cycle life requirements of transportation, albeit with advanced thermal and electrical controls technology. Additionally, significant materials and mechanical, electrical and thermal engineering innovations at the cell, pack and vehicle level in the area of safety have ameliorated the inherent energetic nature of LIB cells under most use and abuse conditions. The ability to fast charge is perhaps the most recent automotive requirement and as such it is the second greatest deficit of LIB performance given this performance attributes comparatively shorter R&D time. Achieving fast charging by itself is not difficult for LIB cells, but doing so while maintaining equivalent levels of energy, life and cost has proven more difficult. The final highlighted requirement is for 70% of room temperature energy delivery at -20°C, a low temperature requirement which LIB has been able to meet for many years [27].

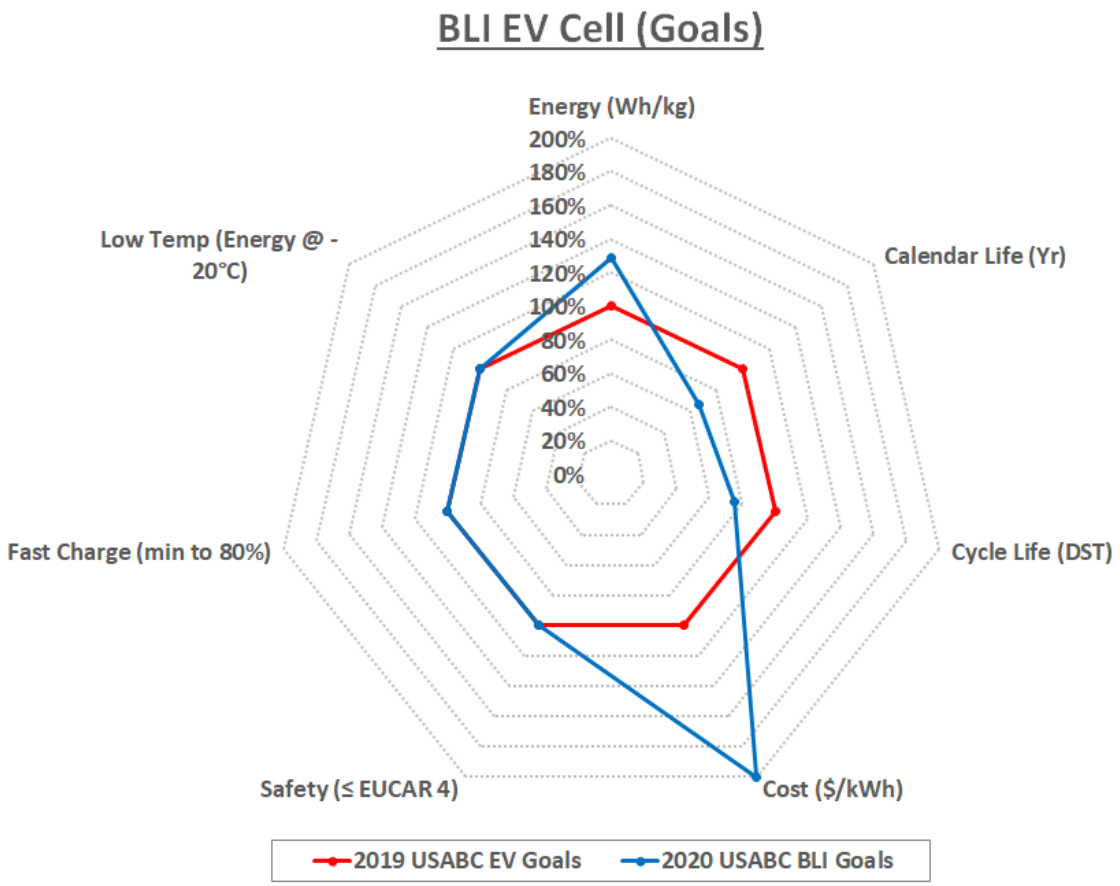

Figure 6.2: 2020 USABC BLI EV Cell Goals compared against the 2019 USABC EV Battery Cell Goals [27, 159]

To guide the development of future lithium metal based cells, the USABC recently issued a new set of performance targets in 2020 for this BLI technology [159]. A comparison between the 2019 USABC EV Cell and the 2020 USABC BLI targets reveals the evolving nature of the automotive application and how it can be tailored to BLI cell technology (see **Figure 6.2**) [27, 159]. The promise of increased energy from BLI cells and the need for continuous performance improvement inherent in the competitive automotive application is seen by an increase in this requirement. The typical expectation of automotive life is reflected in the traditional gas powered emissions useful life definition of 10 years/100,000 by the US Federal Government [160] and 15

years /150,000 miles by US states which have adopted the regulations of the California Air Resource Board (CARB) [161]. The calendar life requirement was reduced from the CARB to the Federal definition and the cycle life scaled down by accounting for the increased energy content of BLI technology in the context of a fixed vehicle lifetime range. The cell level cost goal was halved to $50/kWh from the EV goal, primarily due to the improving nature of LIB technology and the rising size of EV battery packs. This cost reduction will promulgate to the next revision of the USABC EV goals and highlights a future challenge for all BLI technology to compete with LIBs. The three remaining requirements, safety, fast charge and low temperature energy performance were all left the same for the BLI goals as in the case of the EV goals.

6.2.2 Future Challenges and Opportunities for LMSSB

The future challenges and opportunities for LMSSB in automotive applications should be framed against the context of existing automotive requirements. In **Figure 6.3** we see a range of future potential LMSSB EV cell capability plotted against the USABC EV and BLI goals [27, 159].

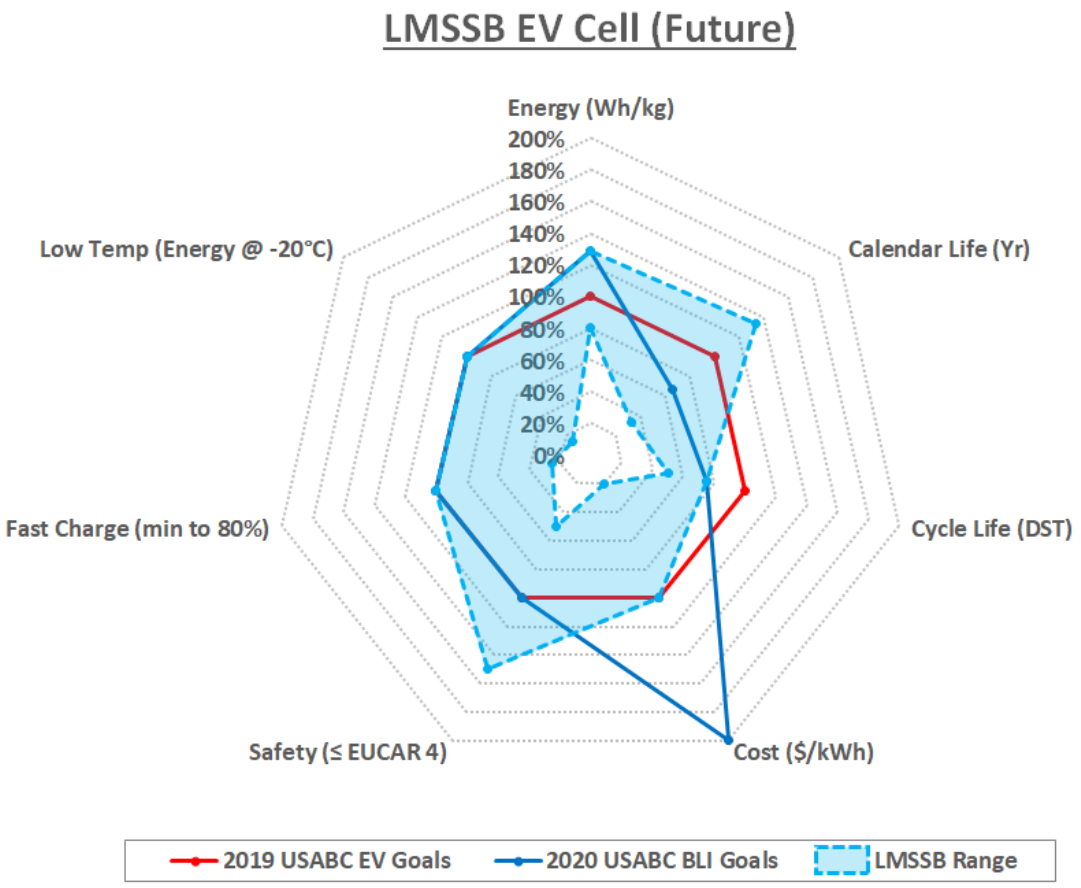

Figure 6.3: LMSSB EV Cell Future Performance Potential compared against the 2019 USABC EV Cell and 2020 USABC BLI EV Cell Goals [27, 159]

6.2.2.1 Energy

The potential for high energy inherent in replacing carbon anodes with lithium metal in the traditional LIB system is the primary motivation for the development of the LMSSB cell type and this research dissertation. The performance estimates of future designs have ranged from 350 to 450 Wh/kg [35, 36] at the cell beginning of life. Typically LIB cells assume 20% capacity fade signifies the end of life, if a LMSSB cell could improve that assumed degradation the energy margin over LIB technology could be improved further when considering end of life needs.

Key areas for future improvement in LMSSB related to lithium metal revolve around reducing the amount of excess lithium needed and the compressive load required. The optimization of excess lithium from the 100 to 50% seen in research cells to values closer to 10% or less is required to achieve high cell level energy values. Additionally, LMSSB designs require significant compression pressures (on the order of MPas) to maintain low interfacial resistance. Maintaining compression is a common battery requirement, prevalent in NiMH and LIB technology, however, the amount of pressure needed is typically an order of magnitude lower. Although it is not difficult to design a battery pack with such high compressive loads, this need for extra structural load bearing hardware will reduce the weight and volume advantage of the LMSSB technology. This study has shown that the yield strength of lithium increases with decreasing aspect ratio (see **Figure 4.10** and **Figure 4.11**), potentially reaching values of 14 to 20 MPa in likely LMSSB electrode sizes (see Section 4.2.5) [98] in alignment with other studies [136, 162]. Accordingly, innovative new mechanical concepts to overcome the yield strength of lithium to enable good bonding of the cathode/electrolyte/anode layers and thereby maintaining low interfacial resistance are needed.

6.2.2.2 Calendar Life

LMSSB will be required to perform for 10 [159] to 15 [27] years to meet automotive industry requirements, while allowing for only 20% capacity lose. In this study we measured the visco-elastic behavior in compression (see **Figure 3.9**), establishing the strain rate decay behavior in lithium as a function of time and pressure (see **Figure 3.10**). The time periods studied to date were chosen to match those of typical charge/discharge patterns, ranging from 12 minutes to 2 hours (see **Table 3.4**). As was described in Section 6.2.1., during these and all compression testing the behavior of lithium was consistent with the hydrostatic pinning model [99]. An extension of

these studies from the hours of testing currently performed to the years required by the application is an important area of future research. As is shown in Figure 3.11, without hydrostatic pressure it is possible for lithium to deform around the separator geometry and potentially short-circuit a cell. Unless the long term behavior of the hydrostatic pinning in lithium is confirmed, the mechanical designers of LMSSB will need to consider alternative confinement strategies for lithium metal electrodes in plane.

Additionally, most solid state electrolyte materials are not stable against lithium with the notable exception of LLZO, and therefore require the application of interface layers [163]. Confirming the effectiveness and durability of these layers at shielding the decomposition of the solid state electrolytes could be the difference between inferior (i.e. 5 years) or superior (i.e. 20 years) calendar performance of LMSSB compared to LIBs.

6.2.2.3 Cycle Life

The work performed to date has contributed to the understanding of the mechanical and safety properties of lithium metal, in particular as they apply to LMSSB predicted to replace LIBs. Recent discoveries of promising solid state electrolyte materials [31, 32] can potentially address the challenges posed by lithium dendrites in limiting battery cycle life [87]. The long term electrochemical cycling stability of lithium in combination with one of these new solid state electrolytes materials should be the basis of future research. To date, limited cycle life performance of small scale, lithium/lithium symmetric cells cycled at steady currents represents the bulk of the published cycling stability literature on solid state electrolytes [36, 164]. Cycling of automotive size (60-100 Ah) full cells using the USABC Dynamic Stress Test (DST) pattern is several years away for even the most advanced cell developer known in 2021.

Due to the increased energy potential in BLI cells, the cycling requirement has been reduced to 750 from 1,000 cycles when comparing the 2019 USABC EV Cell goals to the 2020 USABC BLI Cell goals [27, 159]. When considering the overall vehicle useful life definitions of the Federal and CARB regulations, the USABC EV Cell cycle life goal corresponds to a typical vehicle travel range of 100-150 miles per cycle. Translating the USABC BLI cycle life goal yields a typical vehicle travel range of 133-200 miles per cycle, a modest increase likely to be met by advanced LIB and basic LMSSB technology once it has been qualified for automotive use.

6.2.2.4 Cost

The continuous improvement of LIB cell and pack level cost has been shown in **Figure 1.4** [19, 23]. The significant reduction in the cost of LIB technology has enabled the revision of the USABC target from $100/kWh (EV Cell) [27] to $50/kWh (BLI Cell) [159]. Although the per energy cost of LIBs has dropped noticeably, due to the growing size of EV battery packs, the absolute amount of battery cost still remains high, see Section 1.1.1. It is expected that when the USABC EV goals are revised, their cost targets will match those in the BLI requirements as reason for the drop is market competitive pressures independent of chemistry.

The high cost of lithium foils compared to graphite materials has prompted the research of alternative electrode designs, most prominently so-called lithium free schemes initially proposed in liquid systems [165] and then extended to solid systems [166]. By avoiding the need to manufacture a cell with standalone lithium but rather relying on the cathode and/or electrolyte to provide the metallic lithium in-situ, this technique has the potential to reduce the added cost of lithium metal in both liquid [167] and solid state [166] battery designs.

6.2.2.5 Safety

The safety properties of lithium metal in the context of LMSSB was one of the central themes of this research dissertation. By performing a holistic, FTA analysis of the potential LMSSB cell design we have identified two main categories of hazards unique to LMSSB and distinct to those seen in LIB designs; exposure to the environment and vibration/mechanical shock. Despite these novel hazards, overall LMSSB holds the potential to be a significant safety improvement over LIB as the quantity of hazards detected in our LMSSB FTA (see **Figure 5.1**) [139, 150] was much smaller than that previously found in a LIB FTA [53].

To more directly study the application safety of lithium in the LMSSB, our initial safety study (Chapter 5) should be extended to explore LMSSB specific sensitives as we did (Chapter 4) based on the initial mechanical properties of lithium (Chapter 3). Our research found a strong sensitivity of lithium/water reactivity based on sample thickness in the constrained geometry likely in LMSSB designs. Extending this water exposure study to lithium thicknesses of approximately 50 um would enable a direct assessment of the likely response in the LMSSB application.

This study also investigated the impact of environmental moist air coming into contact with lithium metal and found it be a quality issue rather than a safety challenge. When lithium is exposed to moist air, a two step decomposition mechanism occurs where lithium hydroxide is generated and subsequently reacts with carbon dioxide to form a layer of lithium carbonate on the surface [151]. Due to the self-limiting nature of this reaction, it does not generate enough heat to provide an ignition source. If the resistive coating of lithium carbonate [168] coated a significant fraction of the LMSSB lithium electrode after air exposure, it is possible that resistive heating could create sufficient thermal energy to provide an ignition source. This seems unlikely given

the limited edge plane surface area available to air exposure and the challenges identified in significant water exposure shown in Section 5.2.2.

However another identified potential safety implication of exposure to moist air is the generation of hydrogen sulfide gas from some sulfur based solid electrolytes (see Section 5.2.1.4). Although some studies have been performed on altering the electrolyte material to reduce the quantity of hydrogen sulfide gas [169], more research on this subject is needed given its potential impact on safety [148].

Additionally, this research also found that LLZO was able to undergo an automotive vibration test pattern without fracturing or a rise in internal resistance. Evaluating thinner samples of LLZO (approximately 50 um as well) and extending the test pattern from the vibration (1-8g for minutes) to the mechanical shock region (11-18g for milliseconds) [142] testing would yield insights into the limits of the present safety scheme as has been developed by existing studies of LIB vibration. [170, 171, 172]

6.2.2.6 Fast Charge

During our research in the LMSSB application based sensitives affecting the mechanical performance of lithium metal we explored the impact of strain rate. Our initial study determined the steady state secondary creep strain rate of lithium to be between 3×10^{-4} and 2×10^{-7} s^{-1} in tension depending on the load (see **Figure 3.7**) [42]. At speeds above these strain rate, lithium was able to avoid the visco-elastic region and deform plastically in both tension and compression. Our LMSSB sensitivity mechanical study showed that raising the strain rate further had the effect of doubling the lithium yield strength from approximately 0.7 MPa at 1×10^{-3} s^{-1} to 1.4 MPa at 1 s^{-1} (see **Figure 4.6**) [98].

In the LMSSB system, lithium is both the anode and charge carrier, requiring it to be mechanically stripped and plated with each respective discharge and charge event. As a result it is possible to draw a linear correlation between the average strain rate a lithium electrode would experience and areal current (A/cm^2) required by a LMSSB based battery pack (see **Figure 6.4**) [173]. By overlaying the current demands of various SAE J1772 defined charging power and the discharge power output rating of various EVs, it is possible to contextualize the lithium strain rate [174]. Using the SAE J1772 nomenclature, fast charging to meet the USABC requirements would fit into the DC Charge zone which exists on the strain rate boundary (1 to 3 x 10^{-4} s^{-1}) of visco-elastic and plastic deformation seen in lithium metal.

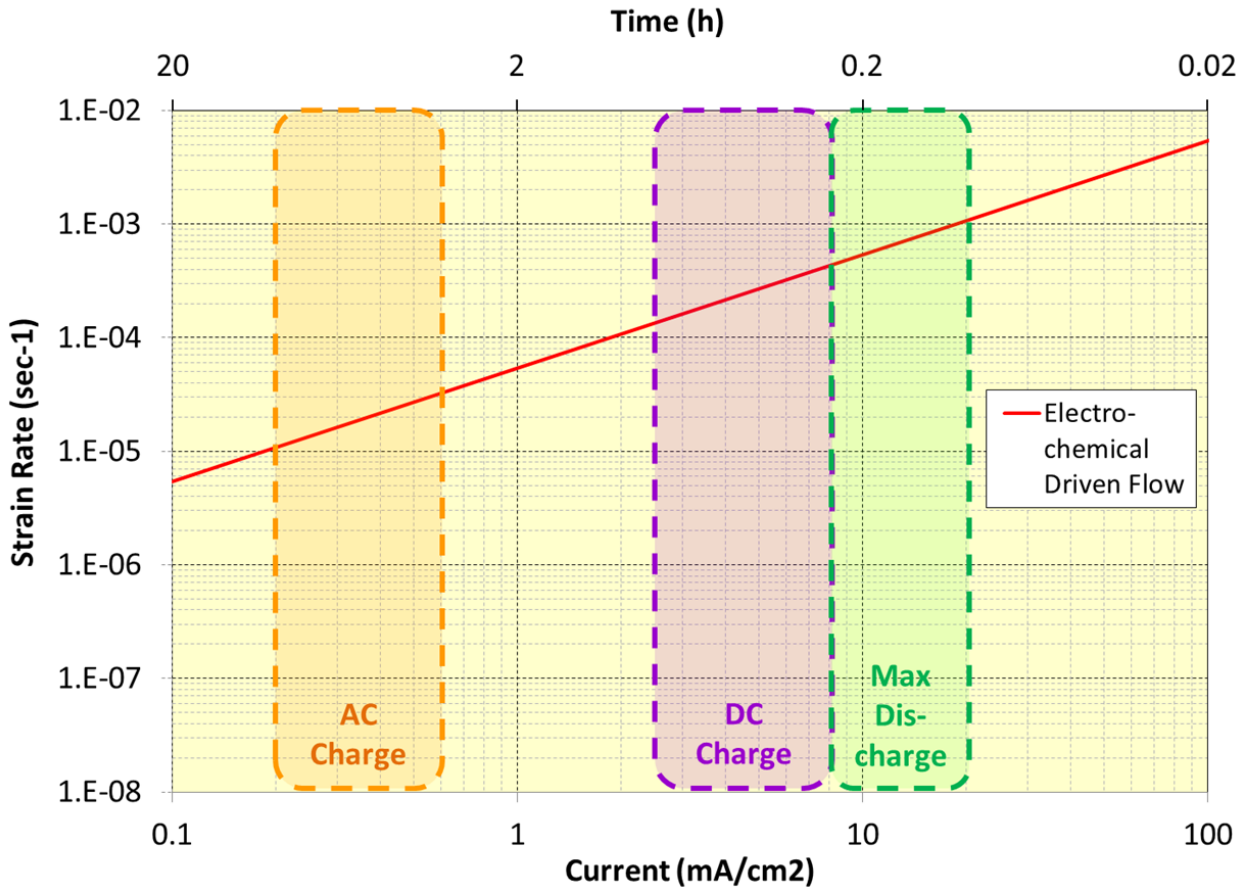

Figure 6.4: Correlation between the mechanical strain rate (s-1) of lithium of stripping (discharge) and plating (charge) in a lithium electrode and the areal current (A/cm^2) of a LMSSB battery pack based vehicle [173]

It is noteworthy that Figure 6.4 plots the average strain rate required to be achieved across an entire battery pack. As a result it very likely that the local strain rates for certain portions of the LMSSB cells which comprise a pack will experience significantly higher strain rates, leading to a corresponding rise in the lithium strain rate as previously shown (see **Figure 4.6**) [98]. The potential impact of strain rate on the likelihood of solid state electrolyte penetration as previously observed should be an area of future research [118].

6.2.2.7 Low Temperature

EV batteries are sized for energy content by range & temperature requirements, but power capacity is also strongly limited by low temperatures such as -20°C [15, 27, 159]. EVs do not have a heat engine on board to supplement power as hybrid electric vehicles do and so they must rely on the battery for startup and power. It is arguable that the customer who has a vehicle at such cold temperatures is the one who needs their vehicle to reliably work as expected the most. LIB technology has been able to meet the low temperature performance requirements of automotive applications for many years, whereas most proposed LMSSB designs prefer elevated temperatures in the range of 45 to 60°C. As a result, it is also arguable that given the large impact of temperature on the achievable current densities seen in solid state electrolytes [164], this automotive requirement maybe the most difficult for LMSSBs to meet.

Decreasing the temperature of a true solid state conductor is expected to lead to decreasing resistance. The observed opposite trend in solid state electrolytes highlights the interface as opposed to the bulk as the root cause of the rate limiting region. As a result research efforts to improve the low temperature performance of LMSSB need to focus on improvements at interface coatings. Also, given that the mechanical yield strength of lithium metal is predicted to be noticeably stronger at lower temperature (see **Figure 4.5**) [98], LMSSB designers must also ensure that they use solid state electrolytes of sufficiently high resistance to penetration by lithium dendrites.

Appendix

The physical relationships referencing the mechanical properties of lithium as shown in reference 64 are reproduced for reference below. [64] Monroe, C., Newman J., "The impact of elastic deformation on deposition kinetics at lithium/polymer interfaces." Journal of the Electrochemical Society, 152 (2005), A396–A404.

In an equilibrated elastic solid, the total stress, $\underline{\underline{\sigma}}$, can be used to describe the steady-state equation of motion as:

$$-\overline{\nabla} \cdot \underline{\underline{\sigma}} = 0 \qquad \text{A.1}$$

The total stress, $\underline{\underline{\sigma}}$, is in turn related to the deformation stress and gage pressure, p, by equation A.2, where $\underline{\underline{\tau}}_d$ is the deformation stress tensor, N/m^2, p is the gage pressure, N/m2 and $\underline{\underline{I}}$ is the identity tensor.

$$\underline{\underline{\sigma}} = \underline{\underline{\tau}}_d + p\underline{\underline{I}} \qquad \text{A.2}$$

Total stress of an isotropic elastic material given by the Navier-Poisson constitutive law, wherein the stress $\underline{\underline{\sigma}}$ is described by equation A.3, where tr( ) denotes the trace of a tensor, v is the Poisson's ratio and G the shear modulus.

$$\underline{\underline{\sigma}} = -\frac{2vG}{1-2v}\, tr\left(\underline{\underline{\varepsilon}}\right) - 2G\,\underline{\underline{\varepsilon}} \qquad \text{A.3}$$

When only considering linear elasticity, deformations can be considered small enough such that the strain can be described by the gradients of the displacement vector from an original undeformed configuration for reference, **u**, by equation A.4 where the superscript T denotes the transpose of a tensor.

$$\underline{\underline{\varepsilon}} = \frac{1}{2}\left[\overline{\nabla}\mathbf{u} + \left(\overline{\nabla}\mathbf{u}\right)^{\mathrm{T}}\right] \qquad \text{A.4}$$

Equations A.1, A.2, A.3 and A.4 summarize the equations governing an isotropic linear elastic solid. The Poisson's ratio used in equation A.3 can be expressed in terms of the shear modulus, G, and the bulk modulus, K. This new relation can be inserted into equation A.1 to yield,

$$0 = \overline{\nabla}\cdot\left(\overline{\nabla}\mathbf{u}\right) + \frac{1}{1-2v}\overline{\nabla}\left(\overline{\nabla}\cdot\mathbf{u}\right) \qquad \text{A.5}$$

By solving equation A.5 the system impact of periodic interfacial disturbances can be determined. To accomplish this boundary conditions are created in a two dimensional system (x-

and z- directions) with the electrode surface at z = 0 and the lithium and solid state electrolyte extending infinitely far away, as a result,

$$u_x(x, z \to \pm\infty) = 0 \quad \text{A.6}$$

$$u_z(x, z \to \pm\infty) = 0 \quad \text{A.7}$$

When $z \geq 0$, the material behaves as the solid state electrolyte for the shear modulus and Poisson's ratio (i.e. G^{sse} and v^{sse}) and for $z \leq 0$, it behaves as lithium (i.e. G^{Li} and v^{Li}). At the electrode surface, i.e. z = 0, there is a periodic deformation with amplitude A and frequency ω, such that

$$u_z(x, 0) = A\cos(\omega x) \quad \text{A.8}$$

Together equations A.6, A.7 and A.8 provide the boundary conditions to solve equation A.5 to yield the following displacement functions.

$$u_x^{sse} = \left[A - \frac{(3 - 4v^{sse})}{\omega} B + Bz\right] \sin(\omega x) e^{-\omega z} \quad \text{A.9}$$

$$u_z^{sse} = (A + Bz)\cos(\omega x) e^{-\omega z} \quad \text{A.10}$$

$$u_x^{Li} = \left\{A - \frac{(3 - 4v^{sse})}{\omega} B + \left[\frac{2\omega}{(3 - 4v^{Li})} A - \frac{(3 - 4v^{sse})}{(3 - 4v^{Li})} B\right] z\right\} \sin(\omega x) e^{\omega z} \quad \text{A.11}$$

$$u_z^{Li} = \left\{A - \left[\frac{2\omega}{(3 - 4v^{Li})} B - \frac{(3 - 4v^{sse})}{(3 - 4v^{Li})} B\right] z\right\} \cos(\omega x)\ e^{\omega z} \quad \text{A.12}$$

Where B is an arbitrary constant which can be solved by satisfying the boundary conditions using equations A2., A.3 and A.4 to calculate the displacement shear stress, τ, on either side of the interface boundary defined by z = 0. This calculation yields A.13, A.14 and A.15 at the surface of the solid state electrolyte and A.16, A.17 and A.18 at the surface of the lithium.

$$\tau_{xx}^{sse}(x,0) = 2G^{sse}[-A\omega + 2(1-v^{sse})B]\cos(\omega x) \quad \text{A.13}$$

$$\tau_{xz}^{sse}(x,0) = \tau_{zx}^{sse}(x,0) = 2G^{sse}[A\omega - 2(1-v^{sse})B]\sin(\omega x) \quad \text{A.14}$$

$$\tau_{zz}^{sse}(x,0) = 2G^{sse}[A\omega - 2(1-v^{sse})B]\cos(\omega x) \quad \text{A.15}$$

$$\tau_{xx}^{Li}(x,0) = \frac{2G^{Li}}{(3-4v^{Li})} \times [-A\omega + 2\left(1-v^{Li}\right)(3-4v^{sse})B]\cos(\omega x) \quad \text{A.16}$$

$$\tau_{xz}^{Li}(x,0) = \tau_{zx}^{Li}(x,0) \quad \text{A.17}$$

$$= \frac{2G^{Li}}{(3-4v^{Li})} \times \left[-A\omega + 2\left(1-v^{Li}\right)(3-4v^{sse})B\right]\sin(\omega x)$$

$$\tau_{zz}^{Li}(x,0) = \frac{2G^{Li}}{(3-4v^{Li})}\left[A\omega - 2\left(1-v^{Li}\right)(3-4v^{sse})B\right]\cos(\omega x) \quad \text{A.18}$$

By using the defined boundary conditions, it is possible to derive B as

$$B = A\frac{\omega\left[G^{sse}\left(3-4v^{Li}\right)+G^{Li}\right]}{2[G^{sse}(3-4v^{Li})(1-v^{sse})+G^{Li}(3-4v^{sse})(1-v^{Li})]} \quad \text{A.19}$$

Bibliography

[1] Blomgren, G. E., "The Development and Future of Lithium Ion Batteries." *J. Electrochemical Society*, 164 (1) (**2017**), A5019-A5025.

[2] Goodenough, J. B., Park, K., "The Li-Ion Rechargeable Battery: A Perspective." Journal of the American Chemical Society 135, 4 (2013) 1167-1176.

[3] The Nobel Prize in Chemistry 2019. "They developed the world's most powerful battery." The Royal Swedish Academy of Sciences. October 2019. Retrieved from https://www.nobelprize.org/uploads/2019/10/popular-chemistryprize2019.pdf (accessed February 12, 2021).

[4] Xiao Q, Li B, Dai F, Yang L, Cai M. Application of Lithium Ion Battery for Vehicle Electrification. Electrochemical Energy: Advanced Materials and Technologies. 2015.

[5] Corrigan D., Masias A., Batteries for electric and hybrid vehicles. Linden's handbook of batteries, 4th edn. McGraw Hill, New York. 2011.

[6] Luo, X., Wang, J., Dooner, M., Clarke, J., "Overview of current development in electrical energy storage technologies and the application potential in power system operation." *Applied Energy*, 137 (**2015**) 511-536.

[7] Dunn, B., Kamath, H., Tarascon, J.M., "Electrical Energy Storage for the Grid: A Battery of Choices." Science 334, 6058 (2011) 928-935.

[8] Hesse, H. C., Schimpe, M., Kucevic, Jossen, A., "Lithium-Ion Battery Storage for the Grid – A Review of Stationary Battery Storage System Design Tailored for Applications in Modern Power Grids." Energies 10, 2107 (2017) 1-42.

[9] Zubi, G., Dufo-Lopez, R., Carvalho, M., Pasaogul, G., "The lithium-ion battery: State of the art and future perspectives." *Renewable and Sustainable Energy Review*, 89 (**2018**) 292-308.

[10] National Oceanographic and Atmospheric Administration, Climate.gov, Climate Change: Atmospheric Carbon Dioxide. August 14, 2020. Retrieved from https://www.climate.gov/news-features/understanding-climate/climate-change-atmospheric-carbon-dioxide (accessed February 13, 2021).

[11] Ackerman, F., Stanton, E. A., "What We'll Pay if Global Warming Continues Unchecked." Natural Resources Defense Council, May 2008. Retrieved from https://www.nrdc.org/sites/default/files/cost.pdf (accessed February 13, 2021).

[12] Davis, S. C., Boundy, R. G., Transportation Energy Data Book, edition 38.2, ORNL-5198, Oak Ridge National Laboratory, Knoxville, TN 2020. Retrieved from https://tedb.ornl.gov/wp-content/uploads/2020/02/TEDB_Ed_38.pdf (accessed February 13, 2021).

[13] Lawrence Livermore National Laboratory (LLNL). Energy Flow Charts, "2019: United-States." March 2020. Retrieved from https://flowcharts.llnl.gov/content/assets/images/charts/Energy/Energy_2019_United-States.png (Accessed February 2, 2021).

[14] Kim, H. C., Wallington, T. J., Arsenault, R., Bae, C., Suckwon, A., Lee, J., "Cradle-to-Gate Emissions from a Commercial Electric Vehicle Li-Ion Battery: A Comparative Analysis." Environmental Science & Technology, 50, 14 (2016), 7715-7722. https://doi.org/10.1021/acs.est.6b00830

[15] Wu, D., Guo, F., Field, F. R., De Kleine, R. D., Kim, H. C., Wallington, T. J., Kirchain, R. E., "Regional Heterogeneity in the Emissions Benefits of Electrified and Lightweighted Light-Duty Vehicles." Environmental Science & Technology, 53, 18 (2019), 10560-10570. https://doi.org/10.1021/acs.est.9b00648

[16] Dunn, J. B., Gaines, L., Kelly, J. C., James, C., Gallagher, K. G., "The significance of Li-ion batteries in electric vehicle life-cycle energy and emissions and recycling's role in its reduction." Energy & Environmental Science 8 (2015), 158-168.

[17] Sivak, M., Schoettle, B., "Relative Costs of Driving Electric and Gasoline Vehicles in the Individual U.S. States." The University of Michigan Sustainable Worldwide Transportation, Report # SWT-2018-1 (2018), 1-11. Retrieved from http://umich.edu/~umtriswt/PDF/SWT-2018-1.pdf (accessed February 2, 2021).

[18] The Official U.S. Government Source for Fuel Economy Information, U.S. Environmental Protection Agency. Retrieved from www.fueleconomy.gov (accessed Jan 6, 2021).

[19] Masias, A., Marcicki, J., Paxton, W., "Opportunities and Challenges of Lithium Ion Batteries in Automotive Applications." *ACS Energy Letters*, 6 (**2021**), 621-630. https://dx.doi.org/10.1021/acsenergylett.0c02584

[20] United States Code of Federal Regulations, Title 40, Chapter 1, Subchapter C, Part 86 – Control of Emissions from New and In-use Highway Vehicles and Engines. Retrieved from http://www.ecfr.gov/cgi-bin/text-idx?SID=f4998116259c3d616115baa40e23648a&mc=true&node=pt40.19.86&rgn=div5#sp40.19.86.b, (accessed February 13, 2021).

[21] Robertson, D. C., Christophersen, J. P., Bennet, T., Walker, L. K., Wang, F., Liu, S., Fan, B., Bloom, I., "A comparison of battery testing protocols: Those used by the U.S. advanced battery consortium and those used in China." *Journal of Power Sources* 306 (**2016**) 268-273.

[22] Belt, J., Utgikar, V., Bloom, I., "Calendar and PHEV cycle life aging of high-energy, lithium-ion cells containing blended spinel and layered-oxide cathodes." *Journal of Power Sources* 196 (**2011**) 10213-10221.

[23] Frith, J. 2020 Lithium Ion Battery Price Survey; Bloomberg New Energy Finance, New York, 2020. Retrieved from https://about.bnef.com/blog/battery-pack-prices-cited-below-100-kwh-for-the-first-time-in-2020-while-market-average-sits-at-137-kwh/ (accessed February 13, 2021).

[24] Argonne National Lab, Energy Systems Division, GREET Model, Retrieved from https://greet.es.anl.gov/ (accessed February 13, 2021.)

[25] Winjobi, Q., Dai, Q., Kelly, J., "Updte of Bill-of-Materials and Cathode chemistry addition for Lithium-ion Batteries in the GREET Model." October 1, 2020. Retrieved from https://greet.es.anl.gov/publication-bom_lib_2020 (accessed February 13, 2021).

[26] Kelly, J. C., Sullivan, J. L., Burnham, A., Elgowainy, A., "Impacts of Vehicle Weight Reduction via Material Substitution on Life-Cycle Greenhouse Gas Emissions." *Environmental Science & Technology* 49 (**2015**) 12535-12542.

[27] United States Advanced Battery Consortium (2018) USABC Goals for Advanced Batteries for EVS—CY 2020 Commercialization. Accessed 23 July 2018. Retrieved from http://www.uscar.org/commands/files_download.php?files_id=364

[28] European Council for Automotive R&D (EUCAR). Battery requirements for future automotive applications, July 2019. Retrieved from https://eucar.be/wp-content/uploads/2019/08/20190710-EGBEV-FCEV-Battery-requirements-FINAL.pdf (accessed February 13, 2021).

[29] Masias, A. (**2018**). "Lithium Ion Battery Design for Transportation." In G. Pistoia & B. Liaw (Eds.), Behavior of Lithium-Ion Batteries in Electric Vehicles: Battery Health, Performance, Safety, and Cost (pp. 1-34). Springer International Publishing.

[30] Christman, J., "The Case of the Burning Laptops." *Journal of Case Studies*, 30, 1 (**2012**), 88-97.

[31] Murugan, R., Thangadurai, V., Weppner, W., "Fast Lithium Ion Conduction in Garnet-Type Li7La3Zr2O12." *Angewandte Chemie Interational Edition*, 46 (41) (**2007**) 7778-7781.

[32] Kamaya, N., Homma, K., Yamakawa, Y., Hirayama, M., Kanno, R., Yonemura, M., Kamiyama, T., Kato, Y., Hama, S., Kawamoto, K., Mitsui, A., "A lithium superionic conductor". Nature. Materials 10, 682–686 (2011)

[33] Winter, M., Barnett, B., Xu, K., "Before Li Ion Batteries." *Chemical Reviews*, 118 (**2018**) 11433-11456.

[34] Placke, T., Kloepsch, R., Duhnen, S., Winter, M., "Lithium ion, lithium metal, and alternative rechargeable battery technologies: the odyssey for high energy density." *Journal of Solid State Electrochemistry*, 21 (**2017**) 1939-1964.

[35] McCloskey, B. D., "Status and challenges in enabling the lithium metal electrode for high-energy and low-cost rechargeable batteries"; *J Phys. Chem. Lett.,* Vol. 6, 22 (**2015**) 4581-4588.

[36] Albertus, P., Babinec, S., Litzelman, S., Newman, A., "Status and challenges in enabling the lithium metal electrode for high-energy and low-cost rechargeable batteries"; *Nature Energy*, Vol 3 (**2018**) 16-21.

[37] Prasad, N. E., Gokhale, A. A., Wanhill, R. J. H. (eds), "Aluminum-Lithium Alloys: Processing, Properties and Applications." Elsevier/Butterworth-Heinemann, Oxford, UK (2014).

[38] Mallick, K. K., Holland, D., "Strengthening of container glasses by ion-exchange dip coating." Journal of Non-Crystalline Solids, 351 (30-32) (2005) 2524-2536.

[39] Zapała-Sławeta, J., Owsiak, Z., "The role of lithium compounds in mitigating alkali-gravel aggregate reaction." Construction and Building Materials, 115 (2016) 299-303.

[40] Delgado, M.A., Valencia, C., Sanchez, M. C., Franco, J. M., Gallegos, C., "Thermorheological behavior of a lithium lubricating grease." *Tribology Letters*, 23 (**2006**) 47-54.

[41] Konings, R., Cordfunke, E., Ouweltjies, W., "The Standard Enthalpies of Formation of Hydroxides III. LiOH." *J. Chemical Thermodynamics*, 21 (4) (**1989**), 415-417.

[42] Masias, A., Felten, N, Garcia-Mendez, R., Wolfenstine, J., Sakamoto, J., "Elastic, plastic and creep mechanical properties of lithium metal." *J. Material. Science*, 54(3) (**2019**), 2585-2600.

[43] W.F. Hosford and R.M. Caddell: Metal Forming: Mechanics and Metallurgy (Cambridge University Press, Cambridge, 1993).

[44] Brick, R. M., Structure and properties of engineering materials, 4th Edition. McGraw-Hill, New York (1977).

[45] St-Pierre, C., Gauthier, T., Hamel, M., Leclair, M., Parent, M., Davis, M. S., "AVESTOR/spl trade/ lithium-metal-polymer batteries: conclusions to be drawn from field trial results," The 25th International Telecommunications Energy Conference, 2003. INTELEC '03., Yokohama, Japan, 2003, pp. 51-58.

[46] Vigerstol, O. K., "A review of the suitability of lithium battery technology in ict energy infrastructure," 2017 IEEE International Telecommunications Energy Conference (INTELEC), Broadbeach, QLD, 2017, pp. 254-261, doi: 10.1109/INTLEC.2017.8214144.

[47] Sahraei, E., Meier, J., Wierzbicki, T., "Characterizing and modeling mechanical properties and onset of short circuit for three types of lithium-ion pouch cells." *J. Power Sources*, 247, (**2014**), 503-516.

[48] Sahraei, E., Hill, R., Wierzbicki, T., "Calibration and finite element simulation of pouch lithium-ion batteries for mechanical integrity." *J. Power Sources*, 201, (**2012**), 307-321.

[49] Liu, X., Stoliarov, S., Denlinger, M., Masias, A., Snyder, K., "Comprehensive calorimetry of the thermally-induced failure of a lithium ion battery." *J. Power Sources*, 280, (**2015**), 516-525.

[50] Liu, X., Wu, Z., Stoliarov, S., Denlinger, M., Masias, A., Snyder, K., "A thermos-kinetic model of thermally-induced failure of a lithium ion battery: development, validation and application." *J. Electrochemical Society*, 165 (11) (**2018**), A2909.

[51] Xia, B., Chen, Z., Mi, C., Robert, B., "External Short Circuit Fault Diagnosis for Lithium-Ion Batteries." 2014 IEEE Transportation Electrification Conference, Dearborn, MI, June 15-18, 2014.

[52] Xia, B., Mi, C., Chen, Z. Robert, B. "Multiple Cell Lithium-Ion Battery System Electric Fault Online Diagnostics." 2015 IEEE Transportation Electrification Conference and Expo, Dearborn, MI June 14-17, 2015.

[53] Masias, A., "Ford Safety Performance of Rechargeable Energy Storage Systems (RESS)." Report # DOT HS 812 756, (2019, July), Washington, DC: National Highway Traffic Safety Administration (NHTSA). https://rosap.ntl.bts.gov/view/dot/41840

[54] Deng, J., Bae, C., Marcicki, J., Masias, A., Miller, T., "Safety modeling and testing of lithium-ion batteries in electrified vehicles." *Nature Energy*, 3 (4) (**2018**), 261-266.

[55] Bridgeman, P. W., "The effect of tension on the electrical resistance of certain abnormal metals." Proceedings of the AAAS 57(3) (**1922**), 39–66

[56] Bender, V., "Elastizitatsmessungen an Alkalimetall-Einkristallen in tiefer Temperatur." *Annalen der Physik*, 5, (34) (**1939**) 359-376.

[57] Slotwinski T, Trivisonno J (1969) Temperature dependence of the elastic constants of single crystal lithium. J Phys Chem Solids 30:1276–1278

[58] Day, J.P., Ruoff, A. L., "The Variation of the Elastic Constants of Lithium with Temperature and Press." *Physica Status Solidi A*, 25 (**1974**) 205-213.

[59] Felice, R. A., Trivisonno, J., Schuele, D. E., "Temperature and pressure dependence of the single-crystal elastic constants of ^{6}Li and natural lithium." *Physical Review B*, 16, 12 (**1977**) 5173-5184.

[60] Robertson WM, Montgomery DJ (1960) Elastic modulus of isotopically-concentrated lithium. Phys Rev 117(2):440–442

[61] Schultz R (2002) Lithium: measurement of young's modulus and yield strength. Fermilab Tech Memo 2191:1–6

[62] Tariq S, Ammigan K, Hurh P, Schultz R (2003) Li material testing-fermilab antiproton source lithium collection lens. In: Proceedings of the 2003 particle accelerator conference, 1452–1454.

[63] Yu S, Schmidt RD, Garcia-Mendez R, Herbert R, Dudney NJ, Wolfenstine JB, Sakamoto J, Siegel DJ (2016) Elastic properties of the solid electrolyte Li7La3Zr2O12 (LLZO). Chem Mater 28:197–206

[64] Monroe, C., Newman J., "The impact of elastic deformation on deposition kinetics at lithium/polymer interfaces." *Journal of the Electrochemical Society*, 152 (**2005**), A396–A404.

[65] Ferrese, A., Newman, J., "Mechanical deformation of a lithium-metal anode due to a very stiff separator." *Journal of the Electrochemical Society*, 161 (**2014**), A1350–A1359

[66] Samsonov G (1968) Handbook of the physciochemical properties of the elements. Springer, Berlin

[67] Kaye, G. W. C., Laby, T. H. (eds) (1995) Tables of Physical & Chemical Constants, 16th edn., National Physical Laboratory, Middlessex, England

[68] Gale WF, Totemeier TC (eds) (2004) Smithells metals reference book, 8th edn. Elsevier/Butterworth-Heinemann, New York, USA

[69] Karditsas, P. J., Baptiste, M., "Thermal and structural properties of fusion related materials." United Kingdom Atomic Energy Authority (UKAEA), Technical Report # UKAEA-FUS-294 (1995).

[70] Masias, A., Sakamoto, J., "Solid State Batteries and the Mechanical Properties of Lithium"; *ECS Fall Conf.* (**2017**) Abs #205.

[71] Sargent PM, Ashby MF (1984) Deformation mechanism maps for alkali metals. Scr Metall 18:145–150

[72] Smith, B., "Chevrolet Volt Battery Incident Overview Report." Report # DOT HS 811 573, (2012, January), Washington, DC: National Highway Traffic Safety Administration. Accessed October 14, 2020. https://www.nhtsa.gov/staticfiles/nvs/pdf/Final_Reports.pdf

[73] Josefowitz, W., Kranz, H., Macerata, D., Soczka-Guth, T., Mettlach, H., Porcellato, D., Orsini, F., Hansson, J., "Assessment and Testing of Advanced Energy Storage Systems for Propulsion–European Testing Report". Proceedings of the 21st Worldwide Battery, Hybrid and Fuel Cell Electric Vehicle Symposium and Exhibition. Monaco, EU. April 2-6, 2005. p. 6

[74] Ashtiani, C., “Analysis of Battery Safety and Hazards’ Risk Mitigation.” *Electrochemical Society Transactions*, 11 (19) (**2008**) 1-11.

[75] ISO 26262-4:2018(E), "Road Vehicles - Functional safety - Park 4: Product development at the system level." International Organization for Standardization (ISO), Geneva, CH (2018).

[76] Brewer, J., Nasser, A., Hommes, Q., Najm, W., Jackson, C., “Safety management of automotive rechargeable energy storage systems: The application of functional safety principles to generic rechargeable energy storage systems.” Report # DOT HS 812 556, (2018, November) Cambridge, MA: John A Volpe National Transportation Systems Center. Accessed October 14, 2020. https://www.nhtsa.gov/sites/nhtsa.dot.gov/files/documents/13183-safety_management_electric_070518_v2b_tag.pdf

[77] Stephens, D., Shawcross, P., Stout, G., Sullivan, E., Saunders, J., Risser, S., Sayre, J., “Lithium-ion Battery Safety Issues for Electric and Plug-in Hybrid Vehicles.” Report # DOT HS 812 418, (2017, October) Columbus, OH: Battelle. Accessed October 14, 2020. https://www.nhtsa.gov/sites/nhtsa.dot.gov/files/documents/12848-lithiumionsafetyhybrids_101217-v3-tag.pdf

[78] Obata, H., "Battery Development for Plug-in Hybrid Vehicles." *2012 Advanced Automotive Battery Conference (AABC)*, (**2012**), Orlando, FL, February 7, 2012.

[79] SAE J2464, Battery Safety Standards Committee, Society of Automotive Engineers, "Electric and Hybrid Electric Vehicle Rechargeable Energy Storage System (RESS)." SAE Warrendale, PA, USA (2009).

[80] ISO 12405-3:2014(E), "Electrically propelled road vehicles - Test specification for lithium-ion traction battery packs and systems - Part 3: Safety performance requirements." International Organization for Standardization (ISO), Geneva, CH (2014).

[81] Unkelhaeuser, T., Smallwood, D., “United States Advanced Battery Consortium Electrochemical Storage System Abuse Test Procedure Manual.” SAND99-0497. 1999.

[82] United Nations, "Manual of Tests and Criteria, 7th Edition." Document # ST/SG/AC.10/11/Rev.7, New York City, USA (2019) Section 38.3.

[83] United Nations Global Technical Regulation No.20, “Global Technical Regulation on Electric Vehicle Safety (EVS)” ECE/TRANS/180/Add.20, May 3, 2018. Accessed October 17, 2020. Retrieved from https://www.unece.org/fileadmin/DAM/trans/main/wp29/wp29wgs/wp29gen/wp29registry/ECE-TRANS-180a20e.pdf

[84] UNECE Regulation No. 100, “Uniform provisions concerning the approval of vehicles with regard to specific requirements for the electric power train.”, Series 02 Amendment, July 15, 2013. Accessed, July 24, 2020. Retrieved from https://www.unece.org/fileadmin/DAM/trans/main/wp29/wp29regs/2013/R100r2e.pdf

[85] GB/T-31467.3-2015, "Lithium-ion traction battery pack and system for electric vehicles – Part 3: Safety requirements and test methods." National Standard of the People's Republic of China, May 15, 2015.

[86] KMVSS Annex 1 – Part 48, "Test Procedures for Traction Battery Safety." Korean Motor Vehicle Safety Standards. 2009.

[87] Hatzell, K. B.; Chen, X. C.; Cobb, C. L.; Dasgupta, N. P.; Dixit, M. B.; Marbella, L. E.; McDowell, M. T.; Mukherjee, P. P.; Verma, A.; Viswanathan, V.; Westover, A. S.; Zeier, W. G., "Challenges in Lithium Metal Anodes for Solid-State Batteries." *ACS Energy Letters*, 5 (**2020**), 922−934.

[88] Perea, Alexis, Dontigny, M., Zaghib, K., "Safety of solid-state Li metal battery: Solid polymer versus liquid electrolyte." *Journal of Power Sources*, 359 (**2017**) 182-185.

[89] Chen, R., Nolan, A. M., Lu, J., Wang, J., Yu, X., Mo, Y., Chen, L., Huang, X., Li, H., "The Thermal Stability of Lithium Solid Electrolytes with Metallic Lithium." Joule, 4 (2020) 812-821.

[90] Wu, B., Yang, Y., Liu, D., Niu, C., Gross, M., Seymour, L., Lee, H., Le, P. M. L., Vo, T. D., Deng, Z. D., Dufek, E. J., Whittingham, M. S., Liu, J., Xiao, J., "Good Practices for Rechargeable Lithium Metal Batteries." *Journal of The Electrochemical Society*, 166 (16) (**2019**) A4141-A4149.

[91] Cairns, E. J., Shimotak, H., "High-Temperature Batteries." Science 164, 3886 (1969) 1347-1355.

[92] Whittingham, M. S., Gamble, F. R., "The Lithium Intercalates of the Transition Metal Dichalcogenides." Materials Research Bulletin, 10 (1975) 363-372.

[93] Whittingham, M. S., "Electrical Energy-Storage and Intercalation Chemistry." Science 192, 4244 (1976) 1126-1127.

[94] Chen, S., Dai, F., Cai, M., "Opportunities and Challenges of High- Energy Lithium Metal Batteries for Electric Vehicle Applications." ACS Energy Letters 5 (2020) 3140−3151.

[95] ASTM E9-09, "Standard Test Methods of Compression Testing of Metallic Materials at Room Temperature" (2018).

[96] ASTM E8/E8M-16a (2015) Standard test methods for tension testing of metallic materials

[97] ASTM E139-11 (2011) Standard test methods for conducting creep, creep-rupture, and stress-rupture tests of metallic materials

[98] Masias, A., Felten, N., Sakamoto, J., "Characterizing the Mechanical Behavior of Lithium in Compression." *J. Material Research*, (**2021**), *1-12*.

[99] Cook M, Larke EC (1945) Resistance of copper and copper alloys to homogenous deformation in compression. *Journal of the Institute of Metals*, Vol. 71, 12 (**1945**), 371–390.

[100] Ultrasonic Transducer Technical Note (2011) Accessed 23 July 2018. Retrieved from https://www.olympus-ims.com/en/.downloads/download/?file=285213010&fl=en_US

[101] Schmidt RD, Sakamoto J (2016) In-situ, non-destructive acoustic characterization of solid-state electrolyte cells. J Power Sources 324:126–133

[102] ASTM E494-15 (2015) Standard practice for measuring ultrasonic velocity in materials

[103] Dieter, G.E. *Mechanical Metallurgy (Third Edition)*. McGraw-Hill Book Company. (**1986**), New York, New York. Print.

[104] Instron 5940 Series Single Column Tabletop Product Description. Retrieved from https://www.instron.us/-/media/literature-library/manuals/5940-single-column-table-frames.pdf Access February 6, 2021.

[105] Sharafi, A., Meyer, H.M., Nanda, J., Wolfenstine, J., Sakamoto, J., "Characterizing the Li-$Li_7La_3Zr_2O_{12}$ interface stability and kinetics as a function of temperature and current density"; *J. Power Sources*, Vol. 302 (**2016**) 135-139.

[106] Wang, M., Sakamoto, J., "Correlating the interface resistance and surface adhesion of the Li metal-solid electrolyte interface"; *J. Power Sources*, Vol. 377 (**2018**) 7-11.

[107] Schneider, C. A., Rasband, W. S., Eliceiri, K. W., "NIH Image to ImageJ: 25 years of image analysis." *Nature Methods*, 9 (**2012**), 671-675.

[108] Lex, K. "New Structure Space with Balance Chart Analysis". BYK-Gardner GmbH, European User Meeting 2011, Accessed February 7, 2021. https://instruments.byk.com/fileadmin/byk/support/instruments/technical_information/datasheets/All%20Languages/Appearance/Orange%20Peel/New_Structure_Space_with_Balance_Chart_Analysis__Lex__BYK-Gardner.pdf

[109] ARPA-E Funding Opportunity Announcement DE-FOA-0001478 , Integration and Optimization of Novel Ion Conducting Solids (IONICS). Accessed July 23, 2018. Retrieved from https://arpa-e-foa.energy.gov/FileContent.aspx?FileID=cfac9ce8-5a19-4623-b942-c3e65f3ccf77

[110] Kim, Y., Jo, H., Allen, J.L., Choe, H., Wolfenstine, J., Sakamoto, J., "The Effect of Relative Density on the Mechanical Properties of Hot-Pressed Cubic $Li_7La_3Zr_2O_{12}$"; *Journal of the American Ceramic Society*. Vol. 99, 4 (**2016**) 1367-1374.

[111] Pichl, W., Krystian, M., "The Flow Stress of High Purity Alkali Metals"; *Phys. Stat. Sol. A*, Vol. 160 (**1997**) 373-383.

[112] Sharafi, A., Kazyak, E., Davis, A.L., Yu, S., Thompson, T., Siegel, D.J., Dasgupta, N.P. and Sakamoto, J., "Surface Chemistry Mechanism of Ultra-Low Interfacial Resistance in the Solid-State Electrolyte $Li_7La_3Zr_2O_{12}$"; *Chemistry of Materials,* Vol. 29, 18 (**2017**) 7961-7968.

[113] Courtney, T.H., *Mechanical Behavior of Materials (Second Edition)*. Waveland Press, Inc. (**2000)** Long Grove, Illinois. Print.

[114] Hull, D., Rosenberg, H.M., "The deformation of lithium, sodium and potassium at low temperatures: Tensile and resistivity experiments."; *Philosophical Magazine*, Vol. 4 (**1959**) 303-315.

[115] Gorgas, I., Herke, P., Schoeck, G., "The Plastic Behaviour of Lithium Single Crystals."; *Phys. Stat. Sol. A*, Vol. 67 (**1981**) 617-623.

[116] Xu, C., Ahmad, Z., Aryanfar, A., Viswanathan, V., Greer, J. R., "Enhanced strength and temperature dependence of mechanical properties of Li at small scales and its implications for Li metal anodes."; *Proc. Nat. Acad.Sci.*, Vol. 114 (**2017**) 57-61.

[117] Herbert, E.G., Hackney, S.A., Dudney, N.J., Phani, P.S. Nanoindentation of high-purity vapor deposited lithium films: The elastic modulus, Journal of Materials Research 33(10), 1335-1346 (2018).

[118] E.J. Cheng, A. Sharafi, and J. Sakamoto: Intragranular Li metal propagation through polycrystalline Li6.25Al0.25La3Zr2O12 Ceramic Electrolyte. Electrochim. Acta 223, 85–91 (2017).

[119] A. Sakuda, A. Hayashi, Y. Takigawa, K. Higashi, and M. Tatsumisago: Evaluation of elastic modulus of Li2S–P2S5 glassy solid electrolyte by ultrasonic sound velocity measurement and compression test. J. Ceram. Soc. Jpn. 121, 946–949 (2013).

[120] MRS Fall 2019 Abstract EN05.08.12 : Direct Measurement of Nano-Sized Li Dendrite Growth Stress by In Situ TEM, Megan Aubin.

[121] Herbert, E.G., Hackney, S.A., Thole, V., "Nanoindentation of high-purity vapor deposited lithium films: A mechanistic rationalization of diffusion-mediated flow."; J. Materials Research, Vol. 33 No. 10 (2018) 1347-1360.

[122] W.S. LePage, Y. Chen, E. Kazyak, K. Chen, A.J. Sanchez, A. Poli, E. Arruda, M.D. Thouless, and N.P. Dasgupta: Lithium Mechanics: Roles of Strain Rate and Temperature and Implications for Lithium Metal Batteries. J. Electrochem. Soc. 166, A89–A97 (2019).

[123] Wang, M. J., Choudhury, R., Sakamoto, J., "Characterizing the Li-Solid-Electrolyte Interface Dynamics as a Function of Stack Pressure and Current Density." *Joule*, 3 (9) (**2019**) 2165-2178.

[124] Krauskopf, T., Hartmann, H., Zeier, W. G., Janek, J., "Toward a Fundamental Understanding of the Lithium Metal Anode in Solid-State Batteries – An Electrochemo-Mechanical Study on the Garnet-Type Solid Electrolyte Li6.25Al0.25La3Zr2O12." *ACS Applied Materials & Interfaces* (11) (**2019**) 14463-14477.

[125] Kasemchainan, J., Zekoll, S., Spencer Jolly, D., Ning, Z., Hartley, G.O., Marrow, J., Bruce, P.G., "Critical stripping current leads to dendrite formation on plating in lithium anode solid electrolyte cells."; Nature Materials, Vol. 18 (2019) 1105–1111.

[126] Sakamoto, J. "More pressure needed."; Nature Energy, Vol. 4 (2019), 827–828.

[127] Zener, C., Hollomon, H., J., "Effect of strain rate upon plastic flow of steel."; Journal of Applied Physics, Vol. 15 (1944) 22-32.

[128] Arrhenius, S., "Über die Reaktionsgeschwindigkeit bei der Inversion von Rohrzucker durch Säuren."; Zeitschrift für Physikalische Chemie, Vol. 4 (1889), 226-248.

[129] Holloman, J.H. Tensile Deformation. Trans. Metal. Soc. AIME. 12, 268-290 (1945)

[130] K. Huang and R.E. Loge: A review of dynamic recrystallization phenomena in metallic materials. Mater. Des. 111, 548–574 (2016).

[131] C.D. Fincher, D. Ojeda, Y. Zhang, G.M. Pharr, and M. Pharr: Mechanical properties of metallic lithium: from nano to bulk scales. Acta Mater. 186, 215–222 (2020).

[132] W.F. Hosford: Mechanical Behavior of Materials, 2nd ed. (Cambridge University Press, 2010).

[133] Sakai, T., Belyakov, A., Kaibyshev, R., Miura, H., Jonas, J.J. Dynamic and post-dynamic recrystallization under hot, cold and severe plastic deformation conditions. Progress in Materials Science, 60. 130-207 (2014).

[134] Boulger, F.W. DMIC Report 226, Battelle Memorial Institute, 13–37 (1966).

[135] J.E. Ni, E.D. Case, J.S. Sakamoto, E. Rangasamy, and J.B. Wolfenstine: Room temperature elastic moduli and Vickers hardness of hot-pressed LLZO cubic garnet. J. Mater. Sci. 47, 7978–7985 (2012).

[136] S. Harris, X. Zhang, J.Q. Wang, K. Harrison, and S. Roberts: Time-Dependent Multi-Scale Theory and Simulation for Contact Between Li Metal and a Ceramic Solid Electrolyte. Abstract # EN05.04.07, Materials Research Society 2019 Fall Conference, Boston, MA, December 3, 2019.

[137] United States Advanced Battery Consortium (2019, December). Development of Lithium Electrode Based Cell and Manufacturing for Automotive Traction Applications. Accessed December 17, 2019. Retrieved from http://www.uscar.org/commands/files_download.php?files_id=504

[138] Frenkel, J., The theory of the elastic limit and the solidity of crystal bodies; Zeitschrift fur Physik. Vol. 37, 7/8 (1926) 572-609.

[139] Masias, A., Upadhye, M., Sakamoto, J., "Safety Considerations of Lithium Metal Solid State Batteries." (***in draft***).

[140] Masias, A., Snyder, K., Miller, T., "Automaker Energy Storage Needs for Electric Vehicles." In: SAE-China, FISITA (eds) Proceedings of the FISITA 2012 World Automotive Congress. Lecture Notes in Electrical Engineering, Vol. 192, (**2013**), 729-741. Springer, Berlin.

[141] US DOT TP-305-01, "Laboratory Test Procedure for FMVSS 305, Electric Powered Vehicles: Electrolyte Spillage and Electrical Shock Protection." September 11, 2008. Accessed July 24, 2020. https://www.nhtsa.gov/sites/nhtsa.dot.gov/files/tp-305-01.pdf

[142] Battery Transportation Working Group, Japan Automotive Research Institute. "Vibration Test for Large Lithium-Ion Battery Assemblies on UN Transportation Manual of Tests & Criteria." Working Group on the Testing of and Criteria for Lithium Batteries, Paris, FR April 20-22, 2009. Accessed September 22, 2020. Retrieved from https://www.prba.org/wp-content/uploads/JARI_presentation_UN_LIBWG_20090420-1.pdf

[143] Wietelmann, U. and Steinbild, M. (2014). Lithium and Lithium Compounds. In Ullmann's Encyclopedia of Industrial Chemistry, (Ed.). https://doi.org/10.1002/14356007.a15_393.pub2

[144] Tao, C., Ye, Q., Wang, C., Qian, Y., Wang, C., Zhou, T., Tang, Z., "An experimental investigation on the burning behaviors of lithium ion batteries after different immersion times." Journal of Cleaner Production, 242 (2020) 118539.

[145] "Number of U.S. Aircraft, Vehicles, Vessels, and Other Conveyances." United States Department of Transportation, Bureau of Transportation Statistics. Accessed October 12, 2020. https://www.bts.gov/content/number-us-aircraft-vehicles-vessels-and-other-conveyances

[146] Takahashi, M., Maeda, K., Nakagawa, S. "Immersion Characteristics of Lithium-Ion Batteries for Vehicles." JARI Research Journal Report # 20130702. Access 9/22/20. Retrieved from http://www.jari.or.jp/Portals/0/resource/JRJ_q/JRJ20130702_q.pdf

[147] Ohtomo, T., Hayashi, A., Tatsumisago, M., Kawamoto, K., "Suppression of H2S gas generation from 75Li2S*25P2S5 glass electrolyte by additives." *J. Materials Science,* 48 (**2013**), 4137-4142.

[148] "Safety & Health Topics | Hydrogen Sulfide – Hazards." United States Department of Labor, Occupational Safety and Hazards Administration. Accessed July 21, 2020. https://www.osha.gov/SLTC/hydrogensulfide/hazards.html

[149] "Hazards when Purging Hydrogen Gas-Cooled Electric Generators." United States Department of Labor, Occupational Safety and Hazards Administration. Safety and Health

Information Bulletin SHIB 01-22-2016. Accessed July 21, 2020. https://www.osha.gov/dts/shib/shib012216.html

[150] Masias, A., Upadhye, M., Sakamoto, J., "Safety Assessment of Solid-State Lithium Batteries." MRS Fall 2019, Abstract EN01.01.09 (2019), Boston, December 2, 2019.

[151] Kozen, A. C., Lin, C., Pearse, A. J., Schroeder, M. A., Han, X., Hu, L, Lee, S., Rubloff, G. W., Noked, M., "Next-Generation Lithium Metal Anode Engineering via Atomic Layer Deposition." ACS Nano, 9, 6 (2015) 5884-5892.

[152] Zhang, Y., Lv, W., Huang, Z., Zhou, G., Deng, Y., Zhang, J., Zhang, C., Hao, B., Qi, Q., He, Y., Kang, F., Yang, Q., "An air-stable and waterproof lithium metal anode enabled by wax composite packaging." Science Bulletin, 64 (2019), 910-917.

[153] Xu, Q., Lin, J., Ye, C., Jin, X., Ye, D., Lu, Y., Zhou, G., Qiu, Y., Li, W., "Air-stable and Dendrite-Free Lithium Metal Anodes Enabled by a Hybrid Interphase of C60 and Mg." Advanced Energy Materials, 10 (2020), 1903292.

[154] Park, J., Jeong, J., Lee, Y., Oh, M., Ryou, M., Lee, Y. M., "Micro-Patterned Lithium Metal Anodes with Suppressed Dendrite Formation for Post Lithium-Ion Batteries." Advanced Materials Interfaces, 3, 11 (2016) 1600140.

[155] Lowe, J. S., Siegel, D. J., "Modeling the Interface between Lithium Metal and Its Native Oxide." Applied Materials & Interfaces (2020). https://dx.doi.org/10.1021/acsami.0c12468

[156] Wood, K.N., Xerxes Steirer, K., Hafner, S.E., Ban, C., Santhanagopalan, S., Lee, S., Teeter, G., "Operando X-ray photoelectron spectroscopy of solid electrolyte interphase formation and evolution in Li2S-P2S5 solid-state electrolytes." Nature Communications, 9 (2018) 2490, 1-10.

[157] Walther, F., Koerver, R., Fuchs, T., Ohno, S., Sann, J., Rohnke, M., Zeier, W.G., Janek, J., "Visualization of the Interfacial Decomposition of Composite Cathodes in Argyrodite-Based All-Solid-State Batteries using Time-of-Flight Secondary-Ion Mass Spectrometry." Chemistry of Materials, 31 (2019), 3745-3755.

[158] Kim, S.H., Kim, K., Choi, H., Im, D., Heo, S., Choi, H.S., "In situ observation of lithium metal plating in a sulfur-based solid electrolyte for all-solid-state batteries." J. Materials Chem. A, 7 (2019) 13650-13657.

[159] United States Advanced Battery Consortium (USABC) (2019) "Development of Lithium Electrode Based Cell and Manufacturing for Automotive Traction Applications." Accessed October 19, 2020. Retrieved from http://www.uscar.org/commands/files_download.php?files_id=509

[160] The United States Code, Title 40: Protection of the Environment, Chapter 1, Subchapter C, Part 86 -- Control of Emissions from New and In-Use Highway Vehicles and Engines, Subpart A

-- General Provisions for Heavy-Duty Engines and Heavy-Duty Vehicles, Section 86.001-2 Definitions. Retrieved from https://www.ecfr.gov/cgi-bin/ECFR? (Accessed February 21, 2021).

[161] California Code of Regulations, Title 13. Motor Vehicles, Division 3. Air Resource Board, Chapter 1. Motor Vehicle Pollution Control Devices, Article 2. Approval of Motor Vehicle Pollution Control Devices (New Vehicles) (Refs & Annos), Section 1961.2. Exhaust Emission Standards and Test Procedures - 2015 and Subsequent Model Passenger Cars, Light-Duty Trucks, and Medium-Duty Vehicles. Retrieved from https://govt.westlaw.com/calregs/Search/Index (Accessed February 21, 2021).

[162] Zhang, X., Wang, Q. J., Harrison, K. L., Roberts, S. A., Harris, S. J., "Pressure-Driven Interface Evolution in Solid-State Lithium Metal Batteries." Cell Reports Physical Science, 1 (2) (2020), 100012.

[163] Xiao, Y., Wang, Y., Bo, S., Kim, J. C., Miara, L. J., Ceder, G., "Understanding interface stability in solid-state batteries." Nature Reviews Materials 5 (2019) 105-126.

[164] Taylor, N. J., Stangeland-Molo, S., Haslam, C. G., Sharafi, A., Thompson, T., Wang, M., Garcia-Mendez, R., Sakamoto, J., "Demonstration of high current densities and extended cycling in the garnet Li7La3Zr2O12 solid electrolyte." *Journal of Power Sources* 396 (2**018**) 314-318.

[165] Zhang, J., "Anode-less." *Nature Energy* 4 (**2019**) 637-638.

[166] Wang, M. J., Carmona, E., Gupta, A., Albertus, P., Sakamoto, J., "Enabling "lithium-free" manufacturing of pure lithium metal solid-state batteries through in situ plating." *Nature Communications* 11 (**2020**) 5201.

[167] Weber, R., Genovese, M., Louli, A. J., Hames, S., Martin, C., Hill, I. G., Dahn, J. R., "Long cycle life and dendrite-free lithium morphology in anode-free lithium pouch cells enabled by a dual-salt liquid electrolyte." *Nature Energy* 4 (**2019**) 683-689.

[168] Mizusaki, J., Tagawa, H., Saito, K., Uchida, K., Tezuka, M., "Lithium carbonate as a solid electrolyte." *Solid State Ionics*, 53-56 (**1992**) 791-797.

[169] Ohtomo, T., Hayahsi, A., Tatsumisago, M., Kawamoto, K., "Suppression of H2S gas generation from 75Li2S*25P2S5 glass electrolyte by additives." *J. Materials Science*, 48 (**2013**), 4137-4142.

[170] Kjell, G., Lang, J. F., "Comparing different vibration tests proposed for li-ion batteries with vibration measurements in an electric vehicle." Electric Vehicle Symposium 27, Barcelona, Spain, November 17-20, 2013.

[171] Hooper, J. M., Marco, J., Chouchelamane, G. H., Lyness, C., "Vibration Durability Testing of Nickel Manganese Cobalt Oxide (NMC) Lithium-Ion 18,650 Battery Cells." Energies, 9, 52 (2016) 1-27.

[172] Hooper, J.M., Marco, J., "Characterizing the in-vehicle vibration inputs to the high voltage battery of an electric vehicle." Journal of Power Sources, 245 (2014) 510-519.

[173] Masias, A. "Challenges of Lithium Metal Batteries for Automotive Applications." 37th Annual International Battery Seminar, Virtual, July 28, 2020.

[174] SAE J1772, Hybrid – Electric Vehicle Committee, Society of Automotive Engineers, "SAE Electric Vehicle and Plug in Hybrid Electric Vehicle Conductive Charge Coupler." SAE Warrendale, PA, USA (2017).